NASA CR - 174810

(NASA-CR-174810) ION THRUSTER PERFORMANCE MODEL (Colorado State Univ.) 135 p HC A07/MF A01 CSCL 21C
N85-12935
Unclas
G3/20 12187

ION THRUSTER PERFORMANCE MODEL

PREPARED FOR
LEWIS RESEARCH CENTER
NATIONAL AERONAUTICS AND SPACE ADMINISTRATION

GRANT NGR-06-002-112

by

John R. Brophy

Approved by

Paul J. Wilbur

December 1984

Department of Mechanical Engineering
Colorado State University
Fort Collins, Colorado

1. Report No.
NASA CR 174810

2. Government Accession No.

3. Recipient's Catalog No.

4. Title and Subtitle
ION THRUSTER PERFORMANCE MODEL

5. Report Date
Dec. 1984

6. Performing Organization Code

7. Author(s)
John R. Brophy

8. Performing Organization Report No.

9. Performing Organization Name and Address
Department of Mechanical Engineering
Colorado State University
Fort Collins, Colorado 80523

10. Work Unit No.

11. Contract or Grant No.
NGR-06-002-112

12. Sponsoring Agency Name and Address
National Aeronautics and Space Administration
Washington, D.C. 20546

13. Type of Report and Period Covered
Dec. 1, 1983 - Dec. 1, 1984

14. Sponsoring Agency Code

15. Supplementary Notes Grant Monitor - William Kerslake, NASA Lewis Research Center, Cleveland, Ohio 44135. This report is a reproduction of the Ph.D. Dissertation of John R. Brophy. It is submitted to the sponsor and to the distribution list in this form both as a presentation of the technical material, and as an indication of the academic program supported by the grant.

16. Abstract

A model of ion thruster performance is developed for high flux density, cusped magnetic field thruster designs. This model is formulated in terms of the average energy required to produce an ion in the discharge chamber plasma and the fraction of these ions that are extracted to form the beam. The direct loss of high energy (primary) electrons from the plasma to the anode is shown to have a major effect on thruster performance. The model provides simple algebraic equations enabling one to calculate the beam ion energy cost, the average discharge chamber plasma ion energy cost, the primary electron density, the primary-to-Maxwellian electron density ratio and the Maxwellian electron temperature. Experiments indicate that the model correctly predicts the variation in plasma ion energy cost for changes in propellant gas (Ar, Kr and Xe), grid transparency to neutral atoms, beam extraction area, discharge voltage, and discharge chamber wall temperature.

The model and experiments indicate that thruster performance may be described in terms of only four thruster configuration dependent parameters and two operating parameters. The model also suggests that improved performance should be exhibited by thruster designs which extract a large fraction of the ions produced in the discharge chamber, which have good primary electron and neutral atom containment and which operate at high propellant flow rates. In addition, it suggests that hollow cathode efficiency becomes increasingly important to the discharge chamber performance as the discharge voltage is reduced. Finally, the utility of the model in mission analysis calculations is demonstrated. The model makes it easy to determine which changes in thruster design or operating parameters have the greatest effect on the payload fraction and/or mission duration.

17. Key Words (Suggested by Author(s))
Electrostatic Thruster
Discharge Chamber Model

18. Distribution Statement
Unclassified - Unlimited

19. Security Classif. (of this report)
Unclassified

20. Security Classif. (of this page)
Unclassified

21. No. of Pages
133

22. Price*

* For sale by the National Technical Information Service, Springfield, Virginia 22161

TABLE OF CONTENTS

Table of Contents (Continued)

LIST OF FIGURES

List of Figures (Continued)

List of Figures (Continued)

LIST OF TABLES

I. INTRODUCTION

Electron bombardment ion thrusters have been proposed for both primary and auxiliary space propulsion applications for nearly two-and-a-half decades. During this time, thruster performance requirements have varied according to the missions of current interest. Also during this time, the development of thruster designs capable of meeting these requirements has been largely experimental. That is, thruster development has generally been accomplished by a procedure in which the design parameters that influence thruster performance are physically varied until an acceptable configuration is obtained.

This procedure has several inherent limitations. First of all, it can be time consuming, especially if a large number of parameters is involved. Secondly, an optimum configuration may not be found. That is, once a configuration capable of fulfilling the mission requirements is identified, the procedure is generally terminated even though this may not result in the best configuration possible. Finally, changes in the missions of current interest to those characterized by different thruster requirements necessitate that the iterative experimental procedure be repeated.

Consequently, there is a need for the development of an analytical model which describes the effects of thruster design variables and operating parameters on thruster performance. Such a model should, as a minimum, be capable of providing guidance for the iterative procedure described above, and ideally would be capable of describing exactly how a thruster should be designed to achieve a given set of performance requirements.

Many models of discharge chamber operation have been developed over the last 24 years. A brief discussion of these models is given in the next section. In general, the complexity of the processes taking place in the discharge chamber of an ion thruster together with the relative ease with which new thruster designs can be tested experimentally has resulted in a situation in which theoretical understanding has lagged experimental developments.

The objective of this research is to improve the theoretical understanding of ion thruster operation by providing a simple physical model of the processes affecting thruster performance. Additional constraints on this model are that it should be easy to use, yet general enough to be applicable to a wide range of thruster configurations and operating conditions.

Background

Analytical modeling of electron bombardment ion thrusters has been on going more or less continuously since their introduction by Kaufman [1,2] in 1960. Milder [3] provides a survey of modeling efforts made through 1969. In this survey he concluded that, "...our knowledge and understanding of the physics of these plasmas is far from complete." In addition, he concluded that the usefulness of these efforts was limited by either the simplyfing assumptions required to make the problem tractable or the difficulty of applying less simplified models.

Kaufman [4] presents a discussion of thruster technology as of 1974 in which the latest theories of thruster operation are described. He concluded, as had Milder earlier, that the most successful effort to date was the semiempirical approach proposed by Masek [5] in 1969. The theory of Masek is semiempirical in that it requires as input a detailed knowledge of the plasma properties inside the thruster discharge chamber. These properties are generally obtained using a Langmuir probe together with a data reduction procedure that is both tedious and until recently [6,7] of only limited accuracy.

Since 1974 a number of analytical models have been developed, directed toward different aspects of ion thruster discharge chamber operation [7-19]. Of these, the models proposed in references 8 through 12 are extensions of Masek's modeling technique in that they require detailed Langmuir probe data as inputs. References 16 through 18 present models which do not require probe data, but which instead consist of a complex set of equations which must be solved iteratively by a computer. This complexity makes these models difficult to apply and limits their usefulness in providing guidelines to improved thruster designs.

Discharge chamber models of ion sources for neutral beam injectors have also been proposed recently [20-22]. The operation of these sources is in many respects very similar to that of ion sources for space propulsion applications. This similarity was enhanced by the recent switch in space thruster design [23,24] to discharge chambers characterized by the same high magnetic flux density cusped fields used in neutral beam injectors. References 20 through 22 present relatively simple models that provide valuable insight to discharge chamber operation, but also require plasma property data as inputs. Further, these models are not developed to the point where the performance of a given discharge design can be calculated directly.

In summary, the situation at the present time is remarkably similar to the way it was in 1969 as described by Milder [3]. Many additional models have been proposed since 1969 providing a significant improvement in the overall understanding of discharge chamber processes, however, most of these models still require detailed plasma property data as inputs. Those that do not are either over simplified, resulting in a loss of generality and usefulness, or too complex to be applied easily. Thus, there is a need for the development of a model of ion thruster performance that is easy to use, does not require plasma data as inputs, and yet is general enough and accurate enough to serve as a guideline for the design of improved thruster configurations.

Overview

This dissertation is organized in the following manner. First, a brief review of ion thruster operation is given in Chapter II. In this chapter, the dominant mechanism affecting thruster performance are identified and discussed qualitatively. Since this report is primarily concerned with ion thruster discharge chamber operation, detailed discussions of other thruster components such as the ion accelerator system and cathodes, etc., will not be given. These components will be discussed only in regard to their effect on the operation of the main discharge chamber.

In Chapter III the analytical derivation of the equations comprising the thruster performance model proposed in this investigation is presented. This model consists of a set of algebraic equations, each of which describes the behavior of a different performance parameter. For example, a single equation for the thruster performance curve (variation of beam ion energy cost with propellant utilization efficiency) is developed. Other equations are developed that allow the average values of the discharge chamber plasma properties to be calculated as functions of the thruster operating point. These plasma properties include: the primary electron density, the primary-to-Maxwellian electron density ratio, the Maxwellian electron temperature, and the ratio of doubly-to-singly charged ion currents in the beam.

In Chapter IV, the experimental apparatus and procedures used to investigate the validity of the proposed model are described. Experimental results, comparison of these results with the predictions of the model, and a discussion of this comparison are also given in this chapter.

Three applications of the thruster performance model are discussed in Chapter V. The first of these illustrates the effect of thruster design and operating parameters on the standard performance curve. The second application describes how the model can be used to extrapolate data taken without ion beam extraction to obtain the performance curve applicable to operation with beam extraction. Finally, an illustration of how the model can be applied to mission analysis calculations is presented. In this application, the effects of thruster design parameters and propellant utilization efficiency on the deliverable payload fraction are discussed for an earth orbit raising mission (low earth orbit to geosynchronous earth orbit).

The major conclusions of this investigation are summarized in Chapter VI. SI units are used throughout this report with the exception that energy is frequently given in units of electron volts. In addition, for thermal electrons the energy quantity kT, where k is Boltzmann's constant and T is the temperature will be given as eT_M where e is the electronic charge and T_M is the electron temperature in eV.

II. ION THRUSTER OPERATION

A contemporary "ring cusp" electron bombardment ion thruster is shown schematically in Fig. 1. This thruster consists of a cylindrical steel structure bounded at one end by a circular steel plate and at the other end by a set of two closely spaced grids. The volume bounded by this structure is referred to as the discharge chamber. The two grids at the end of the discharge chamber have a matched matrix of holes through which the ion beam is extracted. The inner grid is referred to as the screen grid while the outer one is called the accelerator grid.

During thruster operation, neutral propellant gas is injected into the discharge chamber. The preferred propellant gas has, for the most part, been mercury vapor because of its large atomic mass, low ionization energy, and its liquid phase storability. Cesium vapor has also been used. However, at the present time, the propellants of most interest are the rare gases argon, krypton and xenon. In this investigation, only these rare gases are considered. The propellant gas is assumed to fill the discharge chamber uniformly during thruster operation.

A hollow cathode serves as the source of electrons for the discharge chamber. Hollow cathodes have replaced both refractory metal and oxide cathodes in ion thrusters primarily because they exhibit very long lifetimes and can be restarted a number of times even after exposure to air (an important capability if the thruster is to be

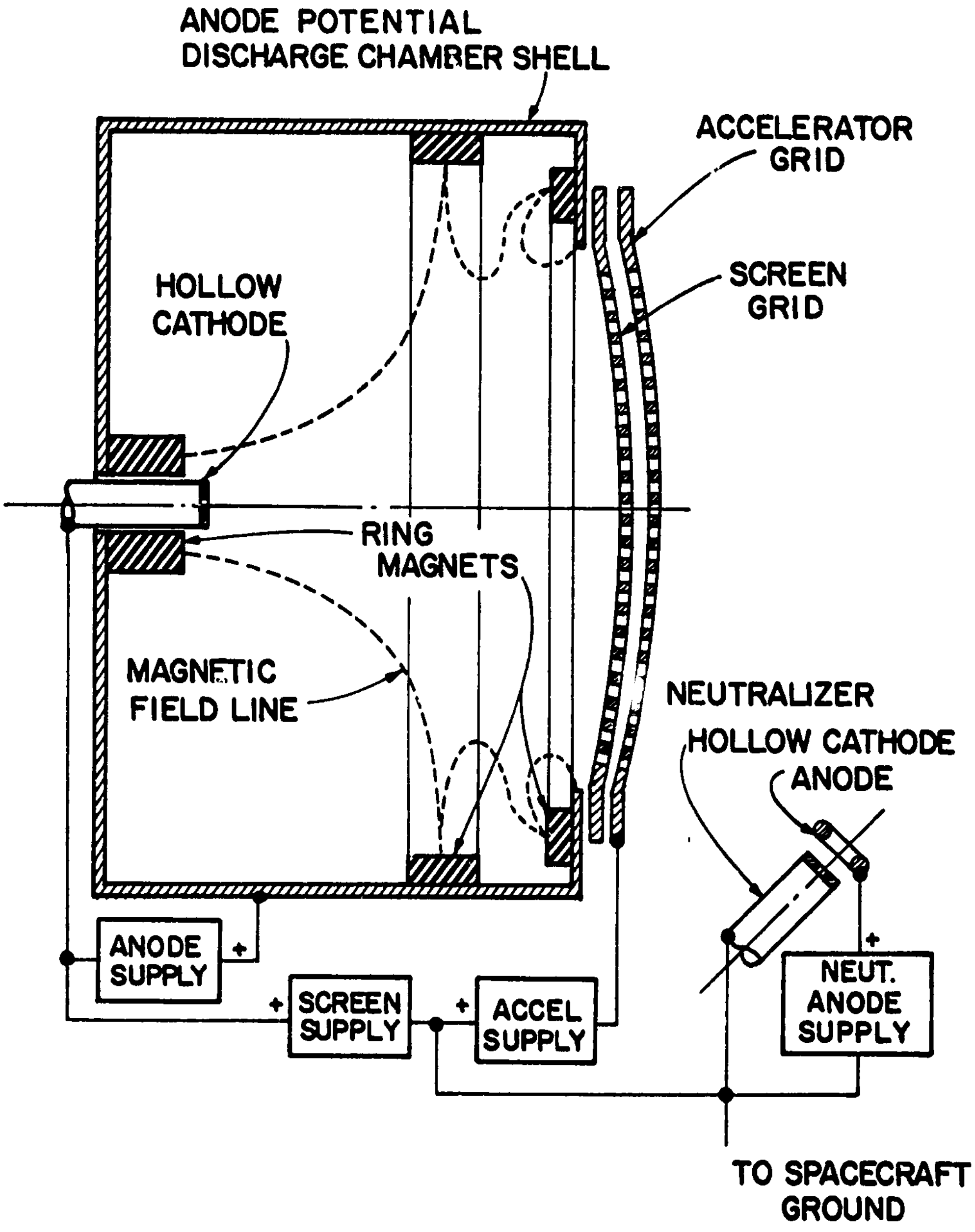

Figure 1. Ion Thruster Schematic

preflight tested). A detailed discussion of hollow cathodes is given by Siegfried [25].

The electrons emitted by the cathode in Fig. 1 are accelerated by an electric field adjacent to the cathode into the discharge chamber. This electric field is established by biasing the discharge chamber walls (with the exception of the screen grid) 30 to 50 volts positive of the cathode by means of an external DC power supply (called the discharge or anode supply). Electrons which have undergone this acceleration are called primary electrons. The energy of these primary electrons is determined by the voltage difference applied between the anode and cathode. The magnitude of this voltage difference is chosen so that the collision cross section for ionization by the primary electrons is large while at the same time the collision cross section for the production of multiply charged ions by the primary electrons is small.

A second group of electrons originates from the inelastic interaction of the primaries with the neutral propellant atoms. These interactions reduce the energy of the primary electrons. In this investigation, an electron is no longer considered a primary electron if it has had at least one inelastic collision. Ionization, the inelastic collision process of primary interest here, results in the release of low energy secondary electrons. Primary electrons, that have had their energy degraded by inelastic collisions, and secondary electrons released by ionization, thermalize to form an electron population with a nearly Maxwellian energy distribution (characterized by a temperature on the order of a few eV). It is possible for both electron populations to exist simultaneously in the discharge chamber due to the low interaction rate between the primary and Maxwellian electrons [26].

At typical discharge chamber neutral atom densities ($\sim 10^{18}cm^{-3}$), the ionization mean free path for primary electrons in neutral atoms is on the order of meters while typical discharge chamber dimensions are on the order of tens of centimeters. For this reason, a magnetic field is employed to restrict the direct access of primary electrons to the anode. The magnetic field for the thruster of Fig. 1 is created by the rings of magnets of alternating polarity located along the back and sides of the discharge chamber. The configuration and strength of the magnetic field has a substantial effect on thruster operation and consequently has been the subject of numerous studies [6,7,13,24,27-33]. Contemporary thruster designs are operated with the entire discharge chamber housing (except for the screen grid) at anode potential. Magnetic field lines at the field cusps, thus, terminate on anode potential surfaces. This allows electrons to be lost to the anode by travelling along magnetic field lines as well as by diffusing across them. To adequately restrict the flow of primary electrons along the field lines to the anode, magnetic flux densities on the order of 0.1 tesla are required.

The discharge chamber magnetic field reduces the probability that a primary electron will be collected by the anode without first having had an inelastic collision with a neutral propellant atom. This probability is a function of the thruster size, the discharge chamber magnetic field configuration, the cathode location and the neutral atom density. As the neutral density decreases, the probability that a primary electron will be lost to the anode without having an inelastic collision increases.

For the hypothetical case of a zero neutral atom density, this probability is one. That is, all primary electrons emitted by the cathode will be collected by the anode and none will have inelastic collisions. In this case, each primary electron will, on the average, travel a certain distance through the discharge chamber before being collected by the anode. This distance is a characteristic of the thruster geometry, magnetic field configuration and cathode location, and is called the primary electron containment length [34]. With this definition, the probability of primary electron loss to the anode may be expressed as a function of the ratio of the primary electron containment length to the mean free path for primary electron-neutral atom inelastic collisions [34]. The loss of primary electrons to the anode constitutes a loss of discharge energy. Consequently, ion thruster performance is strongly dependent on the probability with which primary electrons are lost [34,35].

The plasma produced within the discharge chamber will typically assume a potential a few volts positive of the anode. Thus, a potential sheath will exist at all plasma boundaries. The magnitude of this sheath at cathode potential surfaces depends primarily on the magnitude of the discharge voltage applied between the cathode and anode. The sheath potential at cathode surfaces is sufficiently negative to reflect all but the most energetic electrons in the tail of the Maxwellian distribution. Consequently, the vast majority of electrons in the plasma can leave the discharge chamber only at anode potential surfaces.

Of the ions produced in the discharge chamber, some will reach the discharge chamber walls. Those that do, recombine with electrons there and return to the plasma as neutral atoms. Most of the ions that reach the grid system,on the other hand, are accelerated by the electric field between the screen and accelerator grid to form the ion beam. The fraction of the total ion current produced that is extracted into the beam is called the extracted ion fraction. Because it does little good to produce ions in the plasma only to have them recombine at the discharge chamber walls, it is clearly desirable to have thruster designs in which the extracted ion fraction is as large (close to one) as possible [34]. The electric field between the grids is established by biasing the thruster body positive of ground potential (on the order of 1000 volts) and biasing the accelerator grid several hundred volts negative of ground potential. The final velocity of the ions in the beam is determined by the sum of the positive potential applied to the thruster cathode and the discharge voltage.

Electrons are injected into the positive ion beam by a cathode (called a neutralizer) positioned downstream of the accelerator grid in order to space charge and current neutralize the beam. The negative accelerator grid prevents these electrons from backstreaming to the positive thruster body.

During thruster operation, the propellant gas in the discharge chamber is only partially ionized, with the ion density typically an order of magnitude smaller than the neutral atom density. Thus, one might expect the neutral flux through the grids to be greater than the ion flux. This, however, is not the case since the neutral flux is determined by free-molecular flow toward the grids at a temperature governed by the mean discharge chamber wall temperature [36] ($\sim$ 400K). The ions, on the other hand, tend to move toward the grid system at the Bohm [37] velocity, which is governed by the much higher electron temperature (typically 5 eV or $\sim$ 58,000K). Thus, the ion flux through the grids is usually greater than the neutral flux even though the ion density is substantially smaller than the neutral density.

The ratio of the beam current (assuming singly charged ions only) to the total propellant flow rate (expressed in units of equivalent amperes) is known as the propellant utilization efficiency. For a constant total propellant flow rate, increasing the propellant utilization efficiency generally requires an increase in the average energy required to produce a beam ion. This variation of the beam ion energy cost with the propellant utilization is known as a performance curve. It will be shown in the chapters that follow that the dominant mechanisms affecting the performance curve are the loss of primary electrons to the anode and the extracted ion fraction.

III. THEORETICAL DEVELOPMENT

Thruster Performance Model

In this section, a model is developed which results directly in a single algebraic equation for the variation of the beam ion energy cost with the propellant utilization efficiency for high flux density cusped magnetic field thrusters. This is made possible by formulating the model in terms of the average energy required to produce an ion in the discharge chamber plasma and the fraction of ions produced which are extracted into the beam. A key feature of the model is that it provides a simple technique for the calculation of the average discharge plasma ion energy cost as a function of the propellant flow rate and propellant utilization efficiency.

Assumptions and Limitations

The development of the model assumes steady state discharge chamber operation. The model is applicable to discharge chambers which produce low pressure, partially ionized, optically thin plasmas in which neutral densities are in the range of 10^{18} to 10^{19} m^{-3} and plasma densities range from 10^{16} to 10^{17} m^{-3}. In addition, Maxwellian electron temperatures and primary electron energies should range from 1 to 10 eV and 30 to 50 eV, respectively.

Electron energy losses due to elastic collisions with ions or neutral atoms are neglected. This can be justified because the average energy loss per encounter is proportional to the ratio of masses, and this ratio is small ($\sim 10^{-5}$). Electron energy losses resulting from inelastic collisions with ions are also neglected because of the low ion density relative to the neutral density. This should not cause a significant error, except perhaps at very high propellant utilizations. Only singly charged ions are assumed to be produced, and the effect of metastable atomic states on ion production is neglected.

Primary electron thermalization resulting from collisions with the background Maxwellian electrons also is neglected. Primary electron behavior is assumed to be limited to either inelastic collisions with neutral atoms or direct loss to anode potential surfaces. A primary electron is considered to join the Maxwellian electron population after having one inelastic collision.

Electrons are assumed to be constrained by the plasma sheaths so they are able to leave the plasma only at anode potential surfaces. Ions and photons (emitted by the de-excitation of excited propellant atoms) are assumed to be lost across all plasma boundaries. The assumption of a low pressure discharge implies that ion-electron recombination should be wall controlled, consequently, volume ion recombination is neglected.

The neutral atom density is assumed to be uniform throughout the discharge chamber, and free molecular flow is assumed to apply to the neutral atom flux through the accelerator grid system.

Beam Ion Energy Cost

The average energy cost per beam ion is defined as,

$$\varepsilon_B \equiv (J_D - J_B)\, V_D/J_B \quad , \text{[eV/beam ion]} \qquad (1)$$

where all symbols are defined in Appendix C. The beam current (J_B) in Eq. 1 is subtracted from the discharge current (J_D) so that the energy that goes into accelerating the beam ions through the discharge voltage is not charged to the beam ion energy cost. The numerator on the right-hand-side of Eq. 1 represents the power used to operate the discharge chamber.

In a similar manner, the average energy expended in creating ions in the discharge chamber plasma may be defined as,

$$\varepsilon_P \equiv [J_D - (J_B + J_C)]\, V_D/J_P \quad , \text{[eV/plasma ion]}. \qquad (2)$$

By analogy to Eq. 1, the "$J_B + J_C$" term is subtracted from the discharge current so that the energy that goes into accelerating these ions out of the discharge chamber plasma into the chamber walls or the beam is not included in the plasma ion production cost. Rearranging Eq. 2 yields,

$$\varepsilon_P = \frac{(J_D - J_B)V_D}{J_B}\left(\frac{J_B}{J_P}\right) - \frac{J_C V_D}{J_P} \quad . \qquad (3)$$

For steady state operation, the total ion current produced (J_P) must be equal to the total ion current leaving the plasma. For ion thruster discharge chambers, ions can only leave the plasma by going to cathode potential surfaces, anode potential surfaces or by being extracted into the beam. Thus, the total ion current produced is given by*,

$$J_P = J_B + J_C + J_A \quad . \qquad (4)$$

Dividing this equation through by J_P yields,

---

* Equation 4 is a statement of continuity for the ions.

$$1 = f_B + f_C + f_A \quad , \tag{5}$$

where,

$$f_B \equiv J_B/J_P \quad , \quad f_C \equiv J_C/J_P \text{ and } f_A \equiv J_A/J_P \quad . \tag{6}$$

The fractions f_B, f_C and f_A are, in order, the extracted ion fraction, the fraction of ion current produced that goes to cathode potential surfaces, and the fraction of ion current produced that goes to anode potential surfaces. Using the definitions of f_B and f_C in Eq. 3 along with Eq. 1 yields,

$$\varepsilon_p = \varepsilon_B f_B - f_C V_D \quad . \tag{7}$$

Solving this equation for ε_B gives the result,

$$\varepsilon_B = \varepsilon_p/f_B + f_C V_D/f_B \quad . \tag{8}$$

This equation describes the beam ion energy cost as a function of the plasma ion energy cost (ε_p), the extracted ion fraction (f_B), the fraction of ion current to cathode potential surfaces (f_C) and the discharge voltage (V_D).

The first term on the right-hand-side of Eq. 8 represents the energy loss associated with producing ions in the discharge chamber and extracting only a fraction of them into the beam. Ions which are not extracted into the beam go to the walls of the discharge chamber where they recombine. The resulting atoms must then be re-ionized before they can contribute to the beam current. The factor $1/f_B$ may be interpreted as the average number of times that a beam ion undergoes ionization from a neutral state before being extracted into the beam.

The second term on the right-hand-side of Eq. 8 represents the energy wasted in accelerating plasma ions into interior cathode potential surfaces. This process is undesirable because it results in both a discharge energy loss and in the sputter erosion of these surfaces.

To generate performance curves using Eq. 8, one must be able to specify the behavior of each of the terms on the right-hand-side of this equation as a function of the propellant utilization efficiency.

Plasma Ion Energy Cost

The plasma ion energy cost parameter (ε_p) appearing in Eq. 8 and defined by Eq. 2 reflects all mechanisms of energy loss from the discharge chamber except for the acceleration of ions out of the plasma through the discharge voltage. Specifically, ε_p includes energy losses due to the following phenomena: direct primary electron loss to the anode, Maxwellian electron collection by the anode, excitation of neutral atoms, excitation of ionic states (which will be neglected) and hollow cathode operation. To derive an expression for the plasma ion energy cost as a function of the propellant utilization, a power balance is made on the discharge chamber plasma represented in Fig. 2. The boundary of the control volume for this power balance is defined by the plasma sheath edge. The primary electrons are assumed to be accelerated from a cathode region plasma potential that is V_C volts above cathode potential to the potential of the bulk plasma which is assumed to be near that of the anode. In addition, if it is assumed that only the discharge power supply is used to sustain the discharge, then the rate at which energy is supplied to the discharge chamber plasma by the

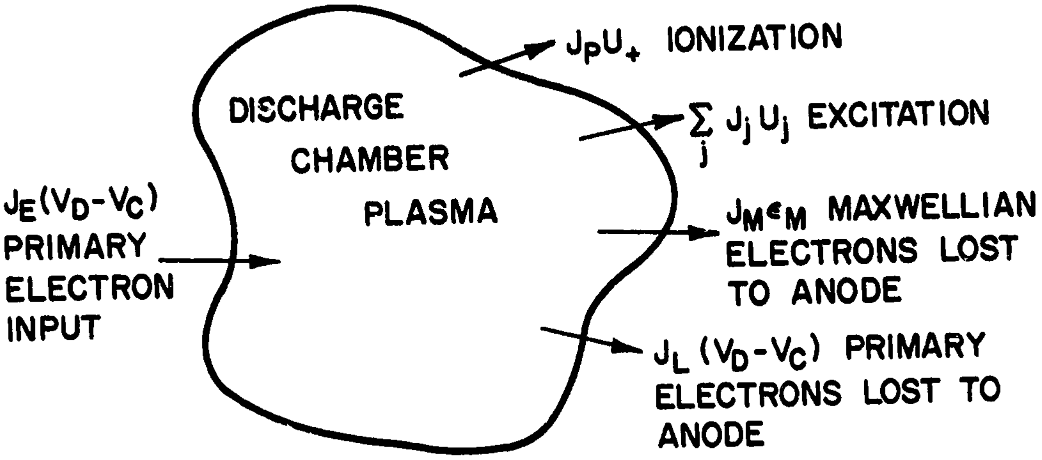

Figure 2. Disharge Plasma Power Balance Schematic

primary electrons is given by $J_E(V_D - V_C)$. The "missing" power J_EV_C is used to operate the hollow cathode.

Energy is lost from the plasma primarily by the flux of four types of energy carriers across the plasma boundaries: ions, photons (emitted by de-excitation of excited propellant atoms), Maxwellian electrons, and primary electrons. The ions and photons are lost to all interior thruster surfaces whereas the Maxwellian and primary electrons are assumed to be lost to the anode surfaces only. In steady state, the rate of energy supplied to the plasma must be equal to the rate at which it is lost, thus,

$$J_E\,(V_D-V_C) = J_PU_+ + \sum_j J_jU_j + J_M\varepsilon_M + J_L(V_D-V_C) \quad , \tag{9}$$

where the summation is over the set of excited neutral states. Dividing Eq. 9 by the ion production current (J_P) and recognizing that the emission current (J_E) related to the discharge current by *,

$$J_E = J_D - (J_C + J_B) \quad , \tag{10}$$

allows Eq. 9 to be written as,

$$\varepsilon_p = U_+ + \frac{\sum_j J_jU_j}{J_P} + \frac{J_M\varepsilon_M}{J_P} + \frac{J_LV_D}{J_P} + \frac{J_EV_C}{J_P} - \frac{J_LV_C}{J_P} \quad , \tag{11}$$

where Eq. 2 has been used. The rate at which the jth excited state is produced (expressed as a current) is given by,

$$J_j = en_on_e \langle\sigma_jv_e\rangle \,\mathcal{V} \quad , \tag{12}$$

---

* Equation 10 is a statement of continuity for the electrons.

where $<\sigma_j v_e>$ represents the product of jth excitation collision cross section and the electron velocity averaged over the entire electron speed distribution - including the primary electrons. Similarly, the ion production current is given by,

$$J_P = en_o n_e <\sigma_+ v_e> \mathcal{V} \quad . \tag{13}$$

Substituting Eqs. 12 and 13 into Eq. 11 yields,

$$\varepsilon_P = \varepsilon_o + \frac{J_M \varepsilon_M}{J_P} + \frac{J_L V_D}{J_P} + \frac{J_E V_C}{J_P} - \frac{J_L V_C}{J_P} \quad , \tag{14}$$

where the parameter ε_o is defined by,

$$\varepsilon_o \equiv U_+ + \frac{\sum_j <\sigma_j v_e> U_j}{<\sigma_+ v_e>} \quad . \tag{15}$$

This parameter accounts for the energy that is expended in ionization and excitation reactions and may be calculated in the manner described by Dugan and Sovie [38]. The third term on the right-hand-side of Eq. 14 may be written as,

$$\frac{J_L V_D}{J_P} = \frac{J_L}{J_E} \frac{J_E V_D}{J_P} = \frac{J_L}{J_E} \varepsilon_P \quad , \tag{16}$$

where the last step was made using Eqs. 2 and 10. The ratio J_L/J is simply the fraction of primary electrons emitted by the cathode which are collected by the anode before having any inelastic collisions. This fraction may be given by the survival equation [39] as,

$$\frac{J_L}{J_E} = e^{-\sigma_o' n_o \ell_e} \tag{17}$$

where ℓ_e is the average distance a primary electron would travel in the discharge chamber before being collected by the anode - assuming it had no inelastic collisions (i.e. the primary electron containment length), σ_o' is the total inelastic collision cross section for electrons at the primary electron energy and n_o is the neutral atom density. Combining Eqs. 14, 16 and 17 yields,

$$\varepsilon_p = \varepsilon_o + \frac{J_M \varepsilon_M}{J_p} + \varepsilon_p e^{-\sigma_o' n_o \ell_e} + \varepsilon_p \frac{V_C}{V_D} - \varepsilon_p \frac{V_C}{V_D} e^{-\sigma_o' n_o \ell_e} \quad . \qquad (18)$$

The current of Maxwellian electrons to the anode may be given as the sum of the secondary electrons liberated in the ionization process and the thermalized primary electrons, thus,

$$J_M = J_p + (J_E - J_L) = J_p + J_E(1-J_L/J_E) \quad . \qquad (19)$$

Using Eqs. 17 and 19 in 18 yields,

$$\varepsilon_p = \varepsilon_o + [J_p + J_E(1-e^{-\sigma_o' n_o \ell_e})]\frac{\varepsilon_M}{J_p} + \varepsilon_p[e^{-\sigma_o' n_o \ell_e} + (1-e^{-\sigma_o' n_o \ell_e})\frac{V_C}{V_D}] \quad . \qquad (20)$$

Finally, using Eqs. 2 and 10 and solving Eq. 20 for ε_p results in,

$$\varepsilon_p = \left(\frac{\varepsilon_o + \varepsilon_M}{1 - \frac{V_C + \varepsilon_M}{V_D}}\right)\left(1 - e^{-\sigma_o' n_o \ell_e}\right)^{-1} \quad . \qquad (21)$$

The factor $1-e^{-\sigma_o' n_o \ell_e}$ may be interpreted as the probability that a primary electron will have an inelastic collision before being collected by the anode. This is analogous to the "fast neutron non-leakage probability" used in nuclear reactor physics [40].

The neutral density (n_o) may be expressed in terms of the propellant flow rate and propellant utilization by equating the rate at which propellant enters and leaves the discharge chamber, i.e.,

$$\dot{m} = J_B + \dot{n}_o \qquad (22)$$

where $\dot{m}$ and $\dot{n}$ are in units of equivalent amperes[+]. The neutral flow rate from the thruster may be expressed using the theory for free molecular flow through a sharp-edged orfice [39],

$$\dot{n}_o = \frac{1}{4} n_o e v_o A_g \, \phi_o \quad . \tag{23}$$

Combining Eqs. 22 and 23 yields,

$$n_o = \frac{4 \, \dot{m}(1-\eta_u)}{e v_o A_g \, \phi_o} \quad , \tag{24}$$

where the propellant utilization defined by $\eta_u \equiv J_B/\dot{m}$ was used. Thus, Eq. 21 may be written as,

$$\varepsilon_p = \varepsilon_p^* \left[1-e^{-C_o \dot{m}(1-\eta_u)} \right]^{-1} \quad , \tag{25}$$

where,

$$C_o \equiv \frac{4\sigma_o' \ell_e}{e v_o A_g \, \phi_o} \quad , \tag{26}$$

and,

$$\varepsilon_p^* \equiv \frac{\varepsilon_o + \varepsilon_M}{1 - \frac{V_C + \varepsilon_M}{V_D}} \quad . \tag{27}$$

Equation 25 is a very simple relationship which can be used to calculate the plasma ion energy cost as a function of the propellant utilization. Experimental results, which will be presented in Chapter IV, indicate that under many conditions the parameters C_o and ε_p^* may be taken to be independent of the propellant utilization.

Substitution of Eq. 25 into Eq. 8 yields the following single equation describing the performance of a given thruster design,

---

[+] Equation 22 is a statement of continuity for the propellant.

$$\varepsilon_B = \frac{\varepsilon_p^*}{f_B\left[1-e^{-C_0\dot{m}(1-\eta_u)}\right]} + \frac{f_C V_D}{f_B} \quad . \tag{28}$$

For design purposes, the parameters f_B and f_C in addition to C_0 and ε_p^* may be taken to be independent of the utilization and flow rate. These parameters do, however, depend strongly on the thruster design. Indeed, these four parameters determine the performance of a given thruster design.

The quantity C_0 reflects the degree to which primary electrons interact with neutral atoms. Thus, it is referred to as the primary electron utilization factor. This factor depends on the quality of the primary electron containment (through ℓ_e), the quality of the containment of neutral atoms (through A_g, ϕ_0 and v_0) and the propellant gas properties (through σ_0' and v_0). Recall that the primary electron containment length ℓ_e may be interpreted as the average distance a primary electron would travel in the discharge chamber before being lost to the anode--assuming it had no inelastic collisions. Magnetic fields in all discharge chamber designs serve the function of increasing this length. Although an effective means of determining ℓ_e remains to be developed, it is believed that this parameter is a function primarily of the thruster geometry, magnetic field configuration and cathode location.

Equation 25 suggests that the plasma ion energy cost should, through the factor C_0, be a function of:

1. The propellant, which determines the total inelastic collision cross section (σ_0') and atomic mass (which affects the thermal neutral velocity, v_0).

2. The wall temperature, which affects the neutral velocity.

3. The transparency of the grids to neutrals (ϕ_o).

4. The area through which the beam is extracted (A_g).

5. The discharge voltage, which determines the primary electron energy and, thus, effects the value of the cross section (σ_o').

The baseline plasma ion energy cost (ε_p^*), defined by Eq. 27, depends on a number of energy loss mechanisms including: the relative amount of energy expended in excitations compared to ionization of neutral atoms through ε_o, the average energy of the Maxwellian electrons which leave the plasma (ε_M) and the efficiency with which the hollow cathode operates.

The cathode efficiency is reflected in the value of V_C which represents the plasma potential from which the electrons are supplied. Inefficient cathode operation results in high values of V_C and correspondingly poor overall thruster performance. For thermionic cathodes $V_C = 0$, however, additional heater power must be supplied to effect its operation. For thrusters equipped with a cathode pole piece/baffle assembly, V_C should be taken as the plasma potential in the cathode discharge region (i.e., the region between the cathode and the baffle). In this case, the power represented by $J_E V_C$ goes into both the operation of the hollow cathode and the operation of the cathode region discharge. The resulting high values of V_C, in this case, would be expected to produce poorer overall thruster performance. Elimination of the separate cathode discharge region should, therefore, improve the performance.

The parameter ε_o , defined by Eq. 15, in general is a function of the entire electron energy distribution including the primary electrons. The parameter ε_p^* (which contains ε_o, see Eq. 27) is, thus, also a function of the electron energy distribution. For plasmas characterized by a Maxwellian plus monoenergetic electron energy distribution, a simple method for the calculation of ε_p^* may be derived. Sample calculations using this method, along with the appropriate collision cross section data, are given in Appendix A. The experimental results given in Chapter IV indicate that, under many conditions, the baseline plasma ion energy cost (ε_p^*) may be taken to be a constant. The calculations given in Appendix A demonstrate that this experimental observation is predicted by the model.

Although the model cannot yet be used to predict the performance of completely new thruster designs, it provides a clear physical picture of the phenomena affecting the performance. Equation 25 describes the plasma ion energy cost in terms of the loss of primary electrons to the anode. At high values of the neutral density parameter, the neutral density in the discharge chamber is large, and the probability is high that all the primary electrons will undergo inelastic collisions with neutral atoms and none will be lost directly to the anode. In this case, the discharge chamber will be producing ions for the minimum or baseline plasma ion energy cost, ε_p^*.

As the beam current is increased (at a constant propellant flow rate), the propellant utilization increases causing the neutral density parameter (and thus the neutral density) to decrease (see Eq. 24). The decrease in neutral density increases the likelihood of a primary electron reaching the anode without having an inelastic collision. This direct loss of primary electron energy increases the overall plasma ion energy cost according to Eq. 25 and consequently increases the beam ion energy cost according to Eq. 28. The shape of the performance curve is largely determined by this direct loss of primary electrons. Thus, any design change which decreases the likelihood of the direct loss of primary electrons (without decreasing the extracted ion fraction) should improve the thruster's performance. The probability of direct primary electron loss is determined through the parameter C_o. This parameter may be increased by either increasing ℓ_e, which makes it harder for primary electrons to escape the plasma, or by making it harder for neutral atoms to escape the discharge chamber.

Calculation of Plasma Properties

The following analysis provides a set of very simple algebraic equations which allow one to calculate the values of the following discharge chamber plasma properties: the average primary electron density, the average primary-to-total electron density ratio, the average Maxwellian electron temperature and the average ratio of the doubly-to-singly charged ion current in the beam. Each of these quantities may be calculated as a function of the propellant flow rate and propellant utilization using only information that would normally be available in the thruster design phase.

Primary Electron Density

This analysis is based on the recognition that all of the energy supplied to the discharge chamber plasma is supplied by the primary electrons. Thus, correctly accounting for the behavior of the primary electrons is essential in determining the average plasma properties. It is assumed that a primary electron can do only one of two things. It can either have an inelastic collision with a neutral propellant atom or it can be lost directly to the anode. For the case where the primary electron has an inelastic collision with a neutral atom, it will produce either an ion or an excited neutral state. After such an inelastic collision, the energy of the primary electron is degraded and it is assumed that it is subsequently thermalized into the Maxwellian electron population. The rate at which primary electrons have inelastic collisions with neutral atoms is given by the difference between the rate at which they are supplied by the cathode (J_E) and the rate at which they are lost directly to the anode (J_L), i.e.,

$$J_E - J_L = J_p' + J_{ex}' \quad , \tag{29}$$

where J_p' is the ion current produced by primary electrons and J_{ex}' is the primary electron induced production rate of excited neutral states expressed as a current. The ion current produced by primary electrons is given by,

$$J_p' = n_o n_p e \sigma_+' \mathcal{V} v_p \quad , \tag{30}$$

where σ_+' is the ionization collision cross section at the primary electron energy. Similarly, the rate of production of excited state atoms induced by primaries is given by,

$$J_{ex}' = n_o n_p e v_p \mathcal{V} \sum_j \sigma_j' \tag{31}$$

where σ_j' is the collision cross section for the jth excited state at the primary electron energy. The fraction of the primary electron-neutral atom inelastic collisions that produce ions is given by,

$$\frac{J_p'}{J_p' + J_{ex}'} = \frac{n_o n_p e v_p \sigma_+' \mathcal{V}}{n_o n_p e v_p \sigma_+' \mathcal{V} + n_o n_p e v_p \mathcal{V} \sum_j \sigma_j'} \tag{32}$$

or,

$$\frac{J_P'}{J_P' + J_{ex}'} = \frac{\sigma_+'}{\sigma_+' + \sum_j \sigma_j'} \quad . \qquad (33)$$

Note that the sum $\sigma_+' + \sum_j \sigma_j'$ Is just the total inelastic collision cross section for primary electron-neutral atom collisions σ_o' . Therefore, Eq. 33 may be written as,

$$\frac{J_P'}{J_P' + J_{ex}'} = \frac{\sigma_+'}{\sigma_o'} \quad . \qquad (34)$$

Multiplying Eq. 34 by the rate at which primary electron-neutral atom collisions occur (Eq. 29) yields the rate at which ions are produced by primary electrons, i.e.,

$$J_P' = (J_E - J_L) \frac{\sigma_+'}{\sigma_o'} \quad . \qquad (35)$$

The term in parentheses in Eq. 35 may be written as,

$$J_E - J_L = J_E (1 - J_L/J_E) \quad . \qquad (36)$$

The quantity J_L/J_E is the fraction of the input primary electron current lost directly to the anode and is given by the survival equation (Eq. 17 written in a slightly different form),

$$\frac{J_L}{J_E} = e^{-C_o \dot{m}(1-\eta_u)} \quad . \qquad (37)$$

Combining Eqs. 2 and 10 yields the following expression for the cathode emission current.

$$J_E = \frac{J_P \varepsilon_P}{V_D} \quad . \qquad (38)$$

Combining Eqs. 25, 35, 36, 37 and 38 yields the following expression for the ion current produced by primary electrons,

$$J_P' = \frac{J_P \varepsilon_P^* \sigma_+'}{V_D \sigma_o'} \quad . \tag{39}$$

Dividing both sides of this equation by J_P yields an expression for the ratio of ion current produced by primaries to the total ion current produced,

$$\frac{J_P'}{J_P} = \frac{\varepsilon_P^* \sigma_+'}{V_D \sigma_o'} \quad . \tag{40}$$

Since the ratio J_P'/J_P cannot be greater than one, Eq. 40 provides a theoretical limit for the maximum value of ε_P^* , i.e.,

$$(\varepsilon_P^*)_{max} = \frac{V_D \sigma_o'}{\sigma_+'} \quad . \tag{41}$$

The total ion current produced may be expressed in terms of the beam current by using the definition of the extracted ion fraction (Eq. 6),

$$J_P = J_B/f_B \quad . \tag{42}$$

In addition, using the definition of the propellant utilization the beam current may be written as,

$$J_B = \dot{m}\eta_u \quad . \tag{43}$$

Combining Eqs. 39, 42 and 43 yields,

$$J_P' = \frac{\dot{m}\eta_u \varepsilon_P^* \sigma_+'}{f_B V_D \sigma_o'} \quad . \tag{44}$$

Finally, equating Eq. 30 to Eq. 44 and solving for the primary electron density (n_p) yields,

$$n_p = \left[\frac{\varepsilon_p^* A_g \phi_o v_o}{4 v_p + f_B V_D \sigma_o'}\right]\left(\frac{\eta_u}{1-\eta_u}\right) , \qquad (45)$$

where Eq. 24 was used for the neutral density. Equation 45 provides an expression for the average primary electron density as a function of the propellant utilization. Remarkably, this expression does not depend on either the propellant mass flow rate or the primary electron utilization factor, both of which cancelled out in the analysis. The term in the square brackets should be roughly a constant for a given thruster design, propellant gas and discharge voltage. A reasonable estimate for each of the terms in the square bracket should be possible for a thruster being designed (assuming a method is developed for the determination of the extracted ion fraction).

Primary-to-Total Electron Density Ratio

Assuming quasi-neutrality, the average ion density (n_i) is equal to the average total electron density ($n_i = n_p + n_M$). In addition, the average ion density is related to the beam current by [41].

$$J_B = 0.6 n_i e v_b A_g \phi_i \quad . \qquad (46)$$

Solving this equation for n_i yields,

$$n_i = \frac{J_B}{0.6 e v_b A_g \phi_i} \qquad (47)$$

where ϕ_i is the transparency of the screen grid to ions and v_b is the

Bohm velocity. Dividing Eq. 45 by 47 and using Eq. 43 yields the following expression for the average ratio of primary-to-total electron density,

$$\frac{n_p}{n_i} = \left[\frac{0.15e\varepsilon_p^* v_b A_g^2 \phi_o \phi_i}{v_p V_D f_B \mathcal{V} \sigma_o'}\right] \frac{1}{\dot{m}(1-\eta_u)} \quad . \tag{48}$$

This equation indicates that the average primary-to-total electron density ratio should be a function of the neutral density parameter, $\dot{m}(1-\eta_u)$. As was the case for Eq. 45, the combination of parameters in the square brackets of Eq. 48 should be roughly a constant for a given thruster design, propellant and discharge voltage. Equation 48 also indicates that, all else being equal, increasing the extracted ion fraction should decrease the primary-to-total electron density ratio.

Primary-to-Maxwellian Electron Density Ratio

Once the primary-to-total electron density ratio is calculated, using Eq. 48 the primary-to-Maxwellian electron density ratio (n_p/n_M) may be calculated from the following equation,

$$\frac{n_p}{n_M} = \frac{n_p/n_i}{1-n_p/n_i} = \frac{1}{n_i/n_p - 1} \quad . \tag{49}$$

Maxwellian Electron Temperature

The total ion current produced (J_P) is the sum of the ion current produced by primary electrons (J_P') and that produced by Maxwellian electrons ($J_{P,M}$) . (50)

The ion current produced by primary electrons is given by Eq. 30 and that produced by Maxwellian electrons is given by,

$$J_{P,M} = n_o n_M e \langle \sigma_+ v_e \rangle_M \mathcal{V} \quad , \tag{51}$$

where the quantity $\langle \sigma_+ v_e \rangle_M$ represents the product of the electron velocity and ionization collision cross section averaged over the Maxwellian electron energy distribution. This quantity is the Maxwellian electron rate factor for the production of ions and is given the symbol Q_o^+ , i.e.,

$$Q_o^+ = \langle \sigma_+ v_e \rangle_M \quad . \tag{52}$$

Combining Eqs. 50 to 52 yields,

$$J_p = n_o n_p e v_p \sigma_+' \mathcal{V} + n_o n_M e Q_o^+ \mathcal{V} \quad . \tag{53}$$

Using Eqs. 42 and 43 in Eq. 53 and solving for Q_o^+ gives,

$$Q_o^+ = \frac{\dot{m} n_u}{f_B n_o n_M e \mathcal{V}} - \frac{n_p}{n_M} v_p \sigma_+' \quad . \tag{54}$$

Substituting for the neutral density using Eq. 24 yields,

$$Q_o^+ = \frac{v_o A_g \phi_o}{4 f_B n_M \mathcal{V}} \left(\frac{n_u}{1-n_u} \right) - \frac{n_p}{n_M} v_p \sigma_+' \quad . \tag{55}$$

The Maxwellian electron density, appearing in Eq. 55, may be written as,

$$n_M = \left(\frac{n_M}{n_p} \right) n_p \quad . \tag{56}$$

Substituting this into Eq. 55 yields,

$$Q_o^+ = \left[\left(\frac{n_u}{1-n_u} \right) \left(\frac{v_o A_g \phi_o}{4 f_B \mathcal{V}} \right) \frac{1}{n_p} - \sigma_+' v_p \right] \frac{n_p}{n_M} \quad . \tag{57}$$

Equation 45 provides an expression for the primary electron density. Using this in Eq. 57 yields,

$$Q_o^+ = \left(\frac{v_p V_D \sigma_o'}{\varepsilon_p^*} - \sigma_+' v_p \right) \frac{n_p}{n_M} \quad . \qquad (58)$$

The primary-to-Maxwellian electron density ratio may be found using Eqs. 48 and 49. Substituting these equations into Eq. 58 yields the following expression for the average Maxwellian electron rate factor for ion production,

$$Q_o^+ = \frac{v_p \sigma_+' \left(\frac{V_D \sigma_o'}{\varepsilon_o^* \sigma_+'} - 1 \right)}{\left[\frac{v_p V_D \sigma_o' \forall}{0.15 e \varepsilon_p^* v_o v_b A_g{}^2 \phi_o \phi_i} \right] \dot{m}(1-\eta_u) - 1} \quad . \qquad (59)$$

Equation 59 provides an expression for the Maxwellian electron ionization rate factor as a function of the neutral density parameter, $\dot{m}(1-\eta_u)$. Once this rate factor has been calculated, it can be compared to a tabulation of rate factors versus electron temperature for the given propellant to determine the appropriate Maxwellian electron temperature. Equation 59 indicates that the average Maxwellian electron temperature should increase with decreasing values of the neutral density parameter.

Double Ion Production

In the previous analysis, the production of doubly charged ions was neglected. In this section, a simple formulation for the ratio of doubly-to-singly charged ion current in the beam is developed. The production rate of singly charged ions expressed as a current is given by,

$$J_p^+ = (n_o n_p P_o^+ + n_o n_M {}_o^+)\, e\, \mathcal{V} \quad , \tag{60}$$

where Q_o^+ is the Maxwellian rate factor for the production of single ions from ground state neutral atoms and P_o^+ is the primary electron rate factor also for the production of single ions from ground state neutrals. Similarly, the production rate of doubly charged ions expressed as a current is given by,

$$J_p^{++} = (n_o n_M {}_o^{++} + n_o n_p P_o^{++} + n_+ n_M {}_+^{++} + n_+ n_p P_+^{++})\, 2e\, \mathcal{V} \quad , \tag{61}$$

where n_+ is the singly charged ion density, Q_o^{++} and P_o^{++} are the Maxwellian and primary electron rate factors for double ion production from ground state neutrals, respectively, and Q_+^{++} and P_+^{++} are the corresponding rate factors for double ion production from ground state ions. Dividing Eq. 61 by 60 yields,

$$\frac{J_p^{++}}{J_p^+} = \frac{2(Q_o^{++} + \frac{n_p}{n_M} P_o^{++})}{Q_o^+ + \frac{n_p}{n_M} P_o^*} + \frac{\frac{2n_+}{n_o} (Q_+^{++} + \frac{n_p}{n_M} P_+^{++})}{Q_o^+ + \frac{n_p}{n_M} P_o^+} \quad . \tag{62}$$

Assuming that the doubly charged extracted ion fraction (f_B^{++}) is equal to the singly charged extracted ion fraction (f_B^+) implies that,

$$\frac{J_p^{++}}{J_p^+} = \frac{J_B^{++}/f_B{}^{++}}{J_B^+/f_B^+} = \frac{J_B^{++}}{J_B^+} \quad , \tag{63}$$

where J_B^{++}/J_B^+ is the average ratio of doubly-to-singly charged ion current in the beam. Combining Eqs. 62 and 63 yields,

$$\frac{J_B^{++}}{J_B^+} = \frac{2(Q_o^{++} + \frac{n_p}{n_M} P_o^{++})}{Q_o^+ + \frac{n_p}{n_M} P_o^+} + \frac{\frac{2n_+}{n_o} (Q_+^{++} + \frac{n_p}{n_M} P_+^{++})}{Q_o^+ + \frac{n_p}{n_M} P_o^+} \quad . \tag{64}$$

The singly charged ion density (n_+) may be conservatively approximated by assuming the beam current is made up entirely of singly charged ions, thus,

$$n_+ = n_i = \frac{J_B}{0.6 e v_b A_g \phi_i} \quad . \tag{65}$$

In addition, using Eq. 43 for the beam current and Eq. 24 for the neutral density allows Eq. 64 to be written as,

$$\frac{J_B^{++}}{J_B^{+}} = \frac{2\left(Q_o^{++} + \frac{n_p}{n_M} P_o^{++}\right)}{Q_o^{+} + \frac{n_p}{n_M} P_o^{+}} + 0.83\left(\frac{v_o}{v_b}\right)\left(\frac{\phi_o}{\phi_i}\right)\left[\frac{Q_+^{++} + \frac{n_p}{n_M} P_+^{++}}{Q_o^{+} + \frac{n_p}{n_M} P_o^{+}}\right]\left(\frac{n_u}{1-n_u}\right). \tag{66}$$

The first term on the right-hand-side of Eq. 66 represents the production of double ions from ground state neutral atoms. This term depends on the thruster geometry only through the primary-to-Maxwellian electron density ratio (n_p/n_M) which is given by Eqs. 48 and 49 and the Maxwellian electron temperature (Eq. 59). The second term in Eq. 66 represents double ion production from singly charged ions. This term is strongly dependent on the propellant utilization. The rate factors Q_o^{++} and Q_+^{++} may be determined once the rate factor Q_o^{+} is calculated from Eq. 59.

IV. EXPERIMENTAL PROCEDURES AND RESULTS

Apparatus

For this investigation, the ion sources shown schematically in Figs. 3a and b were designed and built. Each of these sources normally produces a 12 cm dia. ion beam and provides the capability for measuring the distribution of ion currents to the beam, screen grid and internal thruster surfaces (with the exception of the anode).

The magnetic field for the experimental ion source in Fig. 3a is established through the use of an electromagnet located on the upstream centerline of the discharge chamber and a number of 1.9 cm x 1.3 cm x 0.5 cm samarium cobalt permanent magnets. These permanent magnets are arranged end-to-end to form ring magnets of alternate polarity in the manner suggested by Fig. 3a. The flux density at the surface of the magnets is 0.27T and the magnets are attached to the steel discharge chamber housing by their own magnetic attraction. This arrangement allows the ion source magnetic field configuration to be altered quickly and easily by simply adding, removing or changing the position of the magnets. Although many different configurations were tested, the results obtained were all similar, thus, only those obtained using the configurations shown in Figs. 3a and 3b will be presented. For these configurations, the upstream magnet ring is covered with a strip of 0.13 mm thick steel insulated from the magnets themselves by a strip of 0.25 mm thick flexible mica. This is done so that the surface of this strip can be

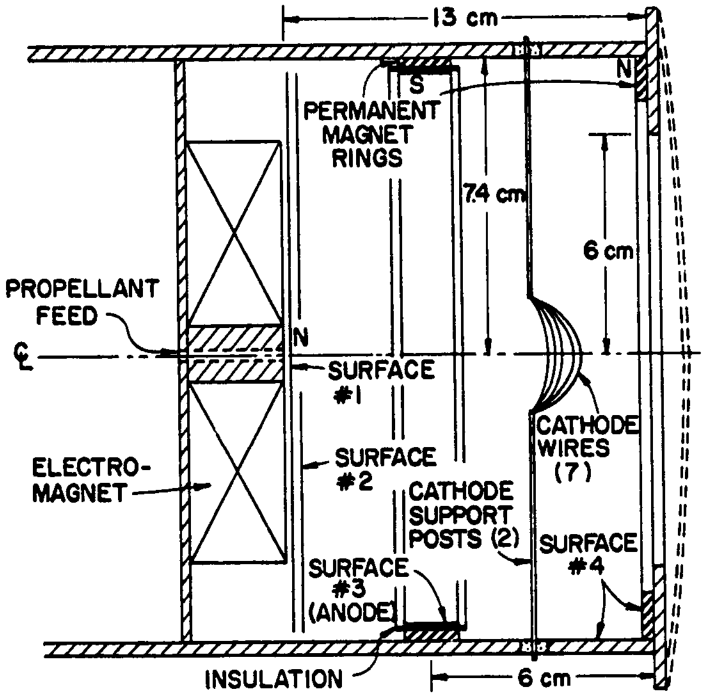

Figure 3a. Ring Cusp Ion Source Schematic - Configuration I

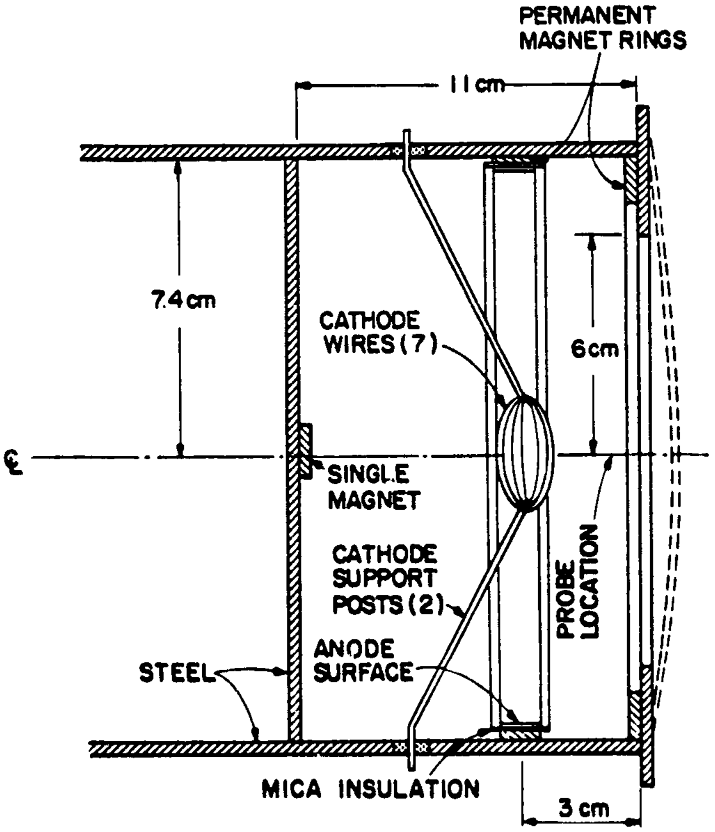

Figure 3b. Ring Cusp Ion Source Schematic - Configuration II

maintained at anode potential while the rest of the thruster body is biased negative of cathode potential. The downstream magnet ring is uncovered. The magnetic flux density at the surface of the electromagnet for the configuration of Fig. 3a can be adjusted from zero to approximately 0.2 T by adjusting the magnet current from zero to 124 A.

The main discharge chamber cathodes, for both configurations, consist of seven 0.25 cm dia. tungsten wires connected in parallel and supported by two support posts that are electrically isolated from the thruster body. Each cathode wire is approximately 2.8 cm long so the total cathode length exposed to the plasma is about 19.6 cm. These seven short wires in parallel are used to minimize the voltage drop across the cathode. A voltage drop less than 3 v at the maximum heater current was achieved with this system. The small voltage drop across the cathode results in a primary electron energy distribution that more closely resembes the monoenergetic distribution produced by a hollow cathode. The cathode wires were heated using direct currents in the range 6 to 8 A per wire. Tests on the configuration of Fig. 3a, were conducted using argon, krypton and xenon propellants. Discharge voltages were varied from 30 to 50 v for argon and 20 to 40 v for krypton and xenon. The discharge current was adjusted through the range of 0.5 to 5 A by controlling the heating current through the refractory cathode wires.

Two ion accelerator systems were used in this study. The first accelerator system consisted of a set of dished small hole accelerator grids (SHAG) with a cold grid separation of 0.75 mm and screen and accelerator grid physical open area fractions of 0.68 and 0.30, respectively. The second system consisted of a set of dished large hole accelerator grids (LHAG) with a cold grid separation of 0.75 mm, and screen and accelerator grid physical open area fractions of 0.68 and 0.57, respectively. Both accelerator systems were normally masked to produce a 12 cm diameter beam. One series of test was conducted, however, with the SHAG set masked to produce a 6 cm diameter beam. For the 12 cm dia. beam tests, flow rates for both argon and krypton were varied from 500 to 1500 mA eq. and for xenon from 250 to 1000 mA eq. For the 6 cm dia. beam test, the flow rates were varied from 125 to 500 mA eq.

The configuration of Fig. 3b is similar to that of Fig. 3a except that the electromagnet assembly has been replaced by a permanent magnet attached to the steel backplate. In addition, the source of Fig. 3b is 2 cm shorter than the one in Fig. 3a and the upstream magnet ring is positioned only 2.5 cm from the downstream end rather than 6 cm.

This source was equipped with two Langmuir probe assemblies. The first probe consisted of a 0.76 mm dia. tantalum wire, 4.32 mm long, supported from a quartz tube insulator. This probe was positioned along the thruster centerline approximately half way between the cathode assembly and the screen grid as suggested in Fig. 3b. The second probe was a square piece of steel, 1 cm on a side and 0.127 mm thick that was positioned on the surface of the upstream magnetic ring. This probe was insulated from the magnet ring with a piece of 0.13 mm thick flexible mica.

Measurements of the doubly and singly charged ion beam components were made on the thruster centerline using a collimating $\vec{E} \times \vec{B}$ momentum analyzer. Details of the use of this probe are given elsewhere [42].

Tests were conducted on the configuration of Fig. 3b using both argon and xenon propellants. Argon propellant flow rates were varied over the range 350 to 1500 mA eq. at discharge voltages of 30 to 50 v. Xenon propellant flow rates were varied over the range 250 to 1000 mA eq. at discharge voltages of 20 to 40 v. Discharge currents for both propellants were varied over 0.5 to 4.0 A.

All tests were conducted in a 1.2 m dia. x 4.6 m long vacuum test facility. Indicated tank pressures ranged from ∿ 2×10^{-6} Torr with no flow to ∿ 3×10^{-5} Torr at a flow rate of 1500 mA eq. of krypton.

Procedure

The following set of experiments, conducted using the thruster configuration of Fig. 3a, was designed to test the suitability of the model developed in Chapter III to predict the functional dependence of the plasma ion energy cost, ε_p, on the neutral density parameter, $\dot{m}(1-\eta_u)$. The model predicts that the plasma ion energy cost should behave according to Eq. 25 with the primary electron utilization factor (C_o) and the baseline plasma ion energy cost (ε_p^*) given by Eqs. 26 and 27, respectively. The value of ε_p may be determined experimentally through the use of Eq. 2, which is repeated here for convenience,

$$\varepsilon_p = \frac{[J_D - (J_C + J_B)]V_D}{J_P}$$

Note that the power used to operate the thermionic cathodes is not included in Eq. 2. In order to use Eq. 2, one must be able to measure each of the parameters on the right-hand-side of the equation. Measurement of the discharge current, discharge voltage and beam current is straight forward, and was accomplished using the experimental instrumentation described in Appendix B.

To measure the ion currents J_C and J_P, the thruster configuration of Fig. 3a was operated with only the upstream magnet ring at anode potential. All other interior discharge chamber surfaces (with the exception of the cathode support posts) were biased approximately 30 v negative of cathode potential to repel the discharge chamber electrons. At this bias, the current to these surfaces consists only of the incoming ion current. If the ion current to the cathode support posts and cathode wires is neglected, then the ion current measured in the manner described above is equal to J_C.

To determine J_P, it is noted that the total ion production current is the sum of the ion currents leaving the plasma as given by Eq. 4. Since the anode is exposed to the plasma only at a magnetic field cusp, the effective area for ion loss to this surface is expected to be less than the physical area [43-46]. Rough calculations indicate that the ion current to the anode with this configuration should be less than a few precent of the total production current. Thus, J_P may be approximated as the sum of the ion currents to the beam (including the impingement current) and to the negatively biased discharge chamber surfaces (including the screen grid).

Complete sets of data consisting of the beam current, propellant flow rate, propellant utilization and total ion production current were collected over the range of operating conditions discussed earlier with the electromagnetic current held constant at 57 A for the thruster of Fig. 3a. At each condition tested, the thruster was operated at flow rates of 500, 750, 1000 and 1500 mA eq. for argon and krypton propellants, and 250, 500, 750 and 1000 mA eq. for xenon. At each flow rate, the discharge voltage was held constant while the discharge current was varied. Increasing the discharge current, increases the beam current and propellant utilization, thus causing the neutral density parameter $\dot{m}(1-\eta_u)$ to decrease. By operating in this manner, the full range of neutral density parameters from close to zero to nearly 1500 mA eq. could be investigated. Thus, the plasma ion energy cost was determined from Eq. 2 for a wide range of operating conditions. The extracted ion fraction, f_B, defined by Eq. 6, was also computed from measured ion currents over this same range of conditions.

A second set of experiments was performed using the thruster configuration of Fig. 3b. These tests were designed to investigate the ability of the model to predict the behavior of various plasma properties with variations in thruster operating conditions. The procedure for these tests was the same as for the previous set with the addition that Langmuir probe measurements of the plasma properties on the thruster centerline and at the anode surface were made at each operating point tested. The ratio of doubly to singly charged ion beam currents along the thruster centerline were also measured at each operating condition, using $\vec{E} \times \vec{B}$ probe.

Experimental Results

Plasma Ion Energy Cost

Measurement of the plasma ion energy cost, for operation of the thruster configuration of Fig. 3a with argon propellant at a 50 v discharge over the range of neutral flow rates from 500 to 1500 mA eq., yielded the results shown in Fig. 4a. Here, the measured values of the

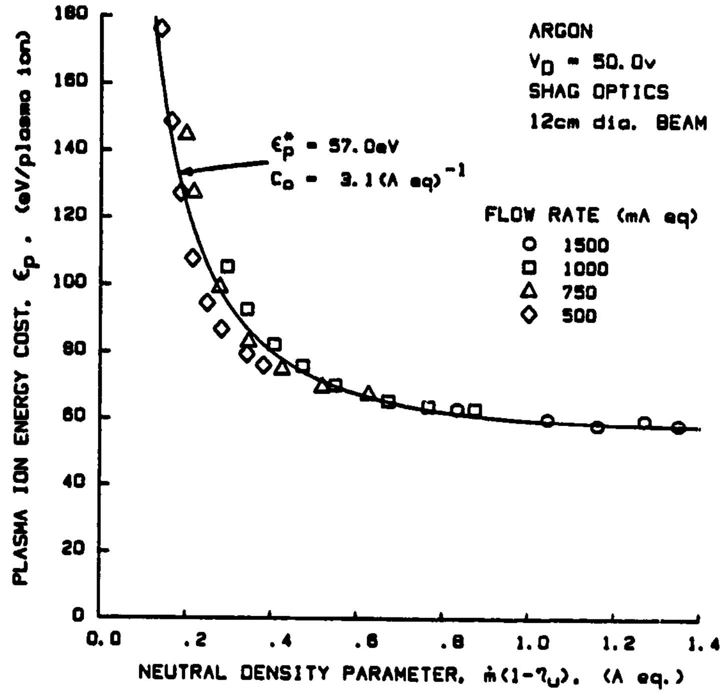

Figure 4a. Plasma Ion Energy Cost Curve - Configuration I

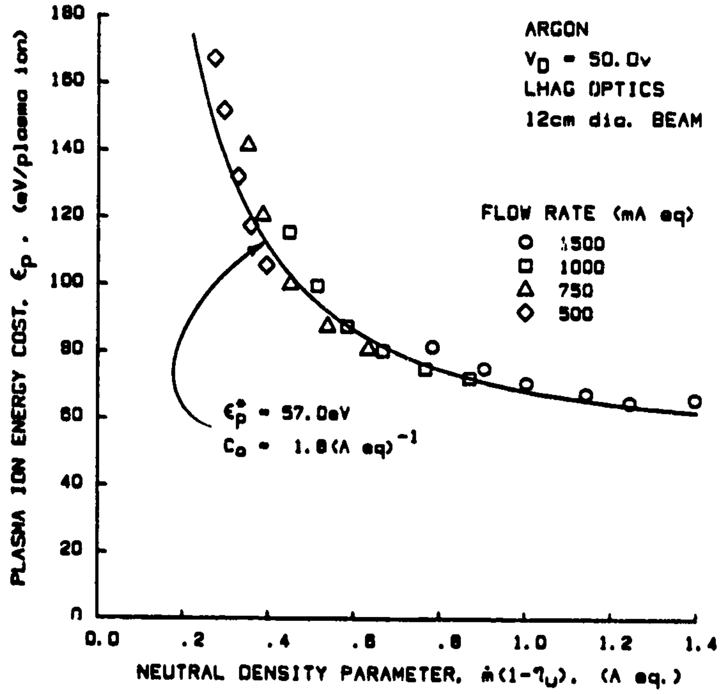

Figure 4b. Plasma Ion Energy Cost Curve for High Accelerator Grid Transparency to Neutral Atoms - Configuration I

plasma ion energy cost (ε_p) are plotted as a function of the neutral density parameter $\dot{m}(1-\eta_u)$, as suggested by Eq. 25. The solid line in Fig. 4a is the curve given by Eq. 25 when the parameters C_o and ε_p^* have been selected to give the best fit to the data. The parameter ε_p^* was taken to be the value of ε_p measured at large values of the neutral density parameter. The justification for this selection can be understood by considering Eq. 25, which shows that when $C_o\ \dot{m}(1-\eta_u)$ is large, the exponential term is small compared to unity and one obtains $\varepsilon_p = \varepsilon_p^*$. Having established the value of the baseline plasma ion energy cost, the value of the primary electron utilization factor (C_o) is varied until the best fit is obtained. The agreement between the functional form of Eq. 25 and the experimental data is seen to be quite good. This indicates that the parameters C_o and ε_p^* may be taken to be independent of the neutral density parameter.

A value of $C_o = 3.1(\text{A eq.})^{-1}$ which is applicable to the ion source of Fig. 3a operating at the conditions defined in the legend for Fig. 4a has now been established. New values of primary electron utilization factor, applicable to other operating conditions, may now be calculated from this value using Eq. 26. For example, changing grid sets from SHAG to LHAG should change the value of C_o through the parameter ϕ_o which is the effective transparency of the grids to neutral atoms. This effective transparency parameter may be calculated for each grid set according to the equation,

$$\phi_o = \frac{\phi_s \phi_a}{\phi_s + \phi_a} \tag{66}$$

where ϕ_s and ϕ_a are the modified transparencies for the screen and accelerator grids, respectively. These modified transparencies may be calculated as the physical open area fraction of a grid times the appropriate Clausing factor [47]. For the two grid sets used in this study,

$$(\phi_o)_{SHAG} = 0.16, \quad (\phi_o)_{LHAG} = 0.27 \quad . \tag{67}$$

Thus, the new value of the primary electron utilization factor applicable to the LHAG optics with all other conditions held constant is given by,

$$(C_o)_{new} = \frac{(\phi_o)_{SHAG}}{(\phi_o)_{LHAG}} (C_o)_{Fig.\ 4a} \quad , \tag{68}$$

which yields $(C_o)_{new} = 1.8\ (A\ eq.)^{-1}$

The measured values of ε_p , obtained under the same set of conditions defined in the legend of Fig. 4a, except for the change in optics from SHAG to LHAG, yielded the results shown by the data points in Fig. 4b. The solid line is the prediction of the model based on the value of C_o calculated from Eq. 68. The value of the baseline plasma ion energy cost was held constant at $\varepsilon_p^* = 57$ eV since changing the optics should not affect this parameter. The degree of agreement between the data points and the curve in Fig. 4b shows clearly that the model correctly predicts the variation in the plasma ion energy cost with the neutral density parameter when the grid system transparency to neutrals is changed.

The same procedure of calculating a new value of the primary electron utilization factor from the old value according to Eq. 26 was followed for the analysis of the data displayed in Figs. 5a and 5b. For the data in Fig. 5a, the thruster was operated with krypton

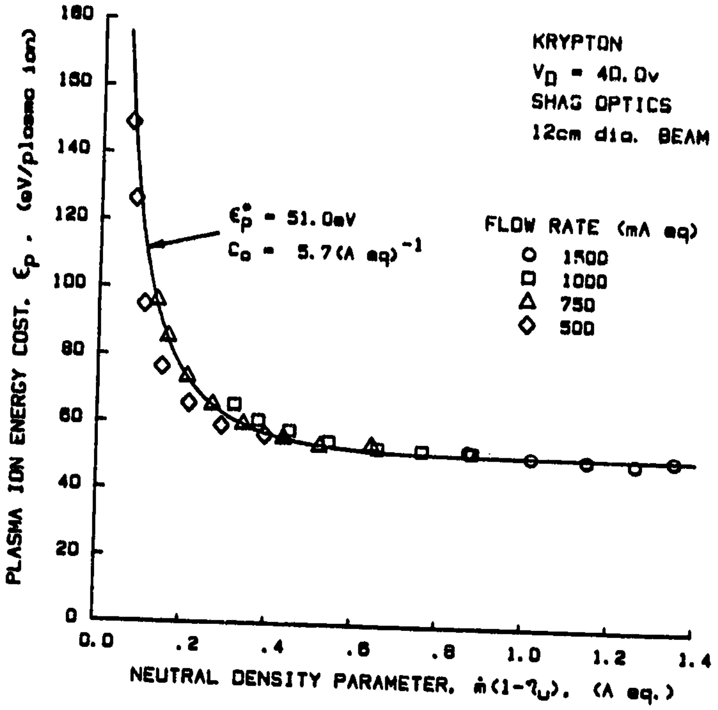

Figure 5a. Plasma Ion Energy Cost Curve for Krypton - Configuration I

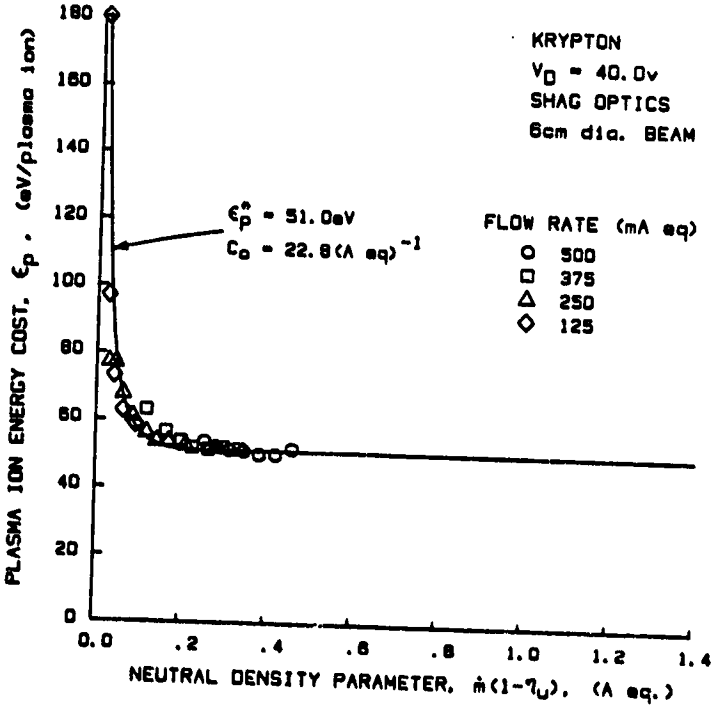

Figure 5b. Plasma Ion Energy Cost Curve for Small Diameter Ion Beam - Configuration I

propellant and SHAG optics at a discharge voltage of 40 v. The primary electron utilization factor corresponding to this operating condition was calculated using the value of C_0 obtained from Fig. 4a together with Eq. 26 in the form,

$$(C_0)_{new} = \frac{(\sigma_0')_{Kr}}{(\sigma_0')_{Ar}} \sqrt{\frac{M_{Kr}}{M_{Ar}}} \, (C_0)_{Fig.\ 4a} \quad . \tag{69}$$

In this case, both the change in propellant properties and the change in discharge voltage must be accounted for. That is, $(\sigma_0')_{Kr}$ is the total inelastic collision cross section for 40 eV primary electron-krypton atom collisions, whereas $(\sigma_0')_{Ar}$ refers, in this case, to 50 eV primary electron-argon atom collisions. The cross section data needed in this equation were obtained from de Heer, et. al [48]. The new value of the primary electron utilization factor calculated from Eq. 69 was $C_0 = 5.7\ (\text{A eq.})^{-1}$ and the corresponding prediction of the model is compared to the measured values in Fig. 5a. A new value of the baseline plasma ion energy cost (ε_p^*) was also required to fit the data of Fig. 5a since this parameter is a function of both the discharge voltage and the propellant type. This new value was selected in the manner suggested previously as the measured plasma ion energy cost at high neutral density levels. These data indicate that the model works as well for operation with krypton propellant as it does for argon.

From Eq. 26, it is seen that the primary electron utilization factor depends inversely on the area of the grids through which the beam is extracted, A_g . This area may be varied without changing the discharge chamber diameter by masking down the screen grid to produce ion beams of different cross sectional areas. In this case, the screen grid for the SHAG optics set was masked down from a beam diameter of 12 cm to one of 6 cm. This four fold reduction in beam area should produce a corresponding four fold increase in primary electron utilization factor. Taking C_0 for Fig. 5a and multiplying by four yields the new value of $C_0 = 22.8$ (A eq.)$^{-1}$. The model prediction for the plasma ion energy cost versus neutral density parameter curve, obtained using this value of C_0, is compared to the measured values of these quantities in Fig. 5b. Remarkably, the agreement between the model and the experiment is excellent. Similar agreement was obtained for operation with argon using the masked down grid set.

Measurements of the plasma ion energy cost variation with the neutral density parameter were also made on the thruster configuration of Fig. 3b. Some of the results obtained with this configuration are shown in Figs. 6a, 6b, 7a and 7b. The data in Fig. 6a was obtained with argon propellant, a discharge voltage of 50 v and a range of propellant flow rates from 350 to 1500 mA eq. Excellent agreement between the model and the experimental data was obtained by taking $\varepsilon_p^* = 59$ eV and $C_0 = 4.0$ (A eq.)$^{-1}$. The value of $\varepsilon_p^* = 59$ eV, obtained with this configuration, agrees well with the value of $\varepsilon_p^* = 57$ eV obtained with the other configuration for operation with argon at a discharge voltage of 50 v. The slightly higher value of ε_p^* for the configuration of Fig. 3b is believed to be the result of the shorter discharge chamber length causing a slightly higher fraction of ion current to go to the anode surface and cathode support posts.

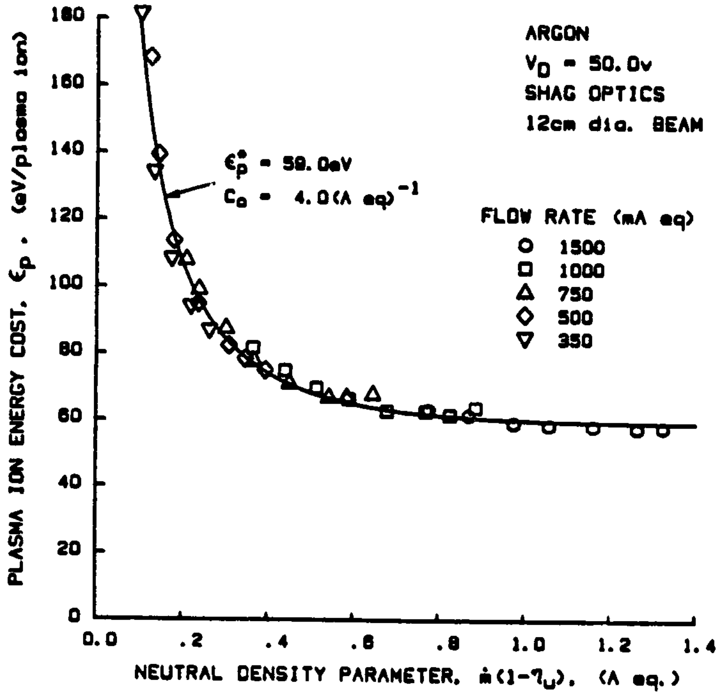

Figure 6a. Plasma Ion Energy Cost Curve - Configuration II

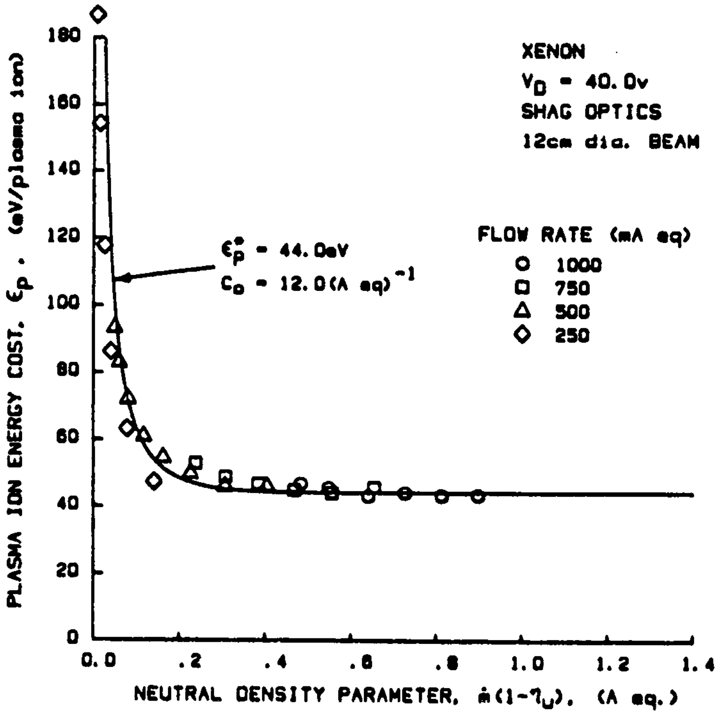

Figure 6b. Plasma Ion Energy Cost Curve for Xenon - Configuration II

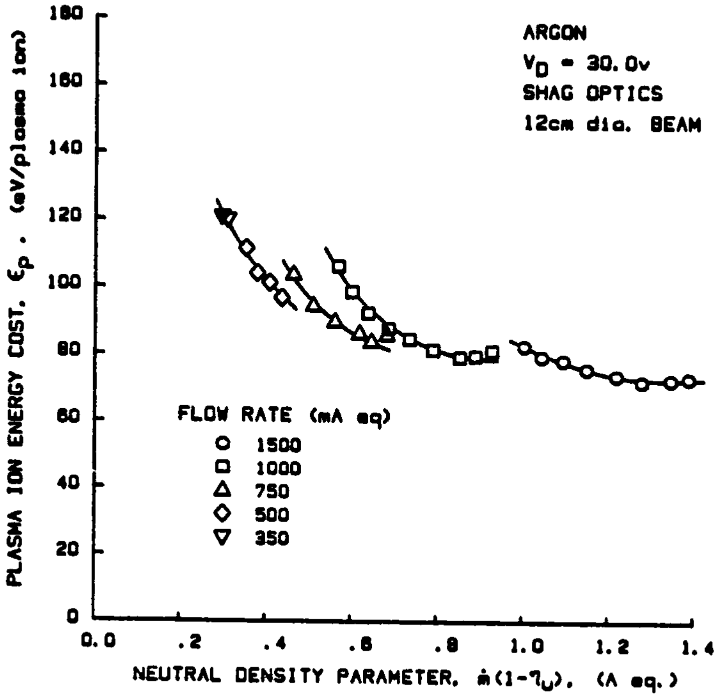

Figure 7a. Plasma Ion Energy Cost Variation at Low Discharge Voltage - Configuration II

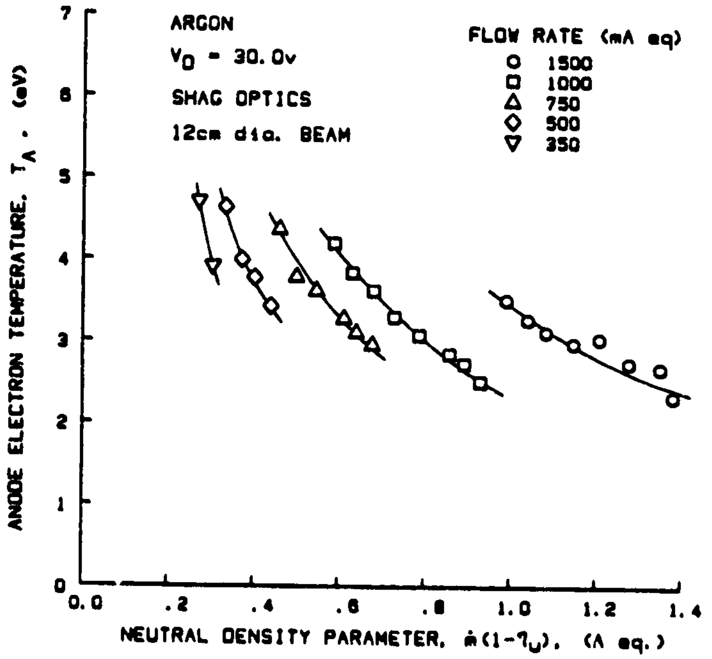

Figure 7b. Anode Electron Temperature Variation at Low Discharge Voltage - Configuration II

From the value of C_o in Fig. 6a, a new value of C_o applicable to this configuration operating on xenon propellant at a discharge voltage of 40 v may be calculated using Eq. 26. The results of this calculation, together with the experimental results, are given in Fig. 6b. For these data, the neutral density parameter has been corrected for presence of doubly charged ions in the beam. Again the value of ε_p^* was chosen in the manner described above. Clearly, the model agrees well with the measured results. Equations 25 and 26 have now been demonstrated to describe correctly the effects of variations in the plasma ion energy cost resulting from changes in propellant flow rate, propellant utilization, effective grid transparency to neutral atoms, beam extraction area, discharge voltage, and propellant gas (Ar, Kr and Xe). In addition, other experiments indicate that the model correctly predicts the change in thruster performance resulting from a change in the effective discharge chamber wall temperature [36]. The model has also been shown to work wall on line cusp thruster geometries [35].

For operation at low discharge voltages, however, the situation is quite different as seen in Fig. 7a. The data in this figure were taken using argon propellant, a discharge voltage of 30 v and the thruster configuration of Fig. 3b. Here, a systematic difference in the data taken at different propellant flow rates is observed. Clearly, a single equation such as Eq. 25 is not sufficient to explain this behavior if C_o and ε_p^* are taken to be independent of the propellant flow rate and propellant utilization. This systematic difference of the plasma ion energy cost curves, measured at different flow rates, is believed to result from changes in the baseline plasma ion energy cost (ε_p^*) which occur at low discharge voltages.

These changes, in turn, result from the dependence of the baseline plasma ion energy cost on the average energy of a Maxwellian electron collected by the anode, ε_M (see Eq. 27). The value of ε_M, however, depends on the Maxwellian electron temperature at the anode. Measured values of the electron temperature, made using the Langmuir probe positioned on the surface of the anode magnet ring, are shown in Fig. 7b. These data were taken under operating conditions identical to those used for the collection of the data in Fig. 7a. The data in Fig. 7b clearly indicate a systematic difference in electron temperature at the anode for different propellant flow rates. For a given value of the neutral density parameter, these data show that the electron temperature at the anode increases with increasing propellant flow rate. Higher electron temperatures at the anode correspond to higher values of ε_p^* because of the increased loss of energy from the plasma in the form of Maxwellian electrons. Because the ratio ε_M/V_D appears in the equation for ε_p^* , changes in ε_M become increasingly important at low discharge voltages.

The systematic difference in the curves of electron temperature versus neutral density parameter observed in Fig. 7b is not predicted by the model (as given by Eq. 59). Thus, some additional mechanism for the transfer of energy from the primary electrons to the Maxwellian electrons, other than that considered in the model, must become important at low discharge voltages. This mechanism is believed to be the direct thermalization of the primary electrons as the result of electron-electron collisions. The collision cross section for primary-Maxwellian electron collisions increases rapidly with decreasing primary electron energy. This is consistent with the observation that the separation between the electron temperature curves taken at different propellant flow rates (such as those in Fig. 7b) increases with decreasing primary electron energy (i.e., discharge voltage).

Extracted Ion Fraction

Aside from the plasma ion energy cost, the other parameter which has a major affect on thruster performance is the extracted ion fraction, f_B. It is of little use to create ions efficiently in the discharge chamber if the fraction of these ions extracted into the beam is small. The extracted ion fraction, which is defined in Eq. 6 as the ratio of the beam current to the total ion current produced, was measured for both thruster configurations over the range of operating conditions discussed earlier.

The resulting extracted ion fraction data, obtained on the thruster configuration of Fig. 3a, are shown in Figs. 8a and b. In Fig. 8a, the value of f_B are given versus the neutral density parameter for operation with argon propellant at discharge voltages of 30 and 50 v over a range of propellant flow rates from 500 to 1500 mA eq. These data indicate that the extracted ion fraction, while being relatively independent of neutral density, does tend to be slightly greater at lower discharge voltages. Data taken under the same conditions, but at a 40 v discharge voltage, fall between the two curves shown in Fig. 8a.

The extracted ion fractions for argon propellant are compared to those for krypton propellant at a discharge voltage of 40 v in Fig. 8b, The values of f_B for argon are seen to be generally slightly higher than those for krypton.

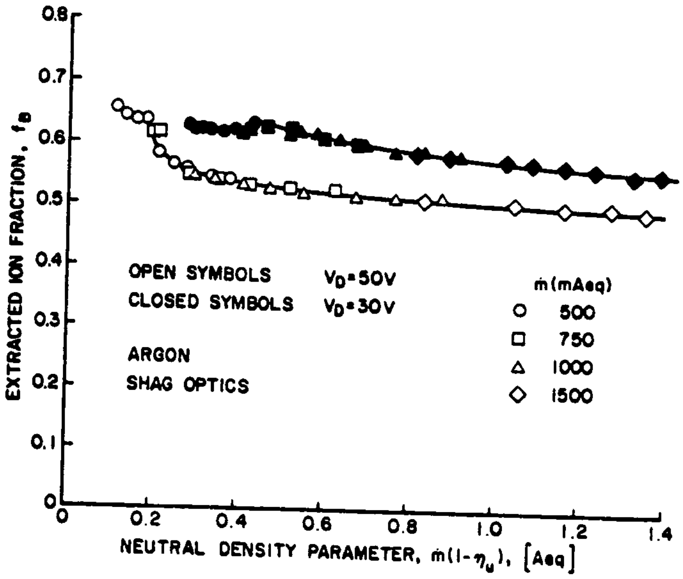

Figure 8a. Effect of Discharge Voltage on the Extracted Ion Fraction - Configuration I

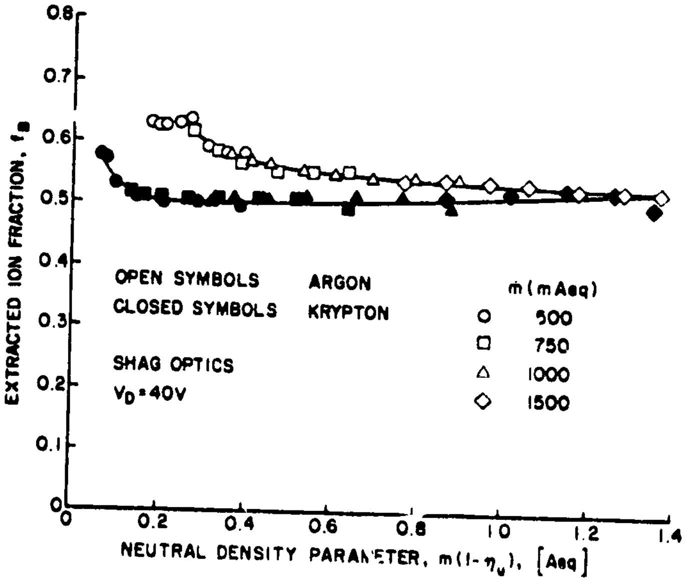

Figure 8b. Effect of Propellant on the Extracted Ion Fraction - Configuration I

The data in Figs. 8a and 8b indicate that the extracted ion fraction is relatively independent of the neutral density parameter. Other data not presented, indicate that the extracted ion fraction sometimes decreases with increasing beam currents for certain thruster configurations. This decrease in f_B results from a decrease in the effective transparency of the screen grid to ions as the plasma density is increased. However, the fraction of the total ion current produced that is directed toward the grids remains constant.

Earlier studies [32,33] indicate that the extracted ion fraction, or the fraction of ions directed toward the grids, is strongly dependent on the magnetic field configuration and thruster geometry. The data in this report indicate that f_B is also a weak function of the discharge voltage and propellant gas, but not a function of the neutral density parameter. Consequently, a simple design approach would be to take f_B to be a constant for a given discharge chamber design (magnetic field configuration), propellant and discharge voltage. Unfortunately, a method for calculating the value of the extracted ion fraction from the above design data remains to be developed.

Plasma Properties

Equation 45 provides a simple expression for the primary electron density as a function of the propellant utilization. As mentioned earlier, the combination of parameters inside the square brackets in this equation may be taken to be roughly a constant for a given propellant, discharge voltage and thruster configuration. The value of this constant, appropriate for argon propellant, a discharge voltage of 50 v and the thruster configuration of Fig. 3b, was calculated to be

1.0×10^{10} cm^{-3} . Thus, Eq. 45 becomes, in this case,

$$n_p = (1.0 \times 10^{10}) \frac{\eta_u}{1-\eta_u} \ (\text{cm}^{-3}) \quad . \tag{70}$$

The value of ε_p^* , required for this calculation, was taken to be the measured value given in Fig. 6a. The value of ε_p^* could, however, have been calculated using the method described in Appendix A.

The volume of the ion production region ($\forall$), required by Eq. 45, was determined from a computer drawn magnetic field map of the discharge chamber. This map was created by measuring the magnetic flux density and direction at regularly spaced points in the discharge chamber. The ion production volume, defined by this map, was taken to be the volume in which the magnetic flux density was 0.005 Tesla or less.

The extracted ion fraction (f_B) was taken to be its measured value obtained in tests with argon propellant, a discharge voltage of 50 v and the thruster configuration of Fig. 3b. The transparency of the grids to neutral atoms (ϕ_o) was calculated from Eq. 66. Finally, the neutral atom velocity (v_o) was calculated based on an assumed effective wall temperature of 400 K.

Comparison of the calculated values of the primary electron density from Eq. 45 (in the form of Eq. 70) with the measured values is given in Fig. 9a. The measured primary electron densities were obtained using the Langmuir probe positioned along the centerline of the discharge chamber. Equations 45 and 70, however, calculate essentially an average primary electron desnity. Further, since the centerline primary electron density is expected to be higher than the average value, the

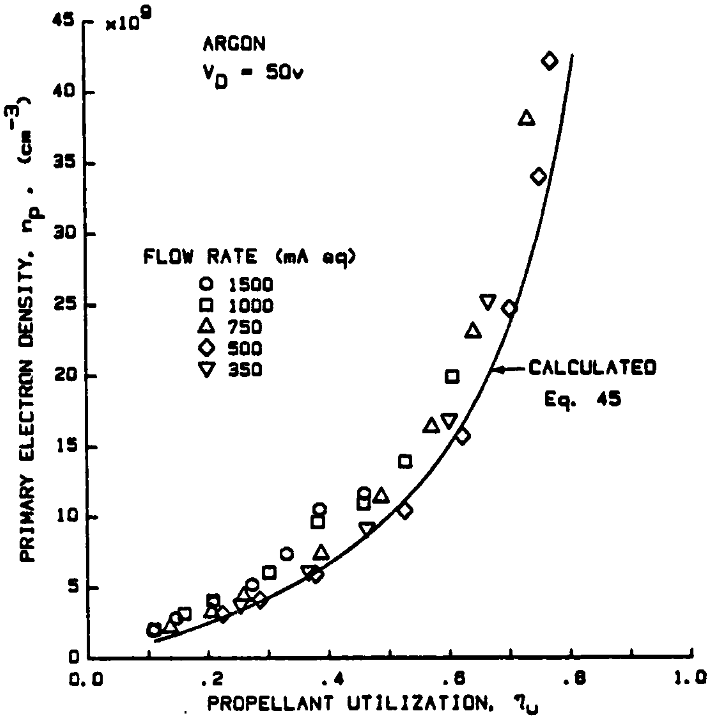

Figure 9a. Primary Electron Density Variation for Argon - Configuration II

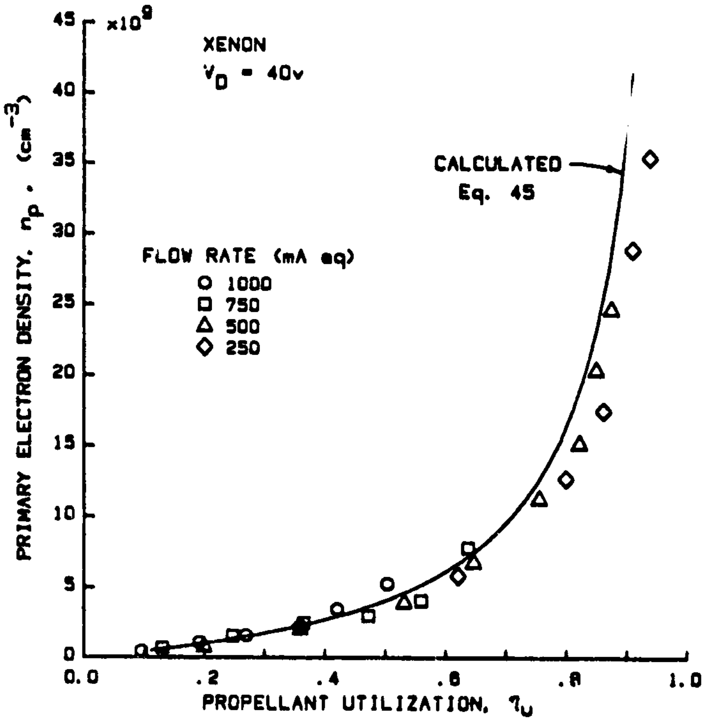

Figure 9b. Primary Electron Density Variation for Xenon - Configuration II

excellent agreement between the calculated and measured values in Fig. 9a is somewhat misleading. This figure clearly indicates, however, that Eq. 45 has the correct functional form and that the primary electron density is indeed relatively independent of the propellant flow rate as predicted by the model.

A similar comparison between calculated and measured primary electron densities is given in Fig. 9b for operation of the same thruster configuration, but with xenon propellant and a discharge voltage of 40 v. Again, the same concludsions drawn from Fig. 9a are also applicable to thruster operation on xenon as indicated in Fig. 9b. The observation that the calculated average values are somewhat greater than the measured centerline values probably results from the use of the measured value of $\varepsilon_p^* = 44$ eV in Eq. 45 rather than the calculated value of $\varepsilon_p^* = 36$ eV given in Appendix A.

An expression for the ratio of primary-to-total electron density is given by Eq. 48. The combination of parameters in the square brackets in this equation is approximately a constant for a given propellant, discharge voltage and thruster configuration. For operation with argon at $V_D = 50$ and the configuration of Fig. 3b, Eq. 48 becomes,

$$\frac{n_p}{n_i} = \frac{0.027}{\dot{m}(1-\eta_u)} \quad . \qquad (71)$$

In making this calculation, the Bohm velocity (v_b) was calculated based on an electron temperature of 4 eV. The value of the screen grid transparency to ions (ϕ_i) was determined experimentally by measuring the ion current to the screen grid and to the beam. The transparency is then the ratio of the beam current to the sum of the screen grid and beam currents. The measured screen grid transparency to ions was approximately 0.8 compared to the physical open area fraction of the screen grid which was approximately 0.68.

Comparison of Eq. 48 (in the form of Eq. 71) with the experimentally measured values is given in Fig. 10a. This figure indicates that for a given discharge voltage, propellant and thruster configuration the primary-to-total electron density ratio is only a function of the neutral density parameter. In addition, it indicates that Eq. 71 has the correct functional form for the variation of this ratio with the neutral density parameter.

For operation of the same thruster configuration with xenon at V_D = 40 v, the results shown in Fig. 10b were obtained. The solid line in this figure corresponds to Eq. 48, where the constant was calculated using values of the parameters in Eq. 48 that are appropriate for xenon propellant and a discharge voltage of 40 v. Figures 10a and b indicate that Eq. 48 correctly accounts for changes in the propellant gas, the discharge voltage, the neutral density parameter and the propellant flow rate.

Comparison of calculated and measured Maxwellian electron temperatures is given in Fig. 11. The calculated electron temperatures were obtained using Eq. 59. For operation with xenon at V_D = 40 and the thruster configuration of Fig. 3b, Eq. 59 becomes,

$$Q_0^+ = \frac{7.64 \times 10^{-14}}{226\, \dot{m}(1-\eta_u)-1} \quad (m^3/s) \quad , \qquad (72)$$

where the appropriate cross section data were obtained from References 49 and 50. Equation 72 gives the value of the Maxwellian ionization rate factor for the production of single ions from neutral atoms as a

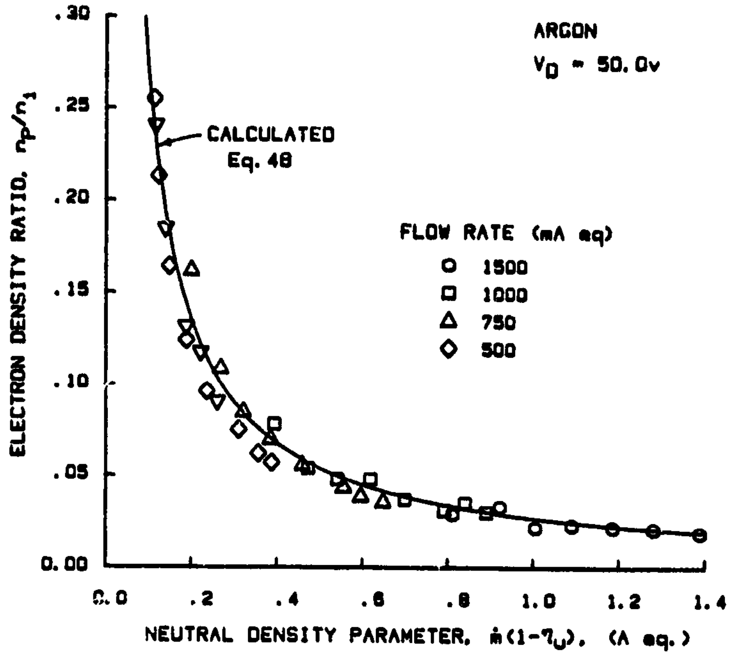

Figure 10a. Primary-to-Total Electron Density Ratio for Argon - Configuration II

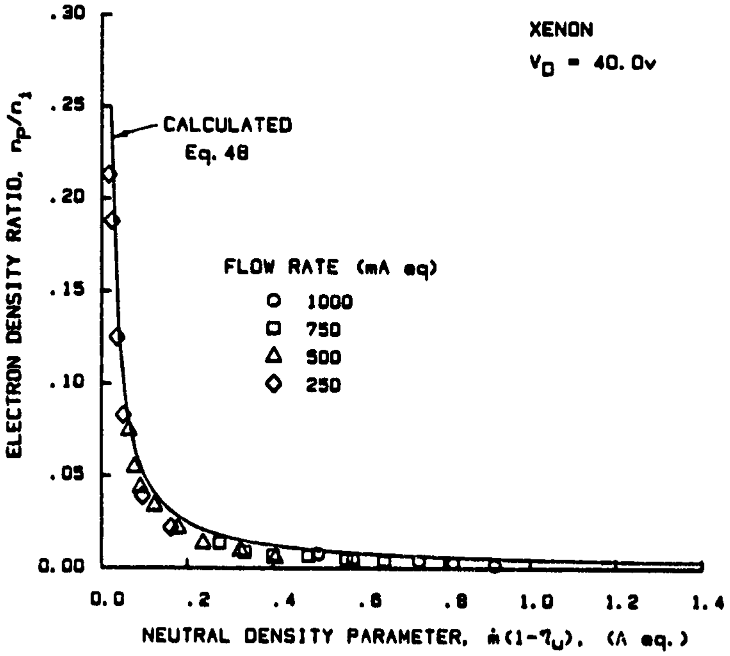

Figure 10b. Primary-to-Total Electron Density Ratio for Xenon - Configuration II

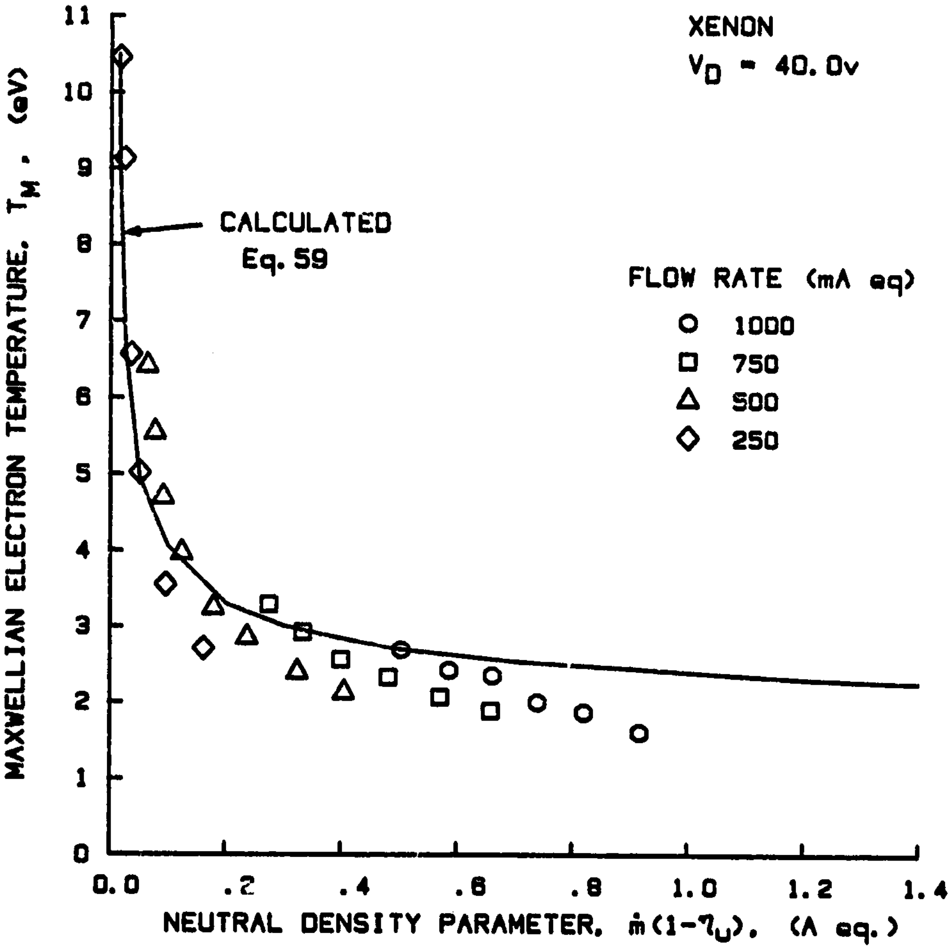

Figure 11. Maxwellian Electron Temperature Variation for Xenon - Configuration II

function of the neutral density parameter. The rate factor Q_o^+ is a function of the Maxwellian electron temperature, and is given by,

$$Q_o^+ = \frac{\sqrt{\frac{2e}{m_e}} \int_0^\infty \sigma_+(E)\, E\, e^{-E/T_M}\, dE}{\int_0^\infty E^{\frac{1}{2}}\, e^{-E/T_M}\, dE} \quad . \qquad (73)$$

Using Eq. 73, the rate factor Q_o^+ may be plotted as a function of the electron temperature as shown in Fig. 12.

To determine the electron temperature as a function of the neutral density parameter, the following procedure is used. First, the value of the rate factor Q_o^+ is calculated for a given value of $\dot{m}(1-\eta_u)$ using Eq. 72. This value of Q_o^+ is then used to enter the curve in Fig. 12 from which the corresponding electron temperature is determined. Repeating this procedure generates the curve of Maxwellian electron temperature versus neutral density parameter shown as the solid line in Fig. 11. The agreement between the calculated and measured electron temperatures is considered to be quite good.

In addition to the Langmuir probe positioned on the thruster centerline, a second probe was positioned on the upstream magnet ring. This probe was used to measure the temperature of the Maxwellian electrons and the energy of the primary electrons reaching the anode. Because the probe was positioned in a region of very high magnetic flux density, the electron temperatures determined from the probe traces obtained with this probe are probably only equal to the electron temperature resulting from motion along the magnetic field lines. The electron temperature corresponding to motion normal to the field lines

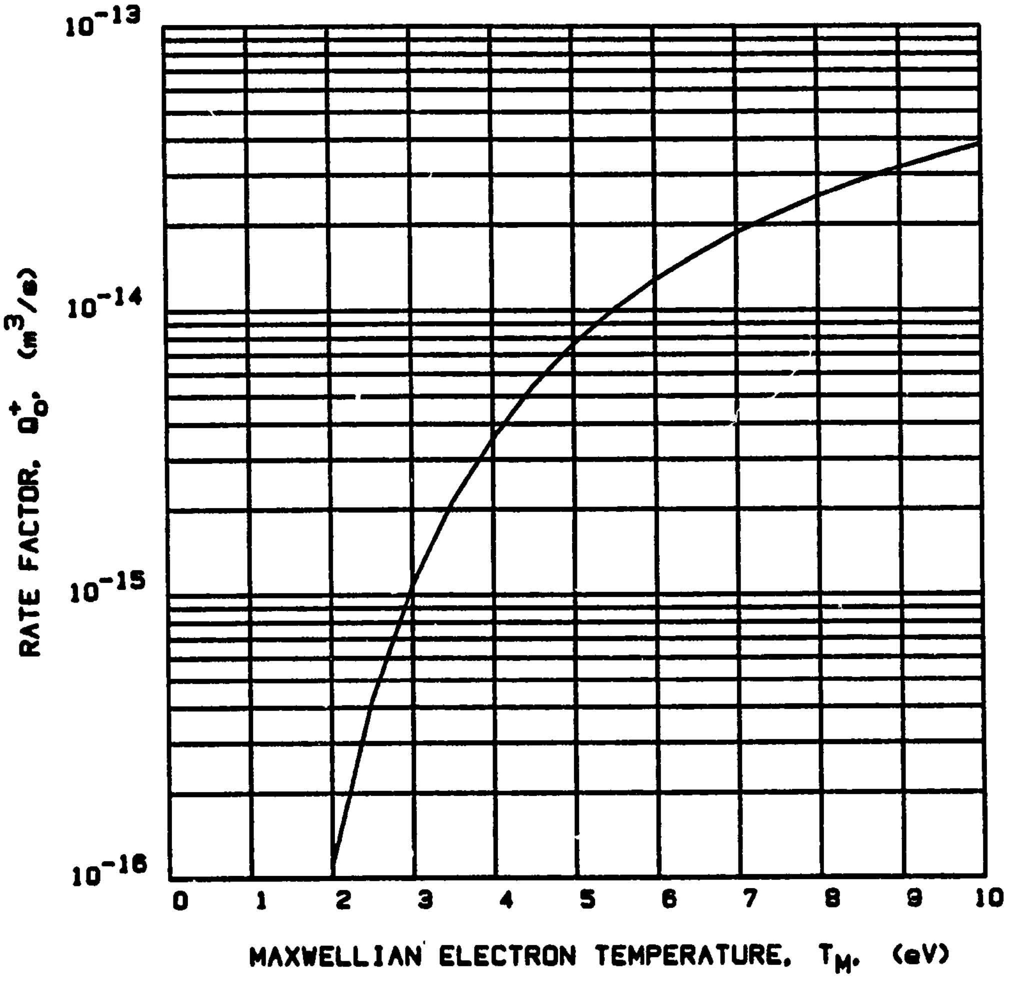

Figure 12. Ionization Rate Factor for Xenon

may or may not be the same. For simplicity, these temperatures are assumed, in this work, to be the same.

The measured electron temperatures at the anode were found to be less than the measured centerline temperatures by approximately a factor of 2/3. The correlation of electron temperature at the anode with the centerline electron temperature is given in Fig. 13. The data in this figure were obtained with the thruster configuration of Fig. 3b using both argon and xenon propellants. The solid line in this figure has a slope of 2/3. This observation that the electron temperature at the anode is approximately 2/3 of the centerline temperature is used in Appendix A for the calculation of ε_p^* .

The probe traces obtained with the probe positioned on the magnet ring surface also indicated the presence of primary electrons. For operation at a discharge voltage of 50 v, these primary electrons had an energy of approximately 50 eV as the model suggests they should for this case where a refractory cathode is used ($V_C = 0$). Similarly, for operation at $V_D = 40$ v, the measured primary electron energy at the anode surface was $\sim$ 40 eV. These probe traces provide direct evidence of the loss of primary electrons through the magnetic field cusp to the anode. Further, the loss rate of these primary electrons was seen to increase as the neutral density parameter decreases as the model predicts.

A comparison between the calculated (from Eq. 66) and measured values of the doubly-to-singly charged ion beam current ratio is given in Fig. 14. The measured values are given by the open symbols and the calculated values by the solid symbols. The propellant utilization efficiencies in this figure have been corrected for the presence of

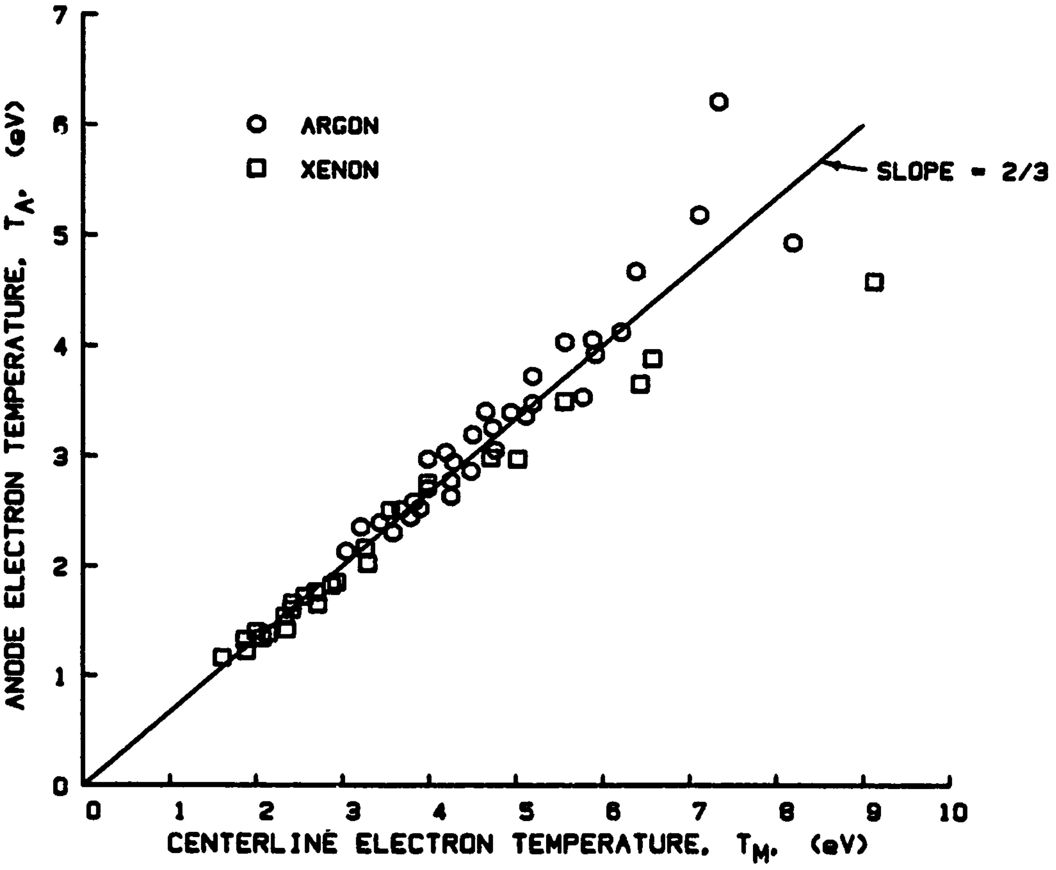

Figure 13. Correlation of Electron Temperatures

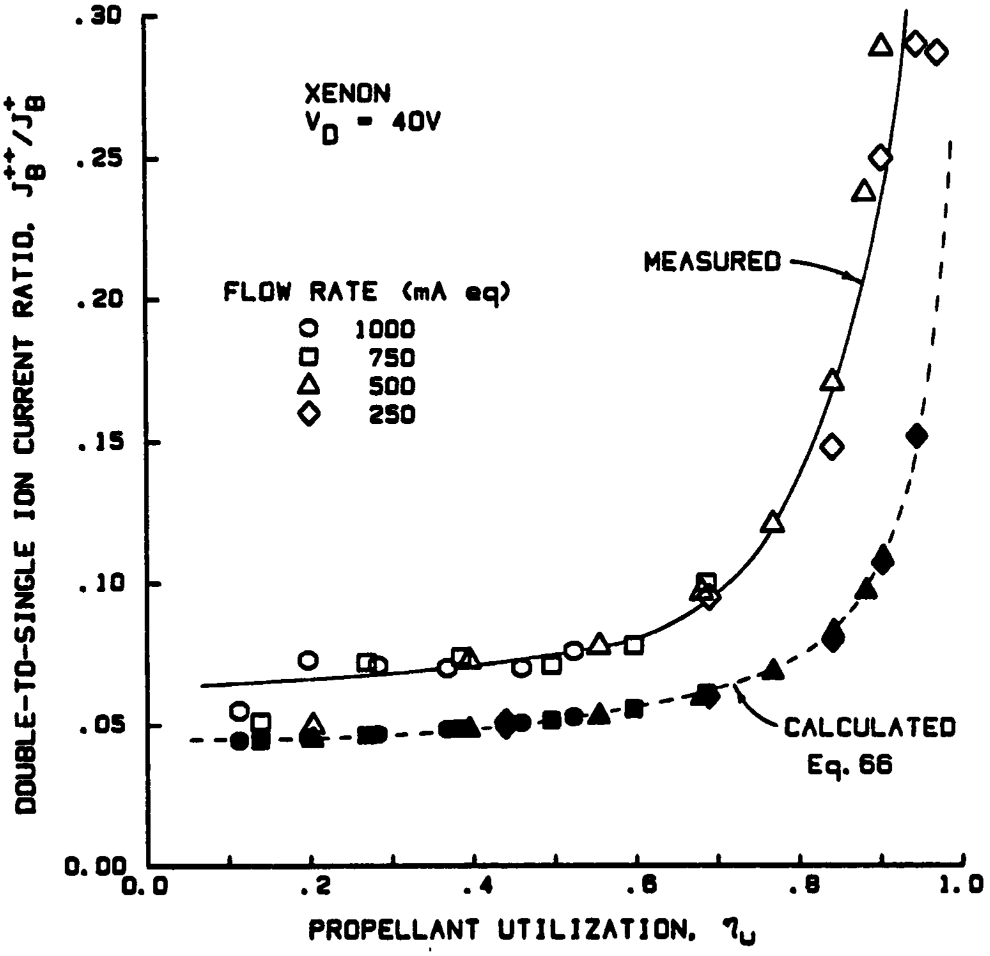

Figure 14. Doubly-to-Singly Charged Ion Beam Current Results

doubly charged ions according to Eq. B-5 given in Appendix B. The ratios J_B^{++} / J_B^{+} in Fig. 14 were taken to be equal to the values of doubly-to-singly charged ion current density measured on the thruster centerline. The values calculated from Eq. 66, however, correspond to values of this ratio averaged over the entire grid area. Since the centerline ratio is expected to be greater than the average value, the data points in Fig. 14 are believed to be shifted up and to the left relative to the locations of the corresponding average values. The amount of this shift is unknown. This shift, however, is believed to account for at least part of the difference between the measured and calculated values.

In calculating the values of J_B^{++}/J_B^{+} using Eq. 66, the collision cross section data required for the calculation of the parameters Q_0^{+} and P_0^{+} were taken from Reference 50. The values of the parameters Q_0^{++}, Q_+^{++}, P_0^{++}, P_+^{++} were obtained from Reference 11, in which the collision cross sections were calculated using the classical cross section model of Gryzinski [51]. The use of Gryzinski cross section data in the calculations of J_B^{++}/J_B^{+} might also account for some of the difference between the measured and calculated values. The values of the Maxwellian electron temperature and primary-to-Maxwellian electron density ratio, required as inputs to Eq. 66, were calculated using Eqs. 48, 49 and 59.

Finally, it is noted that, the values of J_B^{++}/ J_B^{+} calculated from Eq. 66 are very sensitive to the value of the electron temperature used in the calculations. Equation 66 does, however, indicate the correct functional dependence of the doubly-to-singly charged beam current ratio on thruster operating conditions.

V. MODEL APPLICATIONS

Thruster Design

Equation 28 (repeated below) provides a single equation describing the performance curve of a given thruster design

$$\varepsilon_B = \frac{\varepsilon_p^*}{f_B\left[1-e^{-C_o\dot{m}(1-\eta_u)}\right]} + \frac{f_C V_D}{f_B}$$

This equation, along with the data presented in Chapter IV, suggest that the performance of any thruster design depends on the values of four discharge chamber configuration controlled parameters: ε_p^*, C_o, f_B and f_C; and two operating parameters, $\dot{m}$ and V_D. The effect of these parameters on performance was investigated analytically through Eq. 28 by choosing the following set of values as the standard set, then varying them one at a time to determine their effect on the traditional performance curves.

Table 1

Standard Configuration Parameters

$\dot{m}$ = 1000 mA eq.
f_B = 0.6
f_C = 0.1
V_D = 50 v
C_o = 3.0 A eq.
ε_p^* = 50 eV

Figure 15a shows the effect of the extracted ion fraction on performance. As expected, this parameter has a strong effect on the performance. Changes in f_B shift the performance curve up or down, but do not substantially change its shape. Clearly, it is desirable to have f_B be as large (near unity) as possible.

The effect of the primary electron utilization factor (C_0) on performance is given in Fig. 15b. This parameter also has a strong effect on the performance. Indeed, it is this parameter which primarily determine the shape of the performance curve, with larger values of C_0 corresponding to improved performance and curves with more sharply defined "knees." The definition of C_0 given in Eq. 26 suggests a number of ways in which the value of C_0 may be increased. For example, it may be increased by using a propellant gas characterized by a larger inelastic collision cross section σ_0', and a larger atomic mass (resulting in a lower neutral velocity v_0). The parameter C_0 may also increase by decreasing the grid transparency to neutrals, ϕ_0. This must be done, of course, without increasing the accelerator impingement current. For thruster designs with non-uniform beam profiles, Tailoring the accelerator grid hole size to match the radial current density profile might be a useful way to minimize ϕ_0. Also, three grid systems might be expected to have smaller values of ϕ_0 than two grid systems.

Most importantly, C_0 may be increased by increasing the primary electron containment length (ℓ_e). This length corresponds to the average distance a primary electron would travel in the discharge chamber before being collected by an anode surface provided it had no inelastic collisions. As mentioned earlier, the primary function of the magnetic field in all thruster designs is to increase this length. In

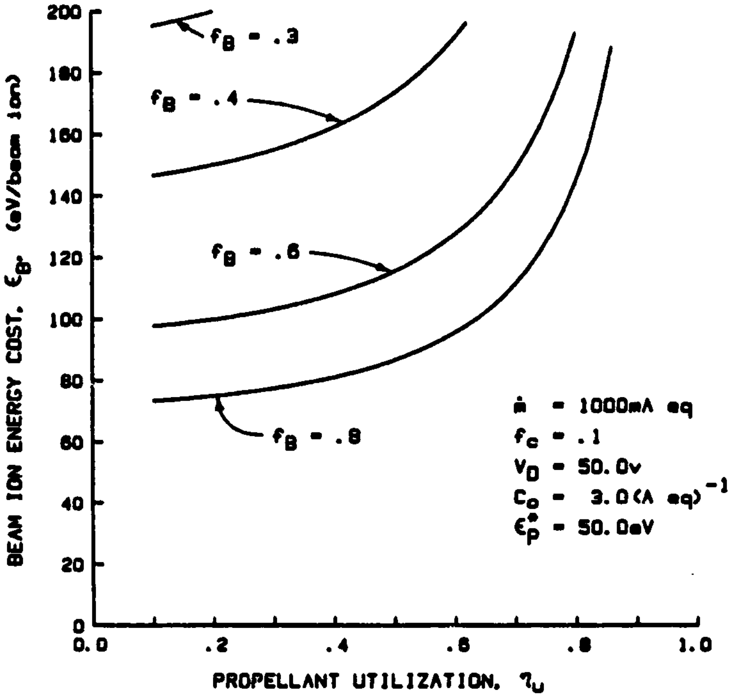

Figure 15a. Effect of f_B on Performance

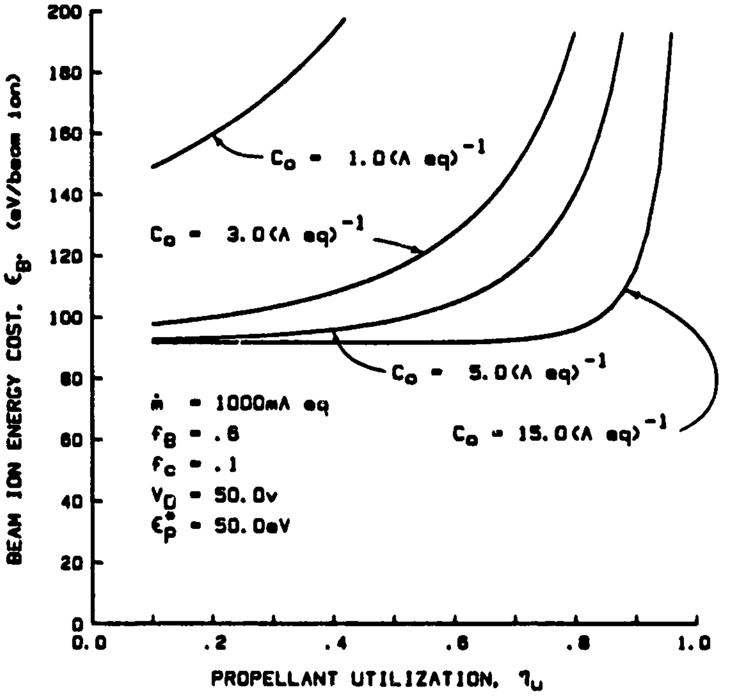

Figure 15b. Effect of C_0 on Performance

cusped field thrusters, primary electrons are lost to the anode through the cusps. Thus, ℓ_e may be increased by decreasing the number of cusps at anode potential or increasing the flux density at the cusp, but only up to a point. Reductions in effective anode cusp area below a certain limit will result in unstable operation of the discharge [22].

Equation 26 also suggests that the primary electron utilization factor may be increased by masking down the area of the grids through which the beam is extracted, A_g. However, decreasing A_g in this manner will lead to a large reduction in the extracted ion fraction, and, therefore, an overall reduction in performance.

The effect of propellant flow rate on performance is shown in Figs. 16a and b. In general, higher flow rates produce better performance. The maximum flow rate at which the thruster can be operated, however, is limited by the ability of the accelerator system to extract the ion current directed toward it. The effect of flow rate on performance is less dramatic for thruster designs characterized by larger values of C_0 as shown in Fig. 16b. High values of C_0 should, therefore, be particularly desirable in thrusters designed to be throttled.

The effect of ε_p^* is merely to shift the performance curves up or down. The amount of the shift increases for smaller values of f_B. For thrusters that use hollow cathodes, the efficiency of the cathode operation (characterized by V_C in Eq. 27) has a strong effect on the value of ε_p^*. In addition, higher values of V_D, in general, produce smaller values of ε_p^*. High discharge voltages, however, are undersirable from thruster lifetime considerations, Consequently, a trade off between thruster performance and thruster lifetime is necessary.

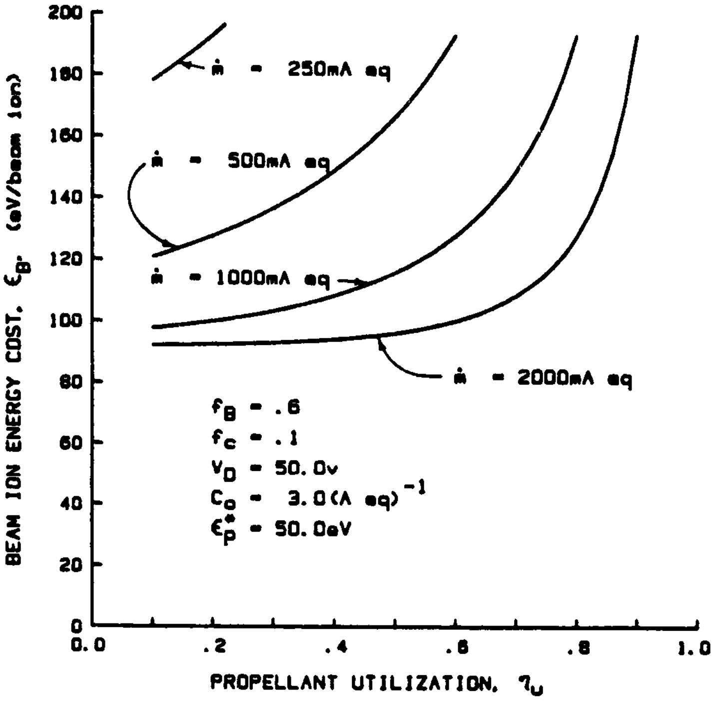

Figure 16a. Effect of Propellant Flow Rate on Performance for Small C_o

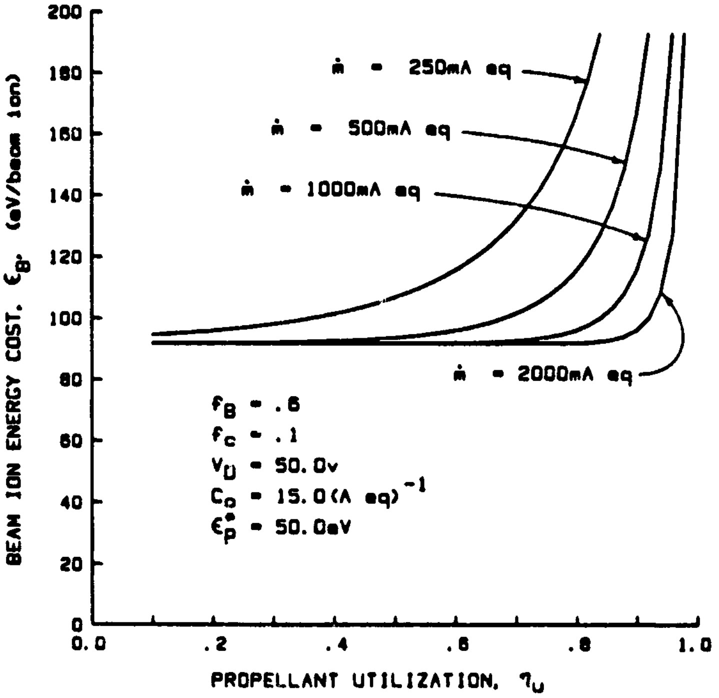

Figure 16b. Effect of Propellant Flow Rate on Performance for Large C_o

The effect of cathode operation on thruster performance can be investigated analytically using the performance model. Hollow cathode operation is reflected in the value of the parameter V_C. The lower the value of this parameter the more efficiently the cathode is operating. At a fixed discharge voltage, increasing the value of V_C degrades the thruster performance in two ways. First, it increases ε_p^* directly through its appearance in Eq. 27, and second, it decreases the energy of the primary electrons, which increases the value of the collisional loss parameter ε_o and decreases the value of C_o. All of these affects are accounted for when ε_p^* is calculated according to the procedure described in Appendix A and the primary electron energy is given by V_D-V_C.

The effect of V_C on the baseline plasma ion energy cost was calculated for xenon propellant using the method described in Appendix A and assuming a discharge voltage of 30 v. The results of these calculations are given in Table 2.

Table 2

Effect of V_C on ε_p^*

V_D (Volts)	V_C (Volts)	V_D-V_C (Volts)	ε_p^* (eV)	C_o (A eq.)$^{-1}$
30	0	30	36	8.0
30	2.5	27.5	42	7.9
30	5.0	25.0	48	7.6
30	7.5	22.5	55	7.2
30	10.0	20.0	66	6.5
30	12.5	17.5	79	5.2

The values of ϵ_p^* and C_0, from Table 2, were then used in the equation for thruster performance (Eq. 28) along with the values: $\dot{m}$ = 1000 mA eq., f_B = 0.5, f_C = 0.1, and V_D = 30 v. The performance curves generated in this manner are shown in Fig. 17. This figure indicates that, at a discharge voltage of 30 v, relatively small changes in V_C can produce substantial changes in thruster performance. For example, increasing V_C from 10 to 12.5 v causes an increase of approximately 30 eV/beam ion in the performance curve.

Work done by Siegfried [52] on inert gas hollow cathodes indicated that a 0.6 v increase in the surface work function of the cathode insert could produce an increase in internal cathode plasma potential from 8 to 12 v. The value of V_C would be expected to increase by this same amount. In addition, Siegfried notes that there is apparently a greater sensitivity of the insert to depletion or contamination of the low work function material for operation with argon or xenon as compared to operation with mercury. Consequently, on the basis of these considerations, one would expect the performance of inert gas ion thrusters operating at low discharge voltages to be quite sensitive to the condition and operation of the hollow cathode.

Changes in the fraction of ion current going to cathode potential surfaces (f_C) also tend to shift the performance curves up or down. Recent trends [23,24] in thruster design to operate the discharge chamber body at anode rather than cathode potential serve to reduce the value of f_C, and consequently improve the performance. In addition, elimination of the separate cathode discharge region in these designs serves to decrease both f_C and V_C, which again improves the performance. It should be noted, however, that an increase in the extracted ion

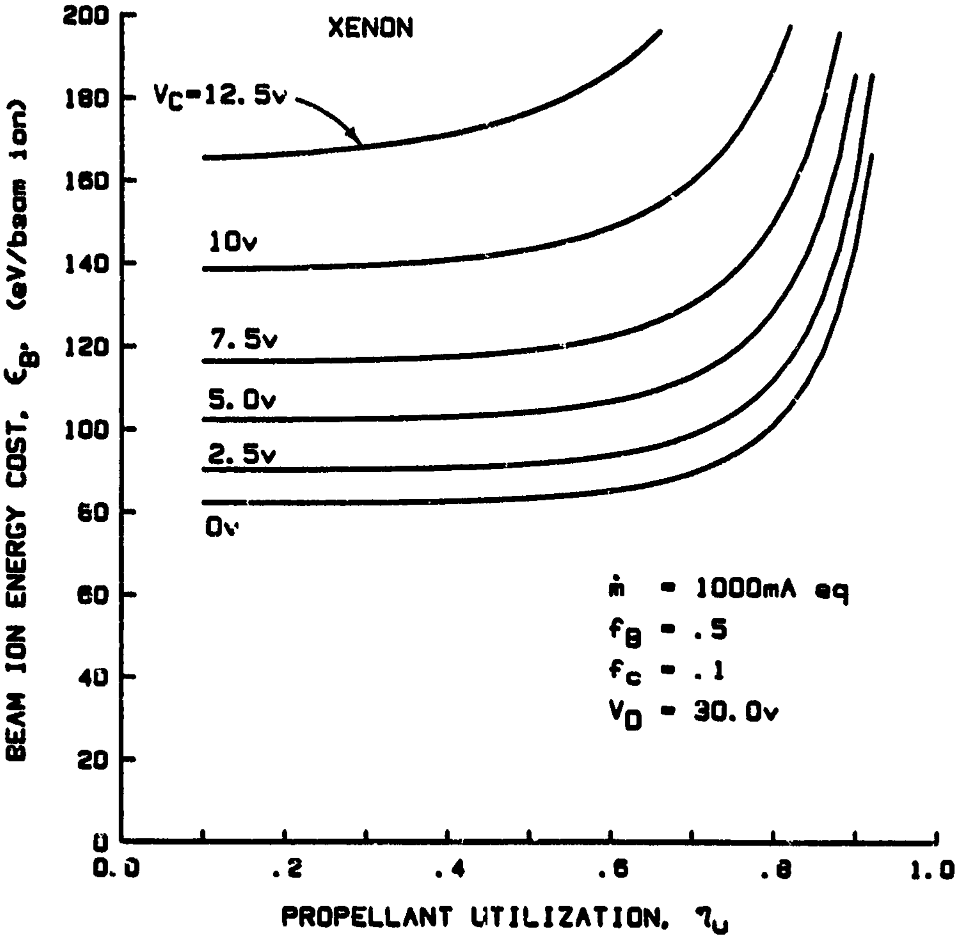

Figure 17. Effect of Cathode Operation on Performance for Xenon

fraction f_B is also believed to be an important factor in the performance improvement observed in these new thruster designs.

Thruster Scaling

The discharge chamber model also suggests performance changes that might be expected from the scaling of thruster designs to different discharge chamber diameters. This may be seen by examining the product of the primary electron utilization factor and propellant flow rate. This product is a dimensionless quantity and is given the symbol B_o.

$$B_o \equiv C_o\dot{m} = \frac{4\sigma_o' \ell_e \dot{m}}{e v_o \phi_o A_g} \quad . \tag{74}$$

For constant, average beam current densities, thruster scaling should be accomplished such that the ratio of mass flow rate to active grid area, $\dot{m}/A_g$, is constant. Thus, for the same propellant and grid transparency to neutrals, Eq. 74 suggests that the discharge chamber performance depends only on the primary electron containment length, ℓ_e. It is believed that this length should increase in approximately direct proportion to thruster diameter, and this suggests that larger diameter thrusters should be more efficient than smaller ones. This is not the whole story, however. The effect of thruster diameter on the extracted ion fraction must also be considered. The above conclusion remains true for thruster scaling accomplished in such a way that f_B remains constant.

Neutral Loss Rate

Rewriting Eq. 22 yields an expression for the neutral atom loss rate from the discharge chamber through the grids,

$$\dot{n}_o = \dot{m} - J_B = \dot{m}(1-\eta_u) \quad . \tag{75}$$

Substituting this into Eq. 28, and solving for the neutral loss rate yields,

$$\dot{n}_o = -\frac{1}{C_o} \ln\left[1 - \frac{\varepsilon_p^*}{f_B\varepsilon_B - f_C V_D}\right] \quad . \tag{76}$$

This equation gives the value of the neutral atom loss rate as a function of the beam ion energy cost. For a specified thruster geometry and discharge voltage, the design parameters C_o, ε_p^*, f_B, f_C and V_D may be taken to be approximately constant. Thus, since the propellant mass flow rate doesn't appear on the right-hand-side of Eq. 76, this equation predicts that the neutral loss rate $\dot{n}_o$ is independent of the flow rate at a constant value of the energy cost per beam ion (ε_B). This same conclusion was reached originally by Kaufman [53] in his constant neutral loss rate theory developed for low magnetic field strength discharge chamber designs.

Thruster Testing without Beam Extraction

It is often desirable to compare the performance of different discharge chamber designs that have been operated without ion beam extraction. Operation without beam extraction is often more convenient and generally requires the use of smaller vacuum test facilities than operation with beam extraction. However, data obtained under these conditions must be interpreted carefully. It has been observed that the performance (eV/beam ion) extrapolated from thruster operation without beam extraction is generally significantly better than the performance measured with beam extraction [24,54,55]. This difference in performance may be understood in context of the performance model developed in this report.

Thruster operation without beam extraction should be characterized by higher discharge chamber neutral densities than operation at the same propellant flow rate with beam extraction. This is because, without beam extraction most of the propellant leaves the discharge chamber in the form of neutral atoms at the neutral atom thermal velocity. With beam extraction, however, most of the propellant leaves in the form of ions at the Bohm velocity. Therefore, since the total propellant flow rate leaving the thruster must be the same in each case, the loss rate of neutrals is smaller with beam extraction than without it, implying lower neutral densities. This is primarily a consequence of the changing effective transparency of the screen grid. Without beam extraction, the effective screen grid transparency is very small [56] since ions tend to be focused onto the grid webbing. With beam extraction, the ions tend to be focused away from the screen grid webbing and through the grid apertures. In any case, operation at higher neutral densities, for the same thruster configuration, translates into lower plasma ion energy costs according to Eq. 25.

The performance model developed herein may be used to make more meaningful extrapolation of data taken without beam extraction to operation with beam extraction. To do this, it is necessary to experimentally determine the values of the parameters ε_p^*, C_o, f_B and f_C. The parameters ε_p^* and C_o are roughly independent of the neutral density, thus, shouldn't change depending on whether or not a beam is extracted. For hollow cathode equipped thruster designs, however, the baseline plasma ion energy cost includes the parameter V_C, which is an indication of cathode performance. The value of V_C may be a function of the discharge chamber neutral density and consequently could cause the value of ε_p^* to change for operation with and without beam extraction. The magnitude of the change in V_C, if any, is unknown.

To determine the values of ε_p^* and C_o for operation without beam extraction, some method of estimating the total ion current produced as a function of the discharge chamber neutral density must be used. This is probably most easily accomplished using several ion current probes positioned at the walls of the discharge chamber in the manner suggested by Poeschel [54]. Ideally, these data should be acquired over a range of neutral densities at a constant discharge voltage.

Once the total ion current produced is known as a function of the neutral density, a curve similar to Fig. 4a may be generated, where the values of ε_p are calculated using Eq. 2. From these data, the values of ε_p^* and C_o may then be determined as those which give the best fit of Eq. 25 to the data. Note, ε_p^* may also be calculated according to the procedure outlined in Appendix A.

Finally, the values of f_B and f_C may be determined using the above probe data and guessing a value of the effective screen grid transparency appropriate for the beam extraction condition. Once the values of ε_p^*, C_o, f_B and f_C have been determined, the performance curve for the beam extraction condition may be approximated using Eq. 28, for any desired total propellant flow rate.

Space Propulsion Mission Analysis

The performance model, developed in this report, is particularly useful for examining the impact of thruster performance on space propulsion missions. It should also be useful for studies making comparisions of the capabilities of different propulsion systems such as those done in References 57 and 58. The following analysis is intended as an illustration of the kinds of things that can be done using this thruster performance model. Consequently, the orbit transfer mission considered here has been greatly simplified. Solving a more accurate and complicated orbit transfer problem would not provide any additional insight into the applicability of the model to mission analysis, and may even tend to conceal the desired illustration. In the analysis that follows, the effect of thruster performance on the maximum payload fraction obtainable for a low earth orbit to geosynchronous earth orbit transfer mission, with a characteristic velocity of 6000m/s, is investigated.

The rocket equation (Eq. 77) gives the ratio of final spacecraft mass (M_f) to initial mass (M_i) as a function of the characteristic velocity for the mission (ΔV), the thruster exhaust velocity (u) and the thruster propellant utilization efficiency (η_u),

$$\frac{M_f}{M_i} = e^{-\Delta V/\eta_u u} \quad . \tag{77}$$

Assuming, for simplicity, that the final mass consists only of the payload mass (M_ℓ) and the mass of the power plant (M_g) then Eq. 77 can be written as,

$$\frac{M_\ell}{M_i} = e^{-\Delta V/\eta_u u} - \frac{M_g}{M_i} \quad . \tag{78}$$

The mass of the power plant is proportional to the power generated,

$$M_g = \alpha P_g \quad , \tag{79}$$

where α is the specific power plant mass (Kg/W), and P_g is the generator power (W). The generator power may be given as,

$$P_g \eta_t = \frac{1}{2} \dot{m}_p u^2 \eta_u \quad , \tag{80}$$

where η_t is the thruster electrical efficiency and $\dot{m}_p$ is the total propulsion system propellant mass flow rate (kg/s). For a constant exhaust velocity and propellant efficiency, Eq. 80 may be integrated to obtain,

$$P_g = \frac{M_{p_o} u^2 \eta_u}{2\eta_t t} \quad , \tag{81}$$

where M_{p_o} is the initial propellant mass and t is the total mission time. Combining Eqs. 78-80 and recognizing that,

$$\frac{M_{p_o}}{M_i} = 1 - e^{-\Delta V/\eta_u u} \quad , \tag{82}$$

yields,

$$\frac{M_\ell}{M_i} = e^{-\Delta V/\eta_u u} - \frac{\alpha u^2 \eta_u}{2\eta_t t} \left(1 - e^{-\Delta V/\eta_u u}\right) \quad . \tag{83}$$

Considering only discharge chamber losses, the thruster electrical efficiency may be approximated by,

$$\eta_t = \frac{1}{1+\varepsilon_B/V_N} \quad , \tag{84}$$

where V_N is the net accelerating voltage. The net accelerating voltage is related to the exhaust velocity by,

$$e\,V_N = \frac{1}{2}\, m_i u^2 \quad . \qquad (85)$$

Combining Eqs. 83-85 yields,

$$\frac{M_\ell}{M_i} = e^{-\Delta V/\eta_u u} - \frac{\alpha u^2 \eta_u}{2t}\left(1 + \frac{2e\varepsilon_B}{m_i u^2}\right)\left(1 - e^{-\Delta V/\eta_u u}\right) \quad . \qquad (86)$$

Equation 86 gives the payload mass fraction as a function of: the characteristic velocity, the exhaust velocity, the mission time, the power plant specific mass, the charge-to-mass ratio of the beam ions, the average beam ion energy cost and the propellant utilization efficiency. The average beam ion energy cost is related to the propellant utilization efficiency through the equation developed in the thruster performance model,

$$\varepsilon_B = \frac{\varepsilon_p^*}{f_B\left[1 - e^{-B_o(1-\eta_u)}\right]} + \frac{f_C V_D}{f_B} \quad , \qquad (87)$$

where B_o is a dimensionless quantity describing the utilization of primary electrons in the discharge chamber and is given by Eq. 74.

For a given characteristic velocity, mission time, power plant specific mass, and propellant utilization efficiency, the optimum exhaust velocity corresponding to the maximum payload fraction, for these conditions, can be determined from Eq. 86. This is accomplished by setting the derivative of Eq. 86 (with respect to u) equal to zero and numerically solving the resulting equation for u. Substituting this value of the exhaust velocity back into Eq. 86 gives the value of the optimum payload fraction under the specified conditions. This procedure may be repeated for different values of propellant utilization, where, for each value of η_u, the corresponding beam ion energy cost is calculated from Eq. 87. In this manner, a curve of optimized payload fraction versus propellant utilization efficiency may be generated for specified values of the characteristic velocity, mission time, power plant specific mass and thruster performance parameters, ϵ_p^*, f_B, f_C, B_o and V_D.

An example of this is shown as the solid line in Fig. 18 for a characteristic velocity of 6000 m/s, a mission time of 200 days and a specific power plant mass of 40 kg/kW. In addition, the thruster performance parameters were taken to be $\epsilon_p^* = 50$ eV, $f_B = 0.5$, $f_C = 0.1$, $B_o = 5$ and $V_D = 40$ v with argon as the propellant. Figure 18 indicates that the curve of optimized payload fraction versus propellant utilization efficiency goes through a maximum. The propellant utilization efficiency corresponding to this doubly maximized payload fraction indicates the location on the thruster performance curve at which the thruster should be operated in order to truly maximize the payload fraction. In summary, the doubly maximized payload fraction was determined by optimizing the exhaust velocity to produce the optimum payload fraction for a given propellant utilization efficiency and subsequently selecting the propellant utilization to obtain the maximum payload fraction from this set of optimized payload fractions.

To illustrate more clearly what is going on, the initial propellant mass fraction (M_{p_o}/M_i) and power plant mass fraction (M_g/M_i) are plotted along with the optimized payload fraction in Fig. 18. Note that the sum of the three curves in this figure, at any propellant utilization, is equal to unity. As the propellant utilization increases the initial propellant mass fraction decreases as expected. In addition, the power

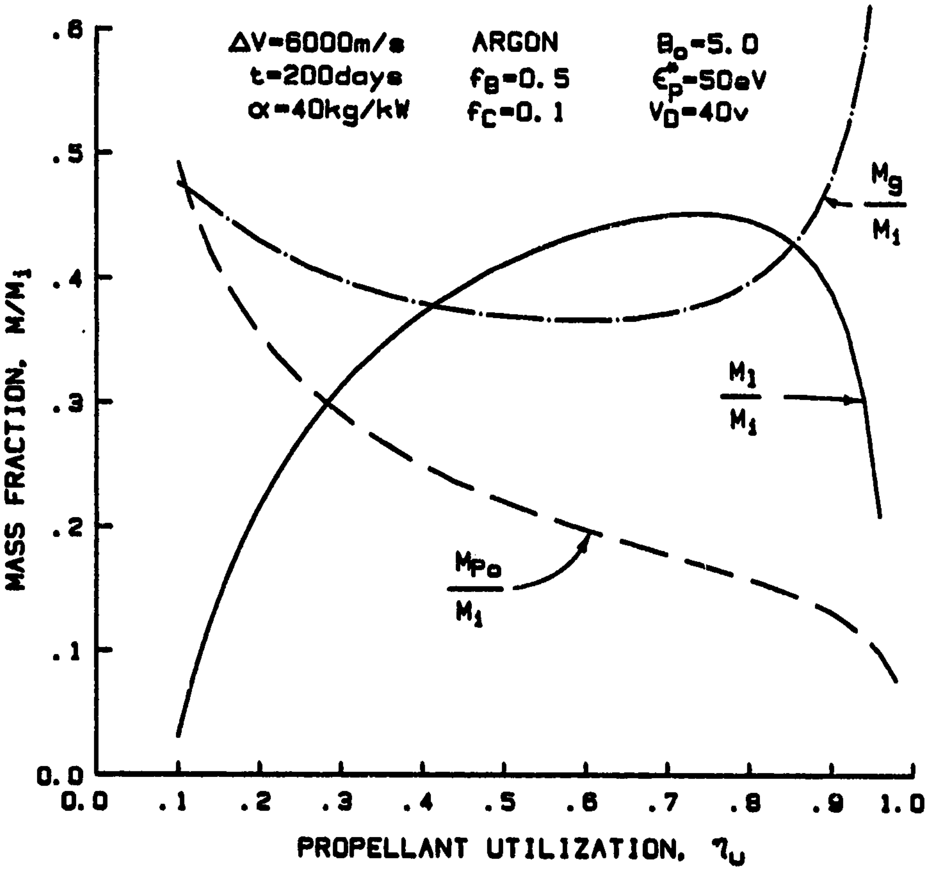

Figure 18. Payload Fraction, Propellant Mass Fraction, and Generator Mass Fraction Variation with Propellant Utilization

plant mass decreases initially, due to a decreasing optimum exhaust velocity, then increases dramatically at high propellant utilization efficiencies, due to the rapid increase in the average beam ion energy cost. For the set of conditions chosen for the curves in Fig. 18, the doubly maximized payload fraction occurs at a propellant utilization of 0.73.

The effect of the specific power plant mass on the optimized payload fraction vs. propellant utilization efficiency curve is shown in Fig. 19a. It is interesting to note that, at very low values of α the optimized payload fraction is relatively insensitive to large changes in the propellant utilization. In addition, the propellant utilization at which the doubly maximized payload fraction occurs is a function of α. That is, the point at which one should operate on the performance curve of a given thruster depends on the specific power plant mass for the spacecraft. This is illustrated in Fig. 19b, where the optimum propellant utilization efficiences for the specified mission parameters are indicated on the performance curve used in generating the curves in Fig. 19a. It is also interesting to note that, the optimum propellant utilization for the α = 1 kg/kW case occurs well past what might ordinarily be considered the "knee" of the performance curve. In a similar manner, the mission time can be shown to effect the optimum propellant utilization, with longer trip times yielding higher optimum propellant utilizations.

So far, only one thruster performance curve has been considered and it has been observed that the optimum propellant utilization efficiency corresponding to the doubly maximized payload fraction is a function of the specific power plant mass and the mission time. The effect of the

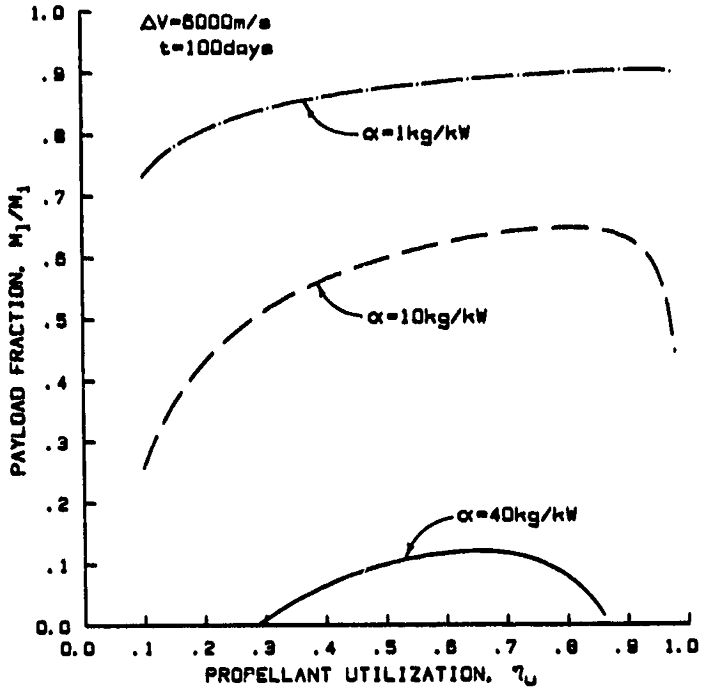

Figure 19a. Effect of Power Plant Specific Mass on Payload Fraction

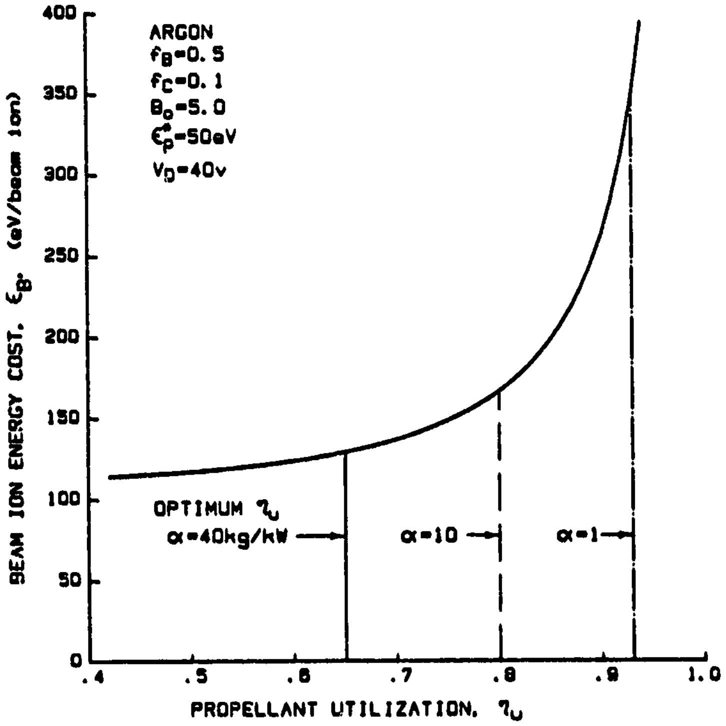

Figure 19b. Effect of Power Plant Specific Mass on Optimum Propellant Utilization

thruster performance parameters on the optimum payload vs. propellant utilization curves will now be investigated.

Figure 20a indicates the effect of the parameter B_o on payload fraction curves. This parameter primarily determines the shape of the thruster performance curve. As expected, larger values of B_o yield higher maximum payload fractions. The optimum propellant utilization efficiencies are indicated, for each performance curve in Fig. 20 b, by the vertical lines that intersect the curves.

The effect of the extracted ion fraction on the payload fraction curves is shown in Fig. 21a. Not surprisingly, higher extracted ion fractions produce larger maximum payload fractions. Again, the optimum propellant utilizations are indicated for each performance curve in Fig. 21b.

Finally, the effect of the propellant gas is indicated in Fig. 22a. To generate the curve labelled "argon" in this figure, the following thruster performance parameters were used: $f_B = 0.5$, $f_C = 0.1$, $V_D = 40$ v, $B_o = 5.0$ and $\varepsilon_p^* = 50$ eV. For krypton and xenon propellants, the values of f_B and f_C were held constant, but, the values of V_D. B_o and ε_p^* were changed to 30 v, 8.2 and 49 eV for krypton, and 30 v, 14.6 and 42 eV for xenon. The changes in the values of B_o were calculated using the equations developed in the thruster performance model. The changes in the values of ε_p^* are consistent with measured changes in this parameter for a given thruster design operated on the three propellant gases. Clearly, xenon propellant is superior to either argon or krypton propellants. The performance curves, along with the corresponding optimum propellant efficiencies, are given in Fig. 22b for the cases where these three propellants are used.

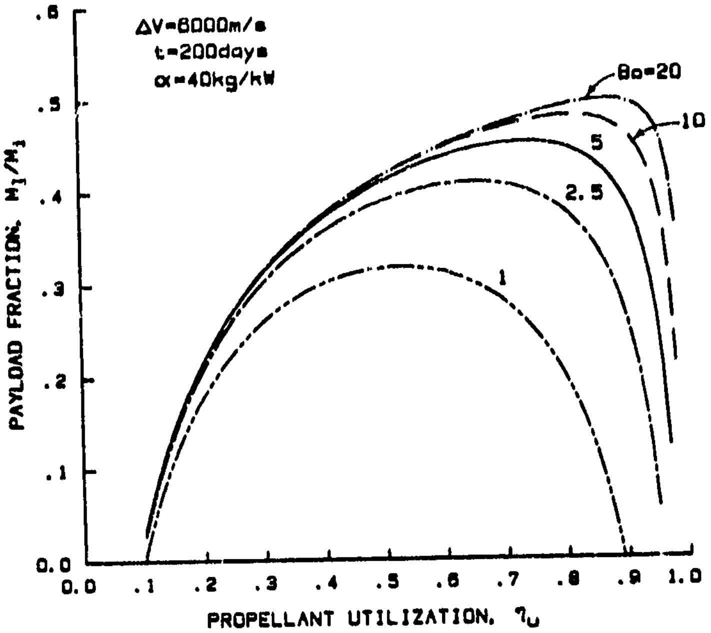

Figure 20a. Effect of B_0 on Payload Fraction

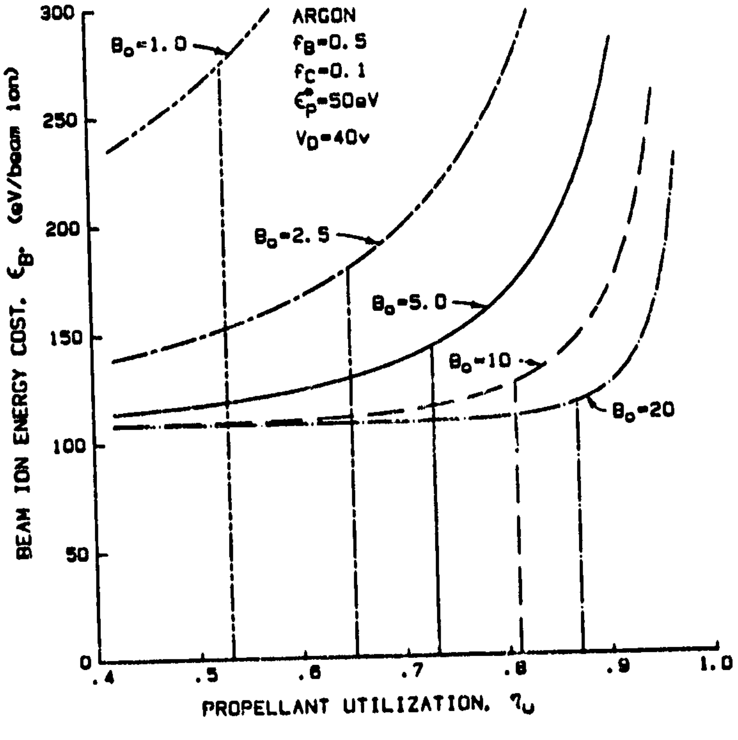

Figure 20b. Effect of B_0 on the Performance Curve and the Optimum Propellant Utilization

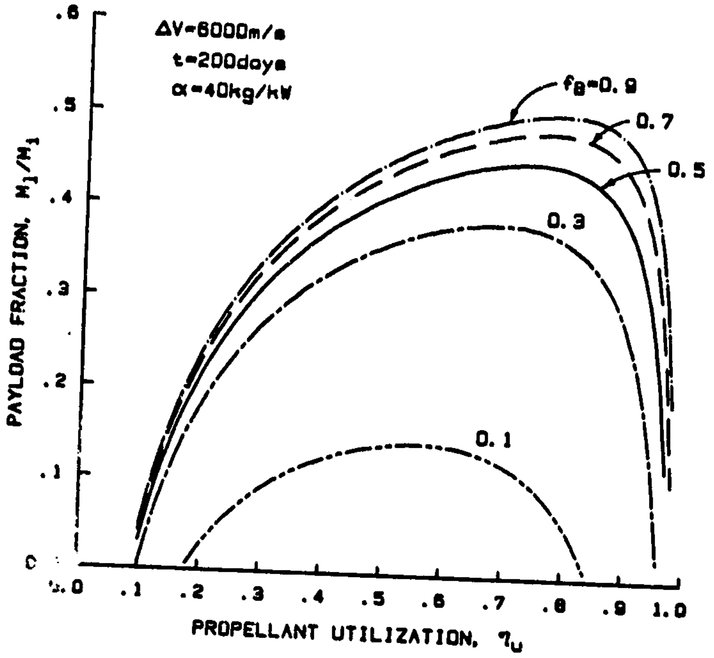

Figure 21a. Effect of f_B on Payload Fraction

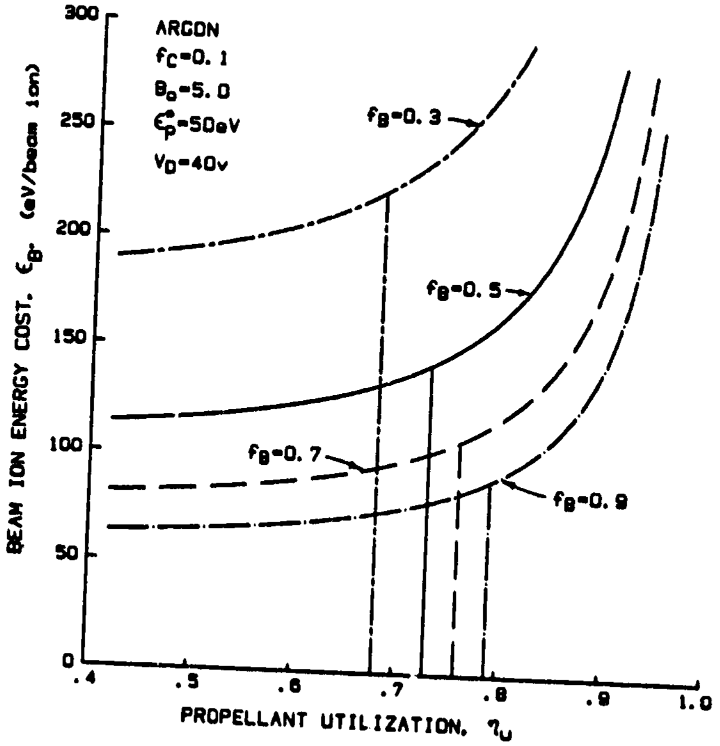

Figure 21b. Effect of f_B on the Performance Curve and the Optimum Propellant Utilization

C-2

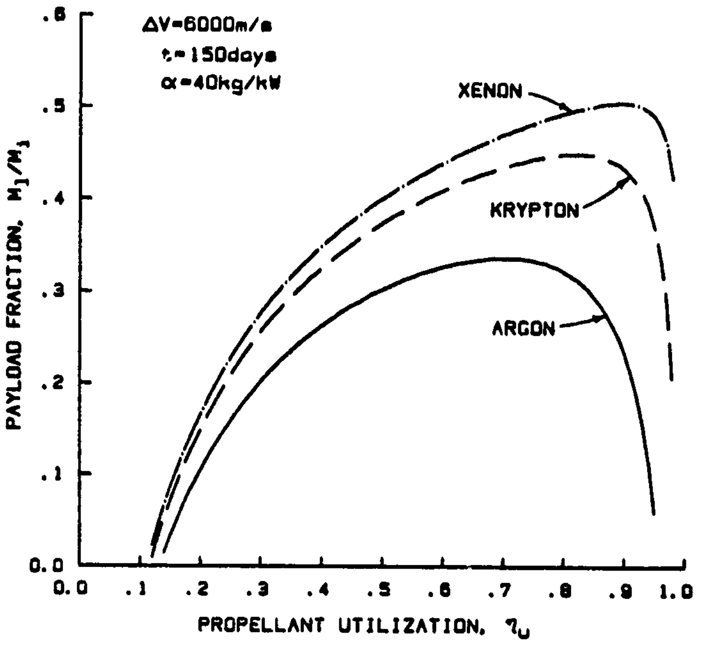

Figure 22a. Effect of Propellant on Payload Fraction

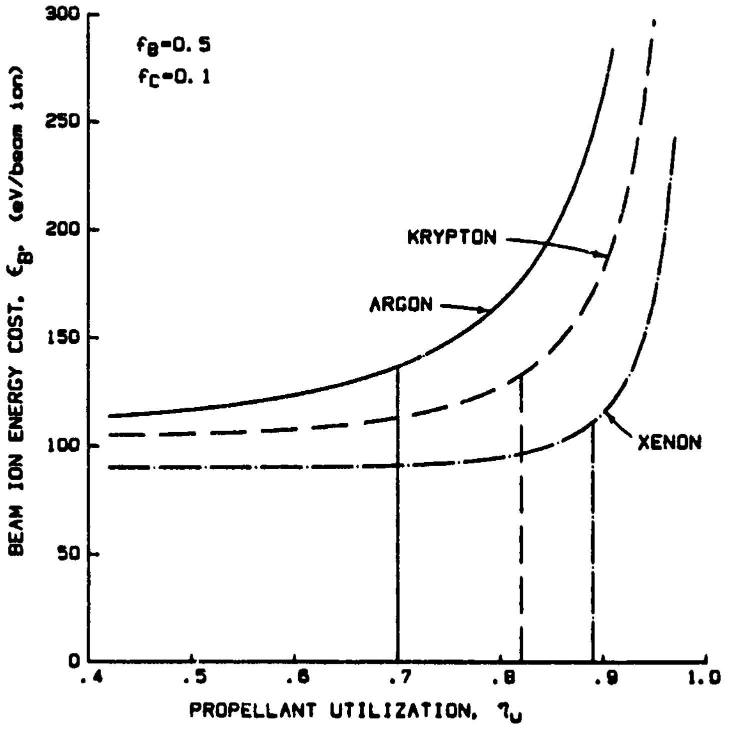

Figure 22b. Effect of Propellant on the Performance Curve and the Optimum Propellant Utilization

VI. CONCLUSIONS

A simple thruster performance model, that has led to an improved understanding of ion thruster discharge chamber operation, has been developed. This model describes ion thruster performance in terms of four parameters: the plasma ion energy cost (ε_p), the extracted ion fraction (f_B), the ion current fraction to cathode potential surfaces (f_C) and the discharge voltage (V_D).

The equation developed to describe the behavior of the plasma ion energy cost agrees with the results of a variety of experiments. This equation provides an expression for the functional dependence of the plasma ion energy cost on the neutral density parameter, $\dot{m}(1-\eta_u)$. Experiments indicate good agreement between the predicted functional form of the model and the experimental data. These experiments also suggest that the primary electron utilization factor (C_0) and the baseline plasma ion energy cost (ε_p^*) are independent of the neutral density parameter under many conditions. The model correctly predicts the variation in plasma ion energy cost for changes in: propellant gas, grid transparency to neutral atoms, beam extraction area, discharge voltage and effective discharge chamber wall temperature. The model is applicable to both ring and line cusp thruster designs.

Measurements of the extracted ion fraction indicate that this parameter is relatively independent of the neutral density parameter. The extracted ion fraction does, however, appear to be a function of the thruster geometry and magnetic field configuration, and to a lesser extent the propellant gas and the discharge voltage. No effective method for calculating the extracted ion fraction based on these considerations is available at the present time.

The values of several discharge chamber plasma properties can be easily calculated, as a function of thruster operating conditions, using the equations developed in the model. These properties include: the primary electron density, the primary-to-total and primary-to-Maxwellian electron density ratios and the Maxwellian electron temperature. The values of these properties, calculated by the model, agree well with the corresponding experimental data. An equation was also developed to calculate the doubly-to-singly charged ion beam current ratio. Experiments indicate only fair agreement between this equation and the measured data. This is believed to be partly the result of the technique used to measure the doubly-to-singly charged ion beam current ratio, and partly the fact that the calculated values of this ratio are very sensitive to the input electron temperature.

For design purposes, thruster performance may be taken to depend on only four physical parameters (the primary electron utilization factor C_0, the baseline plasma ion energy cost ε_p^*, the extracted ion fraction f_B and the cathode potential surface ion fraction f_C) and two operating parameters (the propellant flow rate $\dot{m}$ and the discharge voltage V_D). Improved performance should be characterized by large extracted ion fractions, long primary electron containment lengths (ℓ_e), small effective grid transparencies to neutral atoms (ϕ_0) and operation at high propellant flow rates. The loss of primary electrons to the anode determines the shape of the performance curve to first order. The model suggests that thruster designs characterized by large values of C_0 should allow efficient throttling. In addition, it suggests that hollow cathode efficiency becomes increasingly important to the discharge chamber performance at low discharge voltages.

The thruster performance model can be very useful for mission analysis calculations. The model allows one to easily identify the optimum propellant utilization at which the thruster should be operated for a given mission. In addition, the model makes it easy to determine which changes in thruster design or operating parameters have the greatest effect on the payload fraction and/or mission duration.

Finally, a simple direct method for the calculation of the baseline plasma ion energy cost has been developed. Calculations of ε_p^* agree well with the measured values.

Suggestions for Future Work

Two of the parameters identified in this investigation as having strong effects on thruster performance were the primary electron containment length and the extracted ion fraction. At the present time, however, these parameters cannot be calculated directly given only the discharge chamber/magnetic field design, propellant gas and discharge voltage. Consequently, future work should focus on the development of a method by which the primary electron containment length and the exracted ion fraction can be calculated based only on this information.

The experiments described in this investigation were all performed using a thruster equipped with a filament cathode. The model suggests, however, that the performance of a thruster equipped with a hollow cathode can be strongly influenced by the operation of the hollow cathode. Consequently, there is a need to verify the predictions of the model on a hollow cathode equipped ion thruster.

Finally, it is of interest to test the validity of the model on the older style, low magnetic field strength thruster designs, such as the SERT II [63] or the J-Series [64] thrusters. These thruster designs differ from the cusped magnetic field designs considered in this investigation in that electrons, in the discharge chamber plasma, can only reach the anode surface by crossing magnetic field lines. In the cusped field designs, however, the majority of electrons are believed to reach the anode by going along the field lines. The mechanism for electron loss in the low magnetic field thruster designs is sufficiently different from that in the cusped field designs that experimental verification of the model on these low field strength designs is required.

REFERENCES

1. Kaufman, H. R. and Reader, P. D., "Experimental Performance of Ion Rockets Employing Electron-Bombardment Ion Sources," American Rocket Society Paper 1374-60, 1960.

2. Kaufman, H. R., "An Ion Rocket with an Electron-Bombardment Ion Source," NASA Tech. Note TN D - 585, 1961.

3. Milder, N. L., "A Survey and Evaluation of Research on the Discharge Plasma of a Kaufman Thruster," Journal of Spacecraft and Rockets, Vol. 7, pp. 641-649, 1970.

4. Kaufman, H. R., "Technology of Electron-Bombardment Ion Thrusters," in Advances in Electronics and Electron Physics, Vol. 36, Academic Press, Inc., New York, 1974.

5. Masek, T. D., "Plasma Properties and Performance of Mercury Ion Thrusters," AIAA Journal, Vol. 9, pp. 205-212, 1971.

6. Beattie, J. R., "Numerical Procedure for Analyzing Langmuir Probe Data," AIAA Journal, Vol. 13, No. 7, pp. 950-952, 1975.

7. Robinson, R. S., "Physical Processes in Directed Ion Beam Sputtering," NASA CR-159567, 1979.

8. Ward, J. W. and Masek, T. C., "A Discharge Computer Model for an Electron Bombardment Thruster," AIAA Paper No. 76-1009, 1976.

9. Peters, R. R., "Double Ion Production in Mercury Thrusters, NASA CR-135019, 1976.

10. Beattie, J. R. and Wilbur, P. J., "Cusped Magnetic Field Mercury Ion Thruster," Journal of Spacecraft and Rockets, Vol. 14, No. 2, pp. 747-755, 1977.

11. Wilbur, P. J. and Kaufman, H. R., "Double Ion Production in Argon and Xenon Ion Thrusters," Journal of Spacecraft and Rockets, Vol. 16, No. 4, pp. 264-267, 1979.

12. Wilbur, P. J., "A Model for Nitrogen Chemisorption in Ion Thrusters," AIAA Paper No. 79-2062, 1979.

13. Isaacson, G. C. and Kaufman, H. R., "15-cm Multipole Gas Ion Thruster," Journal of Spacecraft and Rockets, Vol. 14, No. 8, pp. 469-473, 1977.

14. Kaufman, H. R. and Robinson, R. S., "Plasma Processes in Inert Gas Thrusters," AIAA Paper No. 79-2055, 1979.

15. Kaufman, H. R. and Robinson, R. S., "Ion Source Design for Industrial Applications," AIAA Journal, Vol. 20, No. 6, pp. 745-760, 1982.

16. Longhurst, G. R. and Wilbur, P. J., "Plasma Property and Performance Prediction for Mercury Ion Thrusters," AIAA Paper No. 79-2054, 1979.

17. Arakawa, Y. and Kawasaki, Y., "Discharge Plasma in a Multiple Ion Thruster," AIAA Paper No. 82-1931, 1982.

18. Arakawa, Y., Hamatani, C. and Kawasaki, Y., "Wall Losses of Charged Particles in a Multiple Discharge Plasma," Int'l Electric Propulsion Conference Paper IEPC 84-69, Tokyo, Japan, 1984.

19. Divergilio, W. F., Goede, H. and Fosnight, V. V., "High Frequency Plasma Generators for Ion Thrusters," NASA CR-167957, Interim Report, Nov. 1981

20. Holmes, A. J. T., "Role of the Anode Area in the Behavior of Magnetic Multipole Discharges," Rev. Sci. Instrum., Vol. 52, No. 12, pp. 1814-1823, 1981

21. Goede, A. P. H. and Green, T. S., "Operational Limits of Multipole Ion Sources," Phys. Fluids, Vol. 25, No. 10, pp. 1797-1810, 1982.

22. Goebel, D. M., "Ion Source Discharge Performance and Stability," Phys. Fluids, Vol. 25, No. 6, pp. 1093-1102, 1982

23. Sovey, J. S., "Performance of a Magnetic Multiple Line-Cusp Argon Ion Thruster," Journal of Spacecraft and Rockets, Vol. 19, No. 3, pp. 257-262, 1982.

24. Sovey, J. S., "Improved Ion Containment Using a Ring-Cusp Ion Thruster," Journal of Spacecraft and Rockets, Vol. 21, No. 5, pp. 488-495, 1984.

25. Siegfried, D. E., "A Phenomenological Model for Orificed Hollow Cathodes," NASA CR-168026, December 1982.

26. Medicus, G., "Diffusion and Elastic Collision losses of the 'Fast Electrons' in Plasmas," Journal of Applied Physics, Vol. 29, No. 6, pp. 903, 1958.

27. Bechtel, R. T., Cisky, G. A. and Byers, D. C., "Performance of a 15-Centimeter Diameter, Hollow Cathode Kaufman Thruster," AIAA paper No. 68-88, 1968.

28. Poeschel, R. L., Ward, J. W. and Knauer, W., "Study and Optimization of 15-cm Kaufman Thruster Discharges," AIAA Paper No. 69-257, 1969.

29. Bechtel, R. T., "Performance and Control of a 30-cm. dia. Low-Impulse, Kaufman Thruster," AIAA Paper 69-238, 1969.

30. Cohn, A. J., "Onset of Anomalus Diffusion in Electron-Bombardment Ion Thrusters," NASA TN D-3731, 1966.

31. Poeschel, R. L. and Vahrankamp, R., "The Radial Magnetic Field Geometry as an Approach to Total Ion Utilization in Kaufman Thrusters," AIAA Paper No. 72-481, 1972.

32. Brophy, J. R. and Wilbur, P. J., "The Flexible Magnetic Field Thruster," Journal of Spacecraft and Rockets, Vol. 20, No. 6, pp. 611-618, 1983.

33. Brophy, J. R. and Wilbur, P. J., "Recent Developments in Ion Sources for Space Propulsion," Proc. Int'l Ion Engineering Congress - ISIAT '83 and IPAT '83, Kyoto, Japan, pp. 411-422, 1983.

34. Brophy, J. R. and Wilbur, P. J., "Simple Performance Model for Ring and Line Cusp Ion Thrusters," Int'l Electric Propulsion Conference Paper IEPC 84-68, Tokyo, Japan, 1984.

35. Brophy, J. R. and Wilbur, P. J., "An Experimental Investigation of Cusped Magnetic Field Discharge Chambers," Int'l Electric Propulsion Conference Paper IEPC 84-70, Tokyo, Japan, L984.

36. Wilbur, P. J. and Brophy, J. R., "The Effect of Discharge Wall Temperature on Ion Thruster Performance," Int'l Electric Propulsion Conference Paper, IEPC 84-67, Tokyo, Japan, 1984.

37. Bohm, D., "Minimum Ionic Kinetic Energy for a Stable Sheath," in Characteristics of Electrical Discharges in Magnetic Fields, A. Guthrie and R. K. Wakerling, eds., McGraw-Hill, Inc., New York. 1949.

38. Dugan, J. V. and Sovie, R. J., "Volume Ion Production Costs in Tenuous Plasmas: A General Atom Theory and Detailed Results for Helium, Argon and Cesium," NASA TN D-40150, 1967.

39. Lee, J. F., Sears, F. W., and Turcotte, D. L., Statistical Thermodynamics, Addison-Wesley, 1973.

40. Knief, R. A., Nuclear Energy Technology, McGraw-Hill, Hemisphere Publishing Co., 1981, pp. 111.

41. Chapman, B., Glow Discharge Processes, John Wiley & Sons, Inc., New York, 1980.

42. Vahrenkamp, R. P., "Measurement of Double Charged Ions in the Beam of a 30-cm Mercury Bombardment Thruster," AIAA Paper 73-1057, 1973.

43. Hershkowitz, N., et.al., "Plasma Leakage through a Low β Line Cusp," Physical Review Letters, Vol. 35, No. 5, 1975, pp. 277-280.

44. Leung, K. N., et.al., "Plasma Confinement by Localized Cusps," The Physics of Fluids, Vol. 19, No. 7, 1976, pp. 1045-1053.

45. Hershkowitz, N., et. al., "Electrostatic Self-Plugging of a Picket Fence Cusped Magnetic Field," The Physics of Fluids, Vol. 21, No. 1, 1979, pp. 122-125.

46. Kozima, H., et.al., "On the Leak Width of Line and Point Cusp Magnetic Fields," Physics Letters, Vol. 86A, No. 6, 7, 1981. pp. 373-375.

47. Clausing, P., "Über Die Stromung Sehr Verdünnter Case Durch Rören Von Beliebiger Länge," Annalen Der Physik, Vol. 12, 1932, pp. 961-989.

48. deHeer, F. J., et.al., "Total Cross Sections of Electron Scattering by Ne, Ar, Kr and Xe," Journal of Physics B: Atomic and Molecular Physics, Vol. 12, No. 6, 1979, pp. 979-1002.

49. Hayashi, M., "Determination of Electron-Xenon Total Excitation Cross Sections, from Threshold to 100 eV, from Experimental Values of Townsend's α," Journal of Physics D: Applied Physics, Vol. 16, pp. 581-589, 1983.

50. Rapp, D. and Englander-Golden, P., "Total Cross Sections for Ionization and Attachment in Gases by Electron Impact. I. Positive Ionization," Journal of Chemical Physics, Vol. 34, No. 5, pp. 1464-1479, 1965.

51. Gryzinski, M., "Classical Theory of Atomic Collisions, I. Theory of Inelastic Collisions," Physical Review, Vol. 138, April 19, 1965, p. A341.

52. Siegfried, D., "Xenon and Argon Hollow Cathode Research," in "Advanced Ion Thruster Research," P. J. Wilbur ed., NASA CR-168340, Jan. 1984.

53. Kaufman, H. R. and Cohen, A. J., "Maximum Propellant Utilization in an Electron Bombardment Thruster," Proceedings of the Symposium on Ion Sources and Formation of Ion Beams, edited by Th.J.M. Sluyters, Brookhaven National Laboratory. 1971, pp. 61-68.

54. Poeschel, R. L., "Development of Advanced Inert-Gas Ion Thrusters," NASA CR-168206, June 1983.

55. Beattie, J. R. and Poeschel, R. L., "Ring-Cusp Ion Thrusters," Int'l Electric Propulsion Conference Paper, IEPC 84-71, Tokyo, Japan, 1984.

56. Wilbur, P. J., "Advanced Space Propulsion Thruster Research," NASA CR-165584, December 1981, pp. 85.

57. Jones, R. M., "Comparison of Potential Electric Propulsion Systems for Orbit Transfer," Journal of Spacecraft and Rockets, Vol. 21, No. 1, pp. 88-95, 1984.

58. Kaufman, H. R. and Robinson, R. S., "Electric Thruster Performance for Orbit Raising and Manuevering," Journal of Spacecraft and Rockets, Vol. 21, No. 2. pp. 180-186, 1984.

59. Parker, J. H., "Electron Ejection by Slow Positive Ions Incident on Flashed and Gas-Covered Metallic Surfaces," Physical Review, Vol. 93, No. 6, 1954, pp. 1148-1156.

60. Samson, J. A. and Haddad, G. N., "Secondary Electron Emission from Metals by Slow Positive Ion Bombardment," International Journal of Mass Spectrometry and Ion Physics, Vol. 15, No. 1, 1974, pp. 113-115.

61. Holman, J. P. and Gajda, W. J., Experimental Methods for Engineers, McGraw-Hill, Inc., New York, 1978.

62. Wilbur, P. J., "An Experimental Investigation of a Hollow Cathode Discharge," NASA CR-120847, December 1971.

63. Kerslake, W R., Goldman, R. G. and Nieberding, W. C., "SERT II: Mission, Thruster Performance, and In-Flight Thrust Measurements," Journal of Spacecraft and Rockets, Vol. 8, 1971, pp. 213-224.

64. Bechtel, R. T., "The 30 cm J Series Mercury Bombardment Thruster," AIAA Paper No. 81-0714, April 21-23, 1981.

APPENDIX A

THEORETICAL CALCULATION OF THE BASELINE PLASMA ION ENERGY COST, ε_p^*

The definition of the baseline plasma ion energy cost (ε_p^*) is given by Eq. 27, and is repeated here for convenience,

$$\varepsilon_p^* \equiv \frac{\varepsilon_o + \varepsilon_M}{1-(V_c+\varepsilon_M)/V_D} \quad . \tag{A-1}$$

The parameter ε_o in Eq. A-1 accounts for the energy that is expended in ionization and excitation reactions and is defined in Eq. 15 as,

$$\varepsilon_o \equiv U_+ + \frac{\sum_j \langle\sigma_j v_e\rangle U_j}{\langle\sigma_+ v_e\rangle} \quad . \tag{A-2}$$

The brackets in this equation represent the enclosed product averaged over the entire electron speed distribution function, i.e.,

$$\langle\sigma_+ v_e\rangle = \frac{\int_0^\infty \sigma_+(v_e) v_e F(v_e) dv_e}{\int_0^\infty F(v_e) dv_e} \quad , \tag{A-3}$$

where $F(v_e)$ represents the entire electron distribution function.

For a plasma with an electron population characterized by a Maxwellian distribution of temperature T_M, and a monoenergetic (primary) group of energy E_p, Eq. A-2 becomes,

$$\varepsilon_o = U_+ + \frac{\sum_j \left[\frac{n_p}{n_M} \sigma_j' v_p + \langle\sigma_j v_e\rangle_M\right] U_j}{\frac{n_p}{n_M} \sigma_+' v_p + \langle\sigma_+ v_e\rangle_M} , \tag{A-4}$$

where $< \quad >_M$ represents the enclosed product averaged over the Maxwellian speed distribution function.

The term under the summation sign in Eq. A-4 may be approximated by considering only a single equivalent lumped excited state characterized by a total excitation collision cross section σ_{ex} and a lumped excitation energy U_{ex}. For rare gases, U_{ex} may be approximated by [38],

$$U_{ex} = \frac{1}{2} (U_\ell + U_+) , \tag{A-5}$$

where U_ℓ is the lowest excitation energy level. Using this lumped excitation approximation Eq. A-4 becomes,

$$\varepsilon_o = U_+ + \frac{\left[\frac{n_p}{n_M} \sigma_{ex}' v_p + \langle\sigma_{ex} v_e\rangle_M\right] U_{ex}}{\frac{n_p}{n_M} \sigma_+' v_p + \langle\sigma_+ v_e\rangle_M} . \tag{A-6}$$

Substituting Eq. A-6 into A-1 yields the following expression for ε_p^*,

$$\varepsilon_p^* = \frac{U_+ + \varepsilon_M + \dfrac{\left[\frac{n_p}{n_M} \sigma_{ex}' v_p + \langle\sigma_{ex} v_e\rangle_M\right] U_{ex}}{\frac{n_p}{n_M} \sigma_+' v_p + \langle\sigma_+ v_e\rangle_M}}{1 - (V_c + \varepsilon_M) / V_D} , \tag{A-7}$$

The value of ε_p^* may be easily calculated using Eq. A-7 for a given

Maxwellian electron temperature, primary-to-Maxwellian electron density ratio, discharge voltage and value of V_c. In addition, the average energy of a Maxwellian electron lost to the anode (ε_M) must be known. Reference 19 gives this energy as,

$$\varepsilon_M = 2T_A + V_A \quad . \tag{A-8}$$

where T_A is the electron temperature at the anode and V_A is the difference between plasma potential and anode potential. Experiments presented earlier indicated the electron temperature at the anode was approximately 2/3 of the centerline temperature. Therefore, ε_M will be taken as,

$$\varepsilon_M = 2(\frac{2}{3} T_M) + V_A \quad . \tag{A-9}$$

Langmuir probe measurements also indicate that for the thruster configurations tested in this investigation V_A was always approximately 2v, thus, this value of V_A will be used in these calculations together with Eq. A-9.

For xenon, the values of the total excitation collision cross section required by Eq. A-7 were taken from Reference 49. Ionization cross section data were obtained from Reference 50. These data, along with polynomial curve fits used to facilitate interpolation between data points are given in Figs. A-1a and A-1b.

With these data, Eq. A-7 was used to calculate the values of ε_p^* as a function of electron temperature with the primary-to-Maxwellian electron density ratio as a parameter. The results of these calculations are given in Fig. A-2 where the values V_D=40v, V_c=0v and V_A=2v were used. From this figure, it is seen that the baseline plasma ion energy cost can vary over a wide range of values, and it is not clear

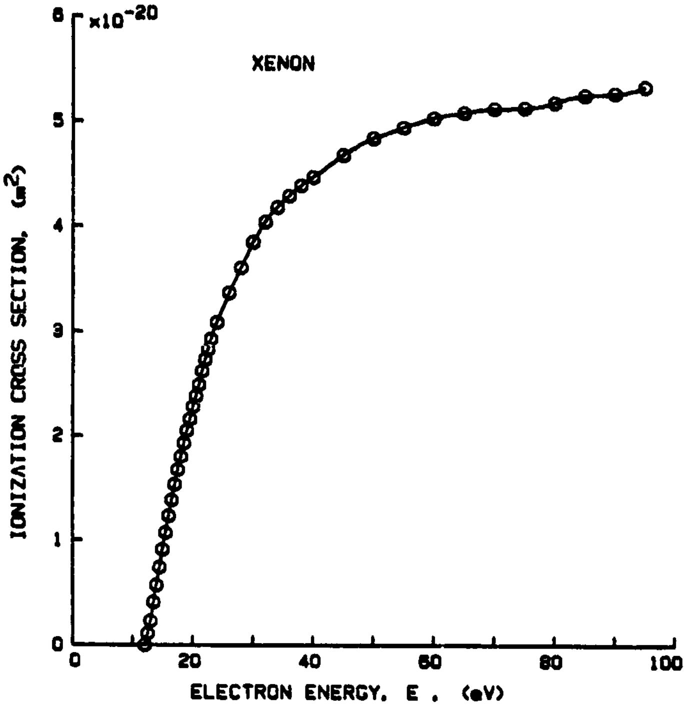

Figure A-1a. Ionization Collision Cross Section for Xenon (Ref.50)

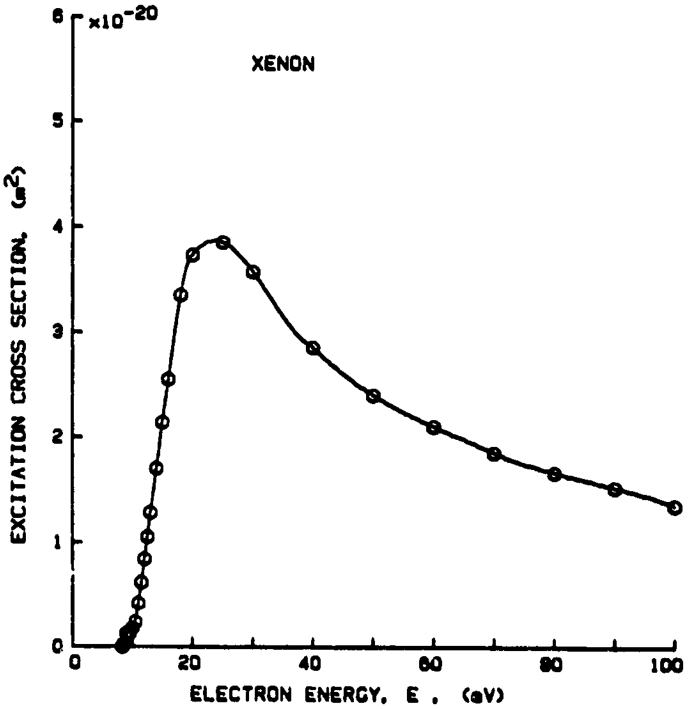

Figure A-1b. Total Excitation Collision Cross Section for Xenon (Ref. 49)

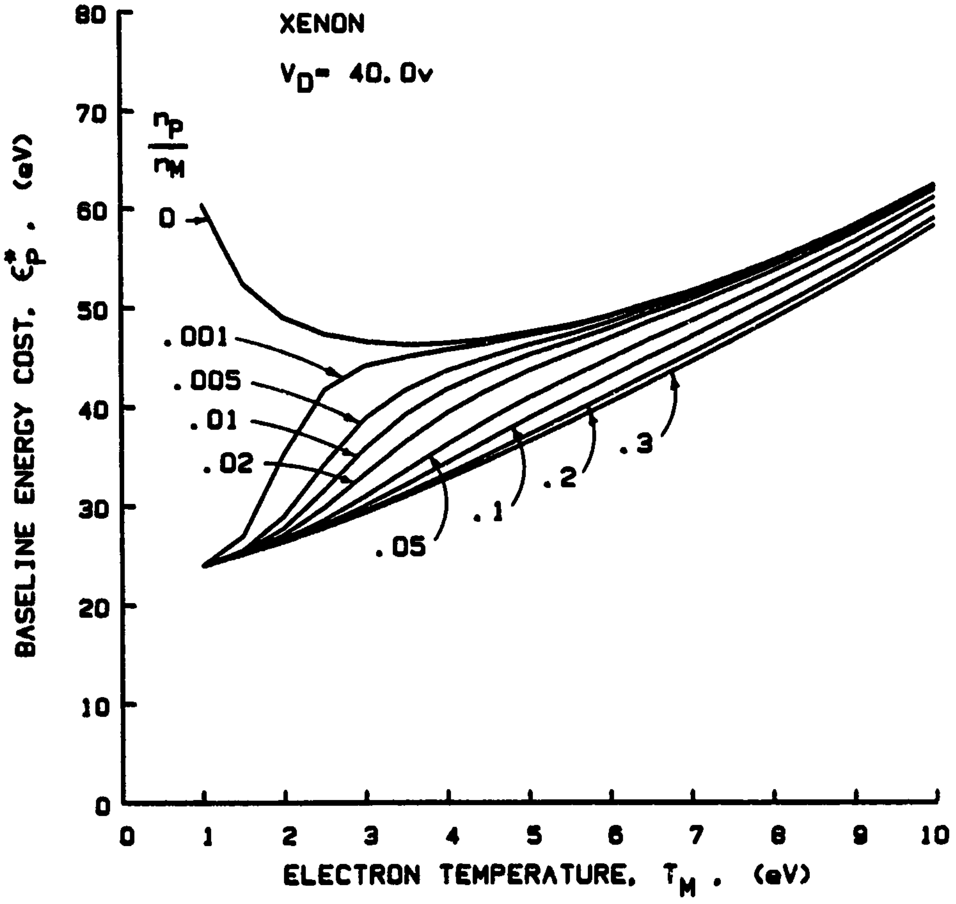

Figure A-2. Baseline Plasma Ion Energy Cost Variation Calculated from Eo.A-7 for Xenon at this point which value or values of ε_p^* are appropriate. This difficulty arises because the Maxwellian electron temperature and primary-to-Maxwellian electron density ratio may not be selected independently as was done for the calculations in Fig. A-2.

To resolve this difficulty a second equation for ε_p^* is required. This second equation for ε_p^* may be derived in the following manner. Equation 40 provides an expression for the ratio of ion current produced by primary electrons to the total ion current produced, i.e.,

$$\frac{J_p'}{J_p} = \frac{\varepsilon_p^* \sigma_+'}{V_D \sigma_o'} \quad . \qquad \text{(A-10)}$$

The total ion current produced, however, is given by Eq. 52 as,

$$J_p = n_o n_p e v_p \sigma_+' \mathcal{V} + n_o n_M e \langle \sigma_+ v_e \rangle_M \mathcal{V} \quad , \qquad \text{(A-11)}$$

and the ion current produced by primary electrons is given by Eq. 30 as,

$$J_p' = n_o n_p e v_p \sigma_+' \mathcal{V} \qquad \text{(A-12)}$$

dividing Eq. A-12 by A-11 yields,

$$\frac{J_p'}{J_p} = \frac{1}{1 + \dfrac{n_M \langle \sigma_+ v_e \rangle_M}{n_p \sigma_+' v_p}} \qquad \text{(A-13)}$$

Equating Eq. A-13 to A-10 and solving for ε_p^* yields the desired second equation for the baseline plasma ion energy cost.

$$\varepsilon_p^* = \frac{V_D \sigma_o' / \sigma_+'}{1 + \dfrac{n_M \langle \sigma_+ v_e \rangle_M}{n_p \sigma_+' v_p}} \quad . \qquad \text{(A-14)}$$

The appropriate values of ε_p^*, determined from the correct corresponding electron temperatures and density ratios, may be found by solving Eqs. A-7 and A-14 simultaneously for ε_p^* and the electron temperature for specified values of the primary-to-Maxwellian electron density ratio. This procedure is most easily accomplished graphically, as shown in Fig. A-3, where the intersection of the curves corresponding to the same values of n_p/n_M gives both ε_p^* and the electron temperature. The locus of these intersection points indicates the variation of the baseline plasma ion energy cost with the electron temperature and primary-to-Maxwellian electron density ratio. Figure A-3 indicates that, under the assumptions used for these calculations, ε_p^* does not vary substantially over wide variations in electron temperature and n_p/n_M. This agrees with the experimental observation that ε_p^* is a constant for operation with xenon propellant at a discharge voltage of 40 v.

The measured value of ε_p^* is shown along with the calculated values in Fig. A-3. The experimental value, at low electron temperatures, is seen to be generally slightly higher than the calculated values. The most likely explanation for this is a systematic measurement error of the total ion current produced as discussed in Appendix B. Also indicated in Fig. A-3 is the theoretical maximum value of ε_p^* for this case (as calculated from Eq. 41). Finally, it should be noted that the above results are somewhat sensitive to the choice of ε_M which is assumed here to be given by Eq. A-9.

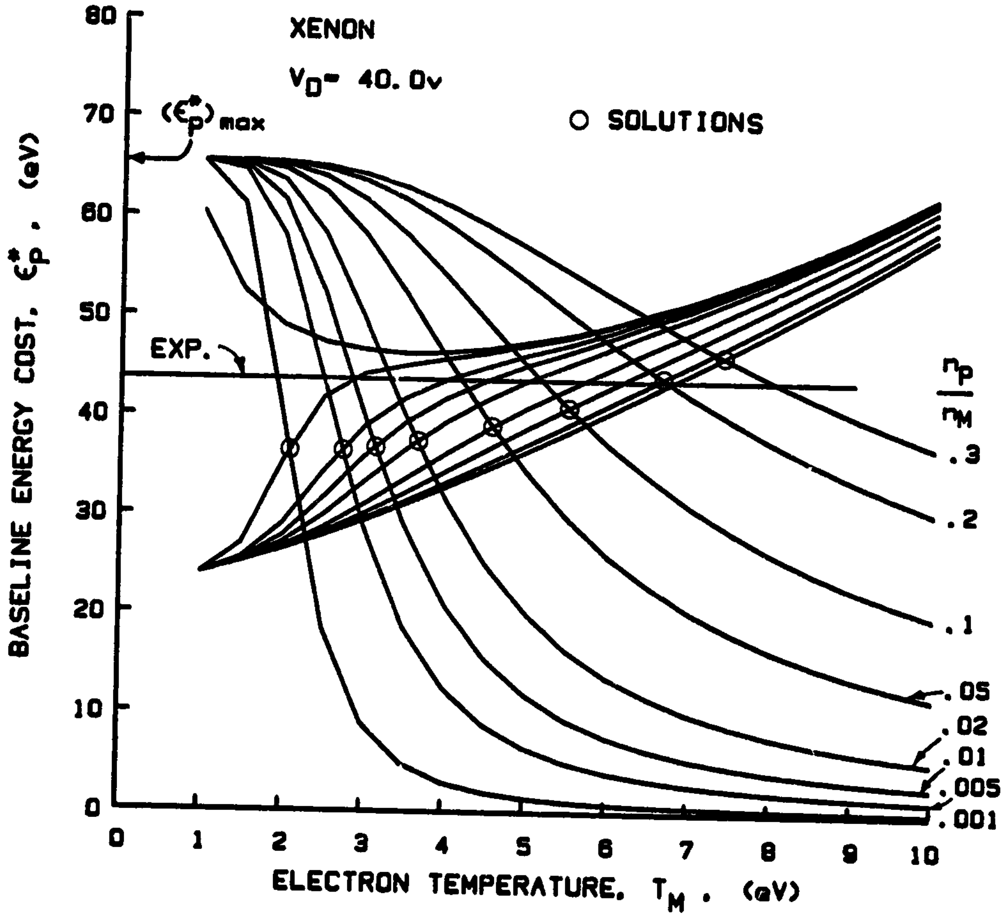

Figure A-3. Solutions for the Baseline Plasma Ion Enegry Cost for Xenon

APPENDIX B

ERROR ANALYSIS

The experiments described in this investigation require the measurement of several quantities. These quantities may be separated into four groups according to the technique required to make the measurement. These four groups are:

1. Measurement of ε_p, ε_p^* and f_B.
2. Measurement of the neutral density parameter, $\dot{m}(1-\eta_u)$
3. Measurement of the plasma properties: n_M , n_p , and T_M .
4. Measurement of doubly charged ions.

The errors associated with the measurements of the quantities in each of these groups will be discussed separately. In each case, both systematic and random errors will be discussed.

Measurement of ε_p, ε_p^* and f_B

Determination of the quantities in this group requires the measurement of the thruster electrical operating parameters including: the discharge voltage, discharge current and beam current. In addition, the total ion current produced (J_p) must be measured. The total ion current produced is given as the sum of the ion currents leaving the plasma. i.e.,

$$J_p = J_B + J_C + J_A + J_{imp} \quad .$$

The accelerator grid impingement current (J_{imp}) is generally less than one percent of the beam current, and can probably be neglected. In this investigation, however, the impingement current was always included in the total ion production current for completeness.

Measurements of the thruster electrical operating parameters were made using the ion source instrumentation shown schematically in Fig. B-1. The measurement of the ion current to cathode potential surfaces (J_C) was accomplished by biasing these surfaces 30v negative of cathode potential. With this bias, electron collection at these surfaces was eliminated allowing the incoming ion current to be measured. The ion current to anode potential surfaces (J_A) and to the cathode support posts could not be measured with this technique. The measured ion production current, consequently, does not include these currents.

Three potentially significant systematic errors associated with the measurements of J_p (and thus ε_p and f_B) have been identified. These are:

1. Neglecting the ion current to anode potential surfaces and the cathode support posts.
2. Secondary electrons emitted by ions striking the negatively biased surfaces.
3. The presence of doubly charged ions.

The most serious of these is the neglect of the ions reaching the anode surfaces and the cathode support posts. The error in J_p and ε_p resulting from this omission is difficult to assess accurately. However, the physical area of these surfaces was 5% and 2%, respectively, of the total interior surface area of the discharge chamber. Thus, one might take 7% to be the maximum systematic error in J_p resulting from the neglected ion currents. Because of these neglected currents, the

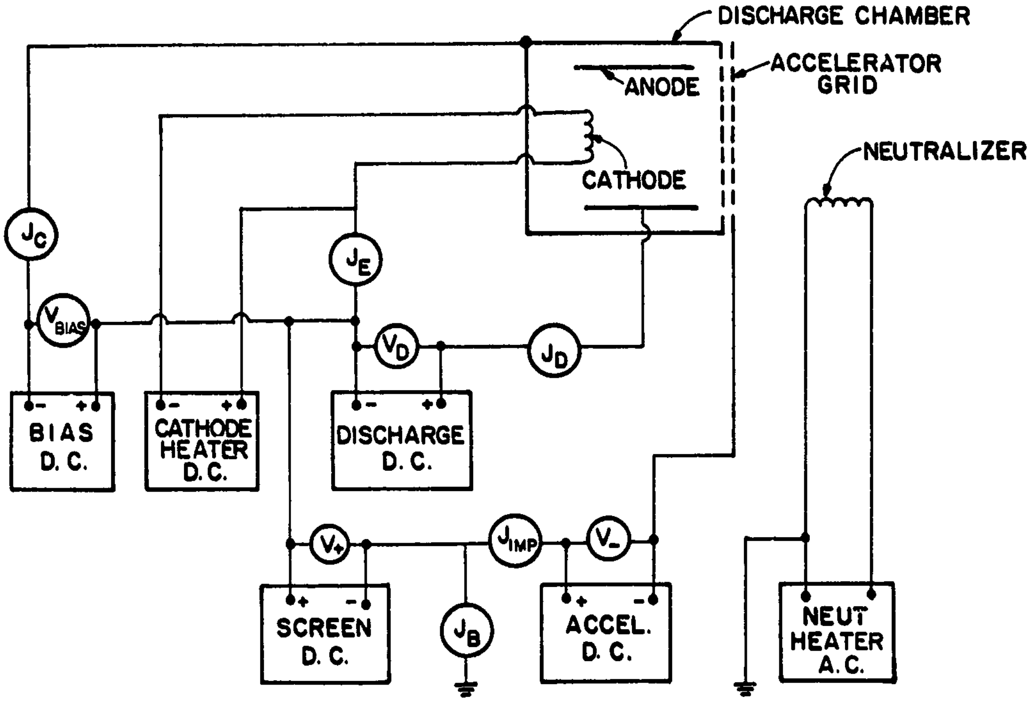

Figure B-1. Ion Source Instrumentation Schematic true value of J_p should be larger than the measured value. This implies that the true values of ε_p and ε_p^* should be smaller than the measured values according to Eq. 2. A 7% error in J_p can result in approximately a 13% error in ε_p^*. It should be noted, however, that Reference 43 through 46 indicate that the effective anode area for ion collection at a magnetic field cusp should be less than the physical area. Consequently, it is believed that the measured values of ε_p and ε_p^* are no more than 10% greater than the true values. In addition, the true value of f_B would be expected to be slightly smaller than the measured value as a result of the neglected ion currents.

Secondary electrons, emitted as a result of ions striking the negatively biased surfaces, produce an error in the measurement of the ion current to those surfaces resulting in measured values of J_c that are larger than the actual values. The largest secondary electron yields at low energies, for the ions and metal surfaces of concern in this study, appear to be for argon ions incident on a clean molybdenum surface [41]. The secondary electron yield for low energy (< 100 eV) argon ions striking molybdenum is approximately 12% [41]. If half of the ions produced strike clean molybdenum surfaces then the measured value of J_p would be approximately 6% greater than the true value as a result of secondary electron emission.

It has been observed, however, that the secondary electron yield of a clean surface decreases after exposure to air [59,60]. Reference 60 concludes that secondary electron yields are less than 1% for low intensity and low energy ion incident on a metal electrode which has been exposed to air and the ambient gas pressure is in the mtorr range during operation. In the course of the experiments in this investigation the discharge chamber surfaces were frequently exposed to air between tests. It is believed that the error in the measurement of J_p resulting from secondary electron emission is less than 1%.

In the calculations of ε_p, ε_p^* and f_B it is assumed that only singly charged ions exist. On the basis of this assumption, a doubly charged ion leaving the plasma is interpreted as two singly charged ions. The effect, however, of these doubly charged ions on ε_p, ε_p^* and f_B should not be substantial for two reasons. First, the fraction of doubly-to-singly charged ions is generally small. Second, the energy required to produce one doubly charged ion should not be vastly different than the energy required to produce two singly charged ions. The presence of doubly charged ions does have a significant effect on the value of the neutral density parameter, however, and this problem is addressed later in this appendix.

Of the three systematic errors mentioned above only the neglect of the ion currents to anode surfaces and to the cathode support posts appears to be significant. The measured values of ε_p and ε_p^* are, therefore, believed to be no more than 10% greater than the true values as a result of systematic measurement errors.

The following analysis was performed to estimate the uncertainty associated with the experimentally measured values of ε_p. The uncertainty in ε_p results from the uncertainty in the measurements of the independent variables which appear on the right-hand-side of Eq. 2. In general, the uncertainty of a quantity y which is a function of the measurable independent variables x_1, x_2, x_3. . . x_n is given by [61],

$$\Delta y = \left[\left(\frac{\partial y}{\partial x_1} \Delta x_1 \right)^2 + \left(\frac{\partial y}{\partial x_2} \Delta x_2 \right)^2 + \ldots + \left(\frac{\partial y}{\partial x_n} \Delta x_n \right)^2 \right]^{\frac{1}{2}} , \quad \text{(B-1)}$$

where Δx_i is the uncertainty of the i^{th} independent variable. For the plasma ion energy cost equation given by*,

$$\varepsilon_p = \frac{(J_D - J_p) V_D}{J_p} , \quad \text{(B-2)}$$

Eq. B-1 becomes,

$$\Delta \varepsilon_p = \left[\left(\frac{\partial \varepsilon_p}{\partial J_D} \Delta J_D \right)^2 + \left(\frac{\partial \varepsilon_p}{\partial J_p} \Delta J_p \right)^2 + \left(\frac{\partial \varepsilon_p}{\partial V_D} \Delta V_D \right)^2 \right]^{\frac{1}{2}} . \quad \text{(B-3)}$$

Carrying out the partial differentiations, Eq. B-3 becomes,

$$\Delta \varepsilon_p = \left\{ \left(\frac{V_D}{J_p} \Delta J_p \right)^2 + \left(\frac{J_D V_D}{J_p^{\,2}} \Delta J_p \right)^2 + \left[\left(\frac{J_D}{J_p} - 1 \right) \Delta V_D \right]^2 \right\}^{\frac{1}{2}} . \quad \text{(B-4)}$$

To use Eq. B-4 the uncertainties in the measurements of the discharge current (ΔJ_D), the discharge voltage (ΔV_D) and the total ion current produced (ΔJ_p) must be determined. These uncertainties result from the uncertainties of the digital meters used to make the measurements and any variation in the thruster operating set point which may occur while the data is being recorded.

Simpson digital panel meters were used to measure the discharge current, discharge voltage and beam current. These meters have an uncertainty of 0.1% plus 1 digit. The ion current to the negatively biased surfaces was measured using a Kiethly digital multimeter. This meter has an uncertainty of 0.5% plus 1 digit. The variation in the thruster operating set point was taken to be 1 digit on each of the

---

* This form of Eq. 2 is appropriate for the case where J_A may be neglected and the impingement current is included in J_B.

digital meters. In addition, 3v was added to the uncertainty in the discharge voltage because of the voltage drop across the thermonic cathode wires. With these uncertainties, the uncertainty in ε_p was calculated using Eq. B-4. The results of these calculations are shown in Fig. B-2 where the vertical error bars represent the measurement uncertainty. The horizontal error bars represent the uncertainty in the neutral density parameter and is discussed in the next section. The data in Fig. B-2 is the same as that in Fig. 6a. The uncertainty in the measured values of ε_p range from approximately 7 to 11%.

Measurement of $\dot{m}(1-\eta_u)$

Three systematic errors exist in the measurement of the neutral density parameter, $\dot{m}(1-\eta_u)$. The first is the effect of doubly charged ions on the propellant utilization efficiency. The second is the use of a gas flow meter with argon, krypton and xenon gases that has only been calibrated for air. The third is the backflow of neutral atoms from the vacuum chamber into the discharge chamber through the grids.

The presence of doubly charged ions in the beam leads to artifically high measurements of the propellant utilization and, consequently, low values of the neutral density parameter. Measurements of the doubly-to-singly charged ion beam current J_B^{++}/J_B^{+} were made along the thruster centerline. This information can be used to correct the propellant utilization according to the equation.

$$(\eta_u)_{corrected} = (\eta_u)_{measured} \; \frac{1+ \frac{1}{2} J_B^{++}/J_B^{+}}{1+ J_B^{++}/J_B^{+}} \quad , \qquad \text{(B-5)}$$

Since the value of J_B^{++}/J_B^{+} at the centerline is generally higher than

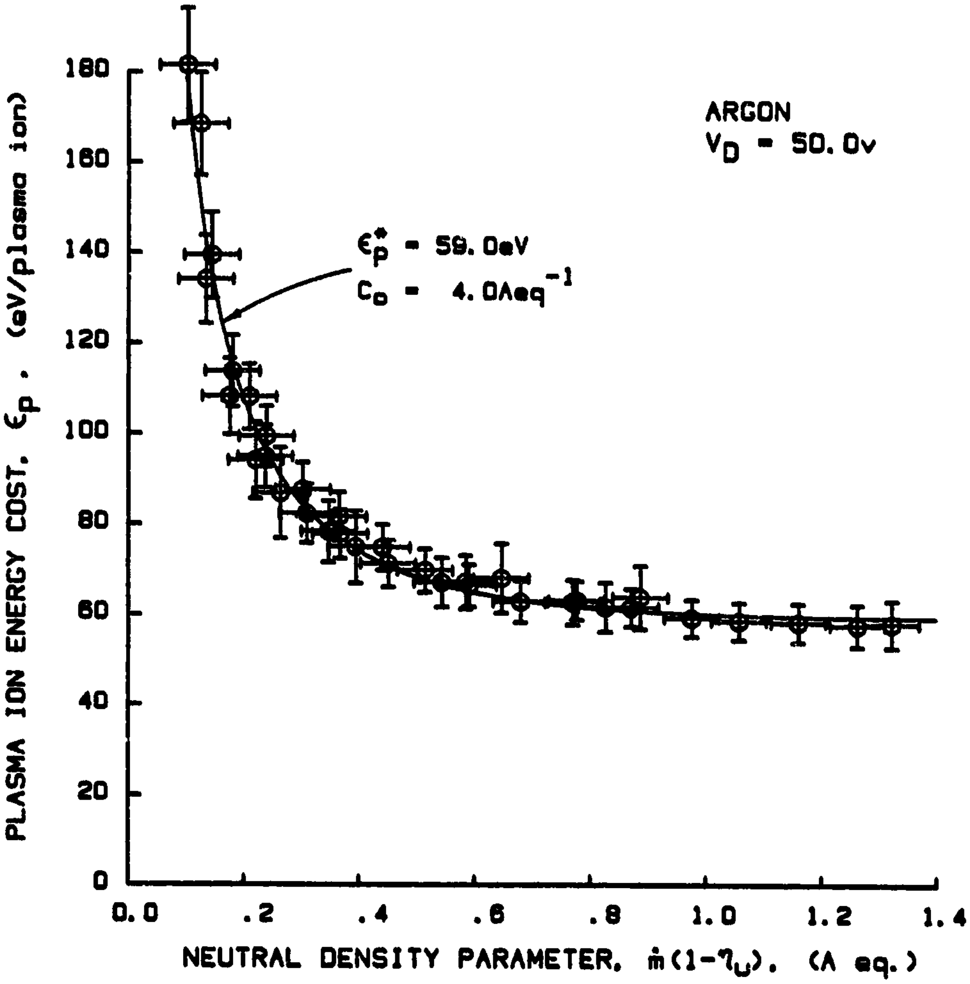

Figure B-2. Uncertainty in the Plasma Ion Energy Cost Measurements the average value its use in Eq. B-5 should tend to over correct the propellant utilization slightly. The resulting error in the neutral density parameter is believed to be small, however.

A Teledyne Hastings-Raydst flow meter with a range of 0 to 50 sccm was used to measure the propellant flow rate into the thruster. The flow meter was calibrated for air, requiring the output readings to be analytically corrected for operation with the gases argon, krypton and xenon. The use of the analytical corrections rather than recalibrating the flow meter for the different gases is expected to introduce only a very slight error in the flow rate measurement. Thus, the systematic errors in the measurement of the neutral density parameter are believed to be negligible.

The backflow of neutral atoms from the vacuum facility into the discharge chamber was calculated based on measurements of the facility pressure made ~1m downstream of the thruster. These calculations were used to correct the total propellant flow rate into the discharge chamber.

The accuracy of the flow meter is 1% of full scale. This turns out to be the major uncertainty in the determination of the neutral density parameter. The uncertainty in the neutral density parameter is indicated by the horizontal error bars in Fig. B-2.

Plasma Property Measurement

Plasma property measurements were made using one Langmuir probe positioned along the discharge chamber centerline and a second probe positioned on a magnetic field cusp. Details of the Langmuir probe circuitry used are given in Reference 62. There are two major sources of error in using Langmuir probes to obtain plasma property data. The first of these deals with obtaining the probe trace itself (i.e., measurement of collected current versus probe voltage). The second source of error arises from the analysis of the probe trace to obtain the desired plasma property information.

Errors associated with obtaining the probe trace include such things as: the variation in work function over the probe surface area, secondary electron emission from the probe, probe insulator contamination, noise in the plasma, electrical noise in the probe circuitry, plasma perturbation by the probe, and magnetic field effects. Plasma perturbation by the probe is minimized by using a probe with a small surface area. Biasing the probe negative of cathode potential when data is not being collected tends to sputter clean the surface and minimizes the variation in work function over the probe surface area. Changing the probe support insulator frequently (∿ every 6 hours) minimizes the problem of insulator contamination. Noise in the plasma was minimized by using a D.C. current heated therminoic cathode. Magnetic field effects were minimized by placing the probe on the discharge chamber centerline where the magnetic flux density was less than 0.001 tesla. For the probe positioned on the magnetic field cusp, where the magnetic flux density is approximately 0.2 tesla, the magnetic field effects are substantial. In this case, only the electron temperature and primary electron energy data obtained from these traces are believed to be meaningful.

The probe traces were analyzed using a non-linear numerical curve fitting routine similar to the one described by Beattie [6]. This routine assumes an electron population that is characterized by a Maxwellian plus mono-energetic (primary) electron energy distribution. Probe traces were digitized using an HP-7470A graphics plotter together with an HP-85 mini-computer. The plotter may be used as a digitizer when equipped with a special digitizing sight. Accurate digitizing is crucial to obtaining good primary electron information.

The errors introduced during probe trace digitizing and analysis may be determined by generating idealized probe traces with known plasma properties and then analyzing these traces in the usual manner. Eight such idealized probe traces were generated and analyzed, covering a wide range of plasma conditions. The results indicated that the data analysis can accurately distinguish primary-to-Maxwellian electron density ratios as small as 0.2% provided the Maxwellian electron temperture is low. The most difficult traces to analyze are those corresponding to low primary-to-Maxwellian electron density ratios in a plasma with a high Maxwellian electron temperature. This particular plasma condition, however, was not observed experimentally in the course of this investigation. The results in Chapters III, IV and Appendix A of this report indicate that when the primary-to-Maxwellian electron density ratio is small the Maxwellian electron temperature is low and when the electron temperature is high the primary-to-Maxwellian electron density ratio is large. These types of probe traces are accurately analyzed with the data reduction system used in this investigation. The idealized probe trace analysis indicated that under most conditions the following errors may be expected from the digitizing and curve fitting procedures:

Plasma Potentional	± 0.3 v
Maxwellian Electron Density, n_M	± 5%
Maxwellian Electron Temperature, T_M	± 3%
Primary Electron Density, n_p	± 15%
Primary Electron Energy, E_p	± 5%
n_p/n_M	± 3%

The overall uncertainty associated with the plasma property measurements are believed to be the following:

Plasma Potential	± 1.0 v
Maxwellian Electron Density, n_M	± 20T
Maxwellian Electron Temperature, T_M	± 10%
Primary Electron Density, n_p	± 30%
Primary Electron Energy, E_p	± 10%
n_p/n_M	± 30%

Measurement of Doubly Charged Ions

Measurements of doubly charged ions in the beam were made using an $\vec{E}$ x $\vec{B}$ probe similar to that described in Reference 42. Errors associated with these measurements include: the accuracy of the picoammeter used to read the probe current, selection of the proper probe deflection voltage to obtain the maximum signal corresponding to the particular charged specie of interest, and variation in the thruster operating conditions during data collection.

Probe current readings were made using a Keithly model 410A picoammeter with an accuracy of ± 4% of full scale. Selection of the proper probe deflection voltage is a fairly difficult thing to do accurately because of the slow response time of the picoammeter (between 0.4 and 12s). This is especially true for currents in the lowest ranges of the ammeter. Errors resulting from the uncertainty in probe deflection voltage and variation in thruster operating conditions are believed to introduce a maximum error of 10% in the measured values of the single and double ion currents. The total uncertanties in the measured values of the doubly-to-singly charged ion current ratio, resulting from the sources of error mentioned above, are indicated in Fig. B-3 by the vertical error bars. The horizontal error bars indicate the uncertainty in the corrected propellant utilization efficiency as mentioned earlier.

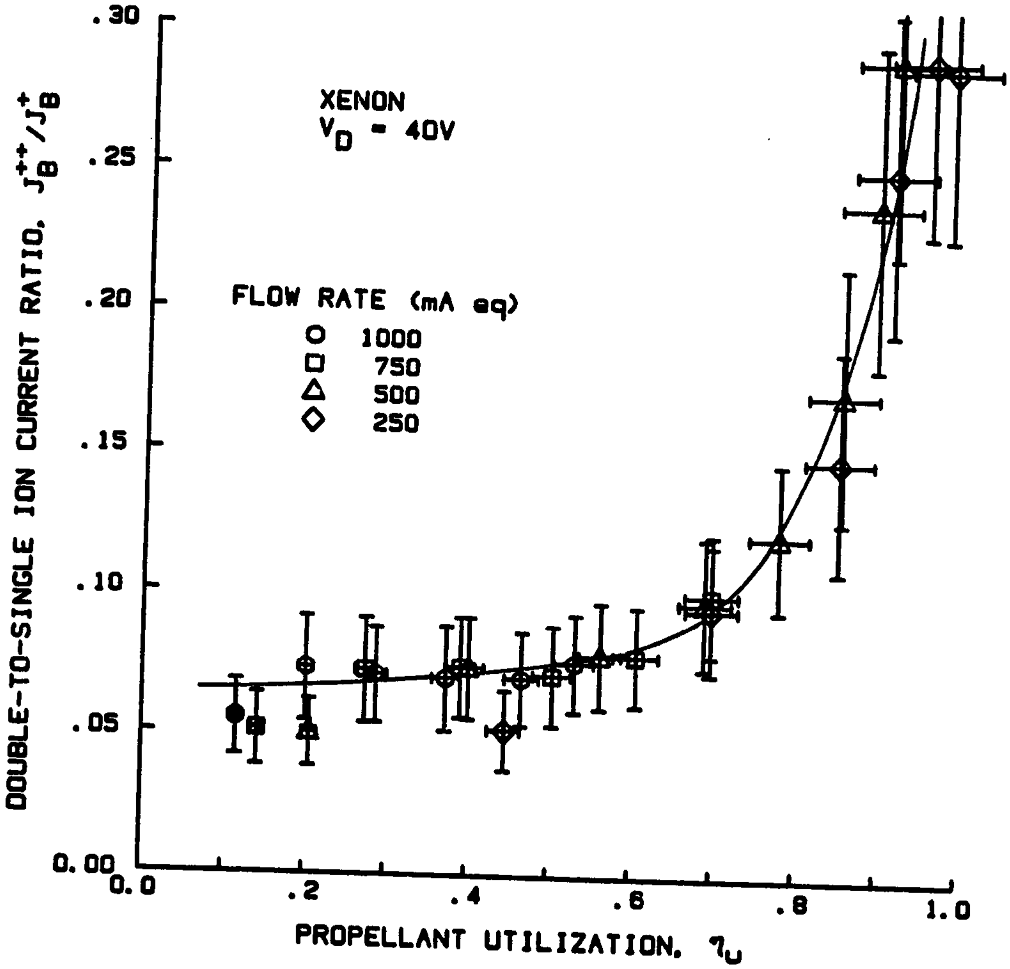

Figure B-3. Uncertainty in the Doubly-to-Singly Charged Ion Beam Current Measurements

APPENDIX C

NOMENCLATURE

A_g = Area of grids through which the ion beam is extracted (m^2)

B_o = $\dot{m}C_o$

C_o = Primary electron utilization factor defined by Eq. 26 $(A\ eq.)^{-1}$

E_p = Primary Electron Energy (eV)

e = Electronic Charge (1.6×10^{-19} coul.)

f_A = Fraction of ion current to anode surfaces

f_B = Extracted ion fraction

f_C = Fraction of ion current to cathode surfaces

J_A = Ion current to anode potential surfaces (A)

J_B = Ion beam current (A)

J_B^+ = Singly charged ion beam current (A)

J_B^{++} = Doubly charged ion beam current (A)

J_C = Ion current to cathode potential surfaces (A)

J_D = Discharge current (A)

J_E = Cathode Emission Current (A)

J'_{ex} = Total production rate of excited neutral atoms by primary electrons - expressed as a current (A)

J_{imp} = Accelerator grid ion impingement current (A)

J_j = Production rate of jth excited state expressed as a current (A)

J_L = Primary electron current to the anode (A)

J_M = Maxwellian electron current to the anode (A)

J_p = Total ion current production rate expressed as a current (A)

J_p' = Ion production rate by primary electrons expressed as a current (A)

J_p^+ = Production rate of singly charged ions expressed as a current (A)

J_p^{++} = Production rate of doubly charged ions expressed as a current (A)

$J_{p,m}$ = Ion production rate by Maxwellian electrons expressed as a current (A)

ℓ_e = Primary electron containment length (m)

M_f = Final spacecraft mass (kg)

M_g = Generator mass (kg)

M_i = Initial spacecraft mass (kg)

M_ℓ = Payload mass (kg)

M_{p_o} = Initial propellant mass (kg)

m_e = Electron Mass (kg)

m_i = Ion mass (kg

$\dot{m}$ = Thruster propellant flow rate (A eq.)

$\dot{m}_p$ = Total spacecraft propellant flow rate (kg/s)

n_e = Total electron density (m^{-3})

n_i = Total ion density (m^{-3})

n_M = Maxwellian electron density (m^{-3})

n_p = Primary electron density (m^{-3})

n_o = Neutral atom density (m^{-3})

$\dot{n}_o$ = Neutral atom loss rate (A eq.)

P_g = Generator Power (W)

P_o^+ = Primary electron rate factor for ionization of neutral atoms (m^3/s)

P_o^{++} = Primary electron rate factor for double ionization of neutral atoms (m^3/s)

P_{+}^{++} = Primary electron rate factor for the production of double ions from single ions (m^3/s)

Q_{o}^{+} = Maxwellian electron rate factor for ionization of neutral atoms (m^3/s)

Q_{o}^{++} = Maxwellian electron rate factor for double ionization of neutral atoms (m^3/s)

Q_{+}^{++} = Maxwellian electron rate factor for the production of double ions from single ions (m^3/s)

T_A = Maxwellian electron temperature at anode surface (eV)

T_M = Maxwellian electron temperature in bulk plasma (eV)

t = Mission duration (s)

u = Ion exhaust velocity (m/s)

U_{ex} = Lumped excitation energy (eV)

U_+ = Ionization energy (eV)

U_j = Excitation energy of jth excited state (eV)

U_ℓ = Lowest excitation energy (eV)

V_A = Anode sheath voltage (v)

V_C = Plasma potential from which electrons emitted by the cathode are accelerated to become primary electrons

V_D = Discharge (Anode) voltage (v)

V_N = Net accelerating voltage (v)

V_+ = Screen grid supply voltage (v)

V_- = Accelerator grid supply voltage (v)

v_b = Bohm velocity (m/s)

v_e = Electron velocity (m/s)

v_p = Primary electron velocity (m/s)

v_o = Neutral atom velocity (m/s)

$\mathcal{V}$ = Volume of ion production region (m^3)

x = Independent variable

y = Dependent variable

α = Power plant specific mass (kg/w)

ΔJ_D = Discharge current uncertainty (A)

ΔJ_p = Ion production current uncertainty (A)

ΔV = Characteristic velocity (m/s)

ΔV_D = Discharge voltage uncertainty (V)

Δx = Uncertainty of independent variable

Δy = Uncertainty of dependent variable

ε_B = Average beam ion energy cost (eV/beam ion)

ε_M = Average energy of Maxwellian electrons leaving the plasma at the anode (eV)

ε_p = Average plasma ion energy cost (eV/plasma ion)

ε_p^* = Baseline plasma ion energy cost (eV/plasma ion)

ε_o = Average plasma ion energy cost considering ionization and excitation processes only (eV)

η_t = Thruster electrical efficiency

η_u = Propellant utilization efficiency

σ_{ex} = Total excitation collision cross section (m^2)

σ'_{ex} = Total excitation collision cross section at the primary electron energy (m^2)

σ_j = Excitation collision cross section of the jth state (m^2)

σ'_j = Excitation collision cross section of the jth state at the primary electron energy (m^2)

σ'_o = Total inelastic collision cross section at the primary electron energy (m^2)

σ_+ = Ionization collision cross section (m^2)

σ'_+ = Ionization collision cross section at the primary electron energy (m^2)

ϕ_a = Transparency of the accelerator grid to neutral atoms

ϕ_i = Transparency of the screen grid to ions

ϕ_s = Transparency of the screen grid to neutral atoms

ϕ_o = Effective transparency of the grid system to neutral atoms

$< >$ = Average over the entire electron energy distribution function

$< >_M$ = Average over the Maxwellian energy distribution function